The Role of van der Waals Interactions and Nuclear Quantum Effects in Soft Layered Materials

Gabriella Graziano

A dissertation submitted in partial fulfillment

of the requirements for the degree of

Doctor of Philosophy

of

University College London.

Department of Chemistry

UCL

21 October 2014

I, Gabriella Graziano, confirm that the work presented in this thesis is my own. Where information has been derived from other sources, I confirm that this has been indicated in the work.

Abstract

Recent years have seen a surge of interest in layered materials, mainly because of their numerous applications, prominently in gas sorption. These materials are highly anisotropic, because of the coexistence of covalent bonds within the individual layers and weak van der Waals (vdW) interactions between layers. Although the anisotropy makes layered materials appealing for many technological applications, it also makes their full theoretical and experimental description difficult. This study has addressed some of the major gaps in our understanding of layered materials using a combination of theoretical and experimental techniques. Computationally, newly developed functionals able to treat both short and long range interactions within density functional theory have been used to look at the structure, energetics, dynamics and adsorption properties of layered materials. Neutron scattering experiments have been used to further our understanding of the atomic dynamics in graphite and to set up a preliminary study of the hydrogen adsorption in doped graphite.

The present results underline strong similarities of the vdW-dominated properties of the systems examined. The interlayer binding energies and the hydrogen adsorption capabilities have been found to be surprisingly similar. Analysis shows that this is due to a fine balance between attractive and repulsive forces and, more specifically between atomic polarizabilities and volumes of the material components.

The comparison between experimental and predicted atomic displacements in graphite highlights that the carbon dynamics is affected by nuclear quantum effects at temperatures lower than 300 K. These temperatures are common for many technological applications, especially those related to gas adsorption. Thus, the presented results pose some questions on what could be the correct model and computational technique to use in order to gain a better understanding of the sorptive properties of layered materials, especially carbon based, and move forward in the design of new gas storage materials.

Publication

The work presented in this thesis has led to the following publications:

- *"Improved description of soft layered materials with van der Waals density functional theory"* G. Graziano, J. Klimeš, F. Fernandez-Alonso and A. Michaelides, J. Phys.: Condensed Matter **24**, 424216 (2012).
- *"Theoretical and experimental assessment of carbon dynamics in graphite"* G. Graziano, M. J. Guttmann, A. Michaelides, F. Fernandez-Alonso, *in preparation.*

Acknowledgements

I would like to express my gratitude to all the amazing people I have met over these four years who, consciously or not, have helped, supported and always taught me something. First of all I would like to massively thank my supervisors Angelos Michaelides and Felix Fernandez-Alonso for their constant guidance, for all the precious discussions and insights and, most of all, for believing in me and encouraging me throughout my PhD.

I wish to thank Jiří Klimeš and Matthias Gutmann for their input into this project, specifically for their contribution to Chapter 3 and Chapter 4, for their valuable explanations of many aspects of this scientific field and for their patience in answering to all of my (mostly silly) questions. A special thank goes also to Andrew Seel and Svemir Rudic for their big help before, during and after the experiments at ISIS. I also would like to thank Chis Howard and Felicty Dear for the preparation of the samples and the precious help during my very last experiment.

I also feel so lucky to have spent these four years being part of the ICE group. Xinzheng, Thor, Ming, Jiri, Brent, Erlend, Nanaxhi, Wei, Philipp, Chiara, Yasmine, Steve and Gabriele: it has been a privilege for me working with you. Questioning our work together, helping and supporting each other, not to mention, having great fun together showed me the beauty of working in a solid team and I can say with confidence that you have not been just my colleagues, but my family during this time. I will always be grateful to you all for being there for me.

I would like also to thank my friends, Antonella, Teresa, Cecilia and Ivan for always being present and always being able to relieve me from tough times.

A special thank goes to my parents for encouraging and believing in me no matter what, and to my brother Gianluca, who "ordered" me to buy the one way flight ticket to London four and half years ago without which I would never have had the most amazing years of my life. Finally a huge thank goes to my husband Marco who has embraced with the same passion this adventure with me, for being always supportive and very (very!) patient, and simply for being part of these amazing four years.

Contents

List of Figures

List of Tables

Nomenclature

AIMD	Ab initio molecular dynamics
DFPT	Density functional perturbation theory
DFT	Density functional theory
DOE	Department of Energy
h-BN	hexagonal-boron nitride
INS	Inelastic neutron scattering
optB88-vdW	optimized Becke88 van der Waals
PIMD	Path integral molecular dynamics
QNE	Quantum nuclear effect
TOF	Time–of–flight
v–DOS	Vibrational density of states
vdW	van der Waals
vdW-DFs	van der Waals density functionals
ZPE	Zero point energy

Chapter 1

Introduction

Since the discovery of graphene [1], material science has seen a surge of interest in layered materials and the possibility of generating new 2D materials with unexplored and exciting properties. Besides graphene and graphite, the list of layered materials is quite remarkable and it includes: *hexagonal*-boron nitride (*h*-BN), also known as inorganic or "*white*" graphite, the class of the transition metal dichalcogenides with formula MX_2 (with M=Mo,W, Ti and X=S, Se, Te), layered oxides and more. The popularity of this class of materials mainly arises from their strong anisotropy which results from the covalent bond of the atoms within a layer, and the weak interactions, mainly due to van der Waals (vdW) forces between the layers.

It is exactly the coexistence of strong and weak bonds affecting not only the mechanical properties but also the chemistry and physics of these materials, which makes them appealing for many technological applications. Because of the weak interactions between the layers they are easy to exfoliate: for example the common every day process of writing with a pencil is nothing but an exfoliation of graphite, where the layers are left as a mark on the paper. More sophisticated uses of graphite and other layered materials have been explored over the years. They have been extensively used as lubricants, especially at high temperature [2, 3, 4, 5]. Because of their ability to expand their interlayer distance, it is possible to intercalate atoms or small molecules within the layers. In fact outstanding and highly studied application comes from the intercalation of single atoms, like lithium, in graphite and some transition metal dichalcogenides which has made these materials very promising as anodes for lithium-ion based batteries [6, 7], now widely used in most electronic devices.

In addition the ability of layered materials to intercalate small molecules has also

been exploited to develop small transistors used as gas sensors. As an example, it has been found that transistors based on different numbers of layers of MoS_2 are able to sense NO, NO_2, NH_3, H_2S and more complex molecules like dopamine and glucose [8, 9, 6, 10]. It is then natural to think of these materials not only as gas sensors, but also as gas storage devices. In fact the last couple of decades especially the porous carbon based materials (layered, and metal-organic frameworks) have been addressed as promising solution for the hydrogen storage problem. Despite the prolific work in this field, from both theoretical and experimental perspectives, still major gaps remain in the full understanding of the fundamental chemistry and physics of the interaction between the hydrogen and the substrates. In this work the interaction between hydrogen and layered materials has been studied in detail. In particular, attempts to tackle the role of weak forces, like vdW, in the physical adsorption (physisorption) of the hydrogen in and on different layered substrates have been made.

In order to understand the motivations behind this work, a short review of the state of the art in the hydrogen storage field needs to be presented.

Hydrogen is the most abundant element in nature and exists as a stable homonuclear molecule H_2. Recent studies show how hydrogen could be one of the most promising clean energy carriers, able to replace fossil fuels [11, 12]. Indeed, hydrogen has been recognized as an ideal and green energy vector, since its combustion releases just heat and water which represents an important prerequisite for a sustainable low-CO_2 economy. However, due to its unfavorably low volumetric energy density, it is extremely difficult to store hydrogen unless cryogenic temperatures and very high pressures are used [13, 14]. The transport industry is the main sector involved in the replacement of fossil fuels with cleaner and more sustainable resources like hydrogen. By 2015 it is expected that hydrogen powered vehicles will be available on the market and they will be based on a high pressure (70 MPa) carbon composite tank system [15]. Of course this is just the beginning and still a lot of research is needed to improve the safety and the efficiency of the refueling system, to improve the consumption and to reduce the costs for the commercialization of these vehicles [15, 16]. Because of this, many studies over the last twenty years in this area have focused on new materials that can store hydrogen, trying to match all the safety and technological requirements stated by the United States (DOE). According to one of the more recent reviews in the field [16], it is possible to group materials for hydrogen storage in three classes, namely reversible metal hydrides, chemical hydrogen stores and hydrogen sorbents or porous materials.

- *Reversible metal hydrides:* Metal alloys, such as $LaNi_5$, TiFe, and MgNi, were the first materials proposed for H_2 storage since they easily form metal hydrides. Hydrogen can then be released by dehydrogenation of the hydrides [17]. The hydrogenation process is direct, with no intermediate steps and is also spontaneous with a very high enthalpy. The high enthalpy is translated into a great heat released by the hydrogenation process which makes the on-board refueling dangerous and difficult [15]. In addition, metal hydrides are very stable products, thus a great amount of energy is necessary to dehydrogenate them. Transition metal hydrides can improve the thermodynamics of the hydrogenation–dehydrogenation process, making it more reversible. However they require the inclusion of other elements, such as rare-earth metals, that make these materials heavy and expensive and not so promising for commercial production [18, 15].

- *Chemical hydrogen stores:* Compounds like ammonia borane and its derivatives belong to this class and they have a high volumetric and gravimetric density. Their dehydrogenation is a multiple–step process and it is favoured by the presence of the protic (partially positive and bound to nitrogen) and hydric (partially negative and bound to boron) hydrogens. Nevertheless the dehydrogenated nitrogen and boron polymerise, hindering the rehydrogenation step [15].

- *Porous materials:* Graphitic materials, zeolites and metal-organic frameworks (MOFs) belong to this class and they match with the highest number of prerequisites defined by the DOE [15]. It has been found that low density nanoporous materials can store hydrogen by physisorption, which does not involve any chemical changes to the material (substrate) or to hydrogen (adsorbate), and allows faster loading and unloading dynamics. Nanoporous carbon materials seem to be promising candidates for this purpose because they can combine low-weight with fast kinetics for gas charging and discharging [13, 19, 20]. However, since the physisorption of H_2 on a substrate is dominated by weak vdW forces, only a small amount of gas can be stored at room temperature. Thus cryogenic temperatures (77 K) are required to increase the quantity of hydrogen stored in carbon based materials. Nevertheless, even the use of such a low temperature only brings the capacity of these materials to 1% per weight which is still too low if compared to the requirement of 6.5%, as defined by DOE [21, 13, 17]. Many approaches have been suggested in order to increase

the strength of the substrate–adsorbate interaction within the physisorption regime [22, 23]. In fact the stronger the adsorbate interaction, the higher the ability of the substrate to hold hydrogen and increase the quantity of gas stored. Most work to date shows how the dimensional scale (nanometric regime [13]) and surface area [19, 24, 20], the shape (nanotubes [22, 25], nanohorns [13, 26], nanoscrolls [27], pillared structures [18]) and metal intercalation (alkali metal intercalation [21, 28, 29, 30]) play very important roles in the interaction between H_2 and porous materials. Other kinds of interactions between physisorption and chemisorption, like those investigated by Kubas [31, 32], seem to be also encouraging solutions for the hydrogen storage problem. Kubas interactions are in fact stronger than pure vdWs but still weaker then the chemical bonds in the hydrates. They are based on the formation of a σ–π complex between the hydrogen molecule and a metal active site on the surface of the porous material. In this way the hydrogen bond is elongated but still no new chemical bonds are formed and in principle this can guarantee good performances in the hydrogen adsorption also at room temperature [24].

In this work we focused particularly on the class of porous materials, because although these are good candidates as hydrogen sorbents, the physisorption process still need to be optimised. In order to do so a fundamental understanding of general adsorption is needed. As mentioned earlier the physisorption process is due to weak interactions, mainly vdW forces, between the adsorbate and the substrate. In addition, vdW forces are also fundamental for the structure of the substrate itself in this case. Nevertheless a theoretical description of these forces was not achievable until the last decade, unless very computationally expensive methods were used. In recent years, much effort has been made in order to develop theoretical tools able to treat properly long–range interactions, such as vdWs, at reasonable computational cost. The accurate description of vdW forces is an exceptionally active area of research within the framework of density functional theory (DFT) [33, 34, 35]. Indeed, DFT is the most popular method for electronic structure predictions in the condensed phase and although it is in principle exact, relies upon approximations made in the exchange–correlation functionals, that in most cases neglect long–range interactions. However, a large number of new functionals have recently been proposed to include the long–range interactions [35]. Thus this work has made extensive use of DFT, especially of vdW–inclusive functionals, to gain a deeper understanding not only of the physisorption of hydrogen on layered materials, but also of the structure,

energetic and dynamical properties of layered materials in general.

In the next chapter a detailed explanation of DFT and the main exchange–correlation functionals used in this study will be reported, in addition to discussion of neutron scattering experimental techniques that have also been used throughout this project to benchmark and design the theoretical prediction. This will be followed by Chapter 3, where results of the structural and energetic properties of graphite and h-BN studied by using several density functionals are reported. Here the performances of different functionals has been compared to experiment and high–accuracy theoretical predictions, where values were available. These results assess that especially one of the new vdW-DFs, namely the (optB88-vdW) [36, 37] predicts values in good agreement with experiment and higher–accuracy theory. For this reason optB88-vdW has been the main functional to further study layered materials and their interaction with hydrogen.

Before looking at the interaction between different layered materials and hydrogen, particularly the graphite substrate has been further investigated. Chapter 4 focuses on the study of the carbon dynamics in graphite as a function of temperature. Although graphite is ubiquitous and has been the subject of a large body of experimental and theoretical studies, a consistent physical picture describing carbon motion does not exist. Here we try to understand the nature of this dynamics by looking at the contribution of the harmonic, anharmonic and high order nuclear quantum effects to the carbon displacement in graphite. The anisotropic displacement parameters at different temperatures as obtained from a single crystal neutron scattering experiment (reported in Chapter 4) and deep inelastic neutron scattering, as well as the measured vibrational density of states (reported in the Appendices A and B) have been compared to theoretical predictions from DFT. This comparison has highlighted that above 300 K the carbon displacement shows classical, anharmonic behaviour and that below 300 K quantum nuclear effects may be not negligible.

In Chapters 5 and 6 the interaction between hydrogen and layered materials is discussed. Chapter 5 tries to fill some of the gaps in our understanding of the role of vdW in solids and adsorption on surfaces. This issue has been tackled with a systematic DFT study of hydrogen adsorption on a range of layered materials. One of the findings is that on all substrates analysed the hydrogen physisorption energies are surprisingly similar. This observation is in line with recent calculations of interlayer binding energies of these materials [38, 39, 40]. Analysis shows that this arises from a delicate interplay between the polarizability and volume of the atoms.

This balance may give some overall insight into the extent and nature of the physisorption process in general. Finally in Chapter 6 the optB88-vdW functional has been used to investigate the absorption of the hydrogen in graphite intercalated systems. As mentioned earlier the intercalation of alkali metals within graphite layers has been recognised as a promising way to increase the strength of the absorption energy between hydrogen and a substrate, whilst still being in the physisorption regime. In particular, the intercalation of potassium in graphite in a concentration of KC_{24} not only expands the graphite interlayer distance so that it can easily absorb hydrogen, but it also polarizes the hydrogen molecule leading to a stronger H_2–substrate interaction which can increase the quantity of hydrogen stored in carbon based materials [21, 29, 30, 41, 42]. The calculations reported here shed light on the structure of the pristine substrate, the concentration of the hydrogen and the optimal configurations of the molecules within the substrate.

Chapter 7 concludes this work with a summary and outlook.

Chapter 2

Methods

In this chapter the theory behind the computational and experimental techniques used in this work will be described. The greater part of the results presented and discussed in the next chapters have been achieved by performing calculations within the framework of density functional theory (DFT). DFT is quantum mechanical theory used to solve and investigate the electronic structure of materials. It makes use of the electron density as the main variable, in such a way it cuts down on the computational cost, whilst still satisfying a good level of accuracy. This is the reason why DFT became such a popular computational tool in the last decades and the scientific community is still very active in developing and increasing the accuracy versus computational cost ratio. Different properties of layered materials have been explored from an experimental perspective, by using neutron scattering techniques. One of the main advantages of using neutrons is that they interact directly with the nuclei of the atoms and therefore *"neutrons tell us where atoms are and how they move"*, just to cite Clifford G. Shull, pioneer of the neutron scattering technique with Bertam Brockhouse. The theory behind neutron scattering techniques will also be briefly discussed in the final sections of this chapter.

2.1 Quantum mechanics

2.1.1 Schrödinger equation

The complete description of a system is achieved by solving the Schrödinger equation:

$$\hat{\mathrm{H}}\psi(\mathbf{r},\mathbf{R}) = E\psi(\mathbf{r},\mathbf{R}), \tag{2.1}$$

where ψ is the many-body wavefunction expressed as a function of the electronic and nuclear coordinates, respectively $\mathbf{r}$ and $\mathbf{R}$, with energy E. $\hat{H}$ is the non-relativistic Hamiltonian which, for a system of M nuclei and N electrons, can be expressed as:

$$\begin{aligned}\hat{H} &= -\frac{1}{2}\sum_{i}^{N}\nabla_i^2 - \frac{1}{2}\sum_{A}^{M}\frac{\nabla_i^2}{M_A} + \\ &\quad -\sum_{i}^{N}\sum_{A}^{M}\frac{Z_A}{|\mathbf{r}_i - \mathbf{R}_A|} + \sum_{i}^{N}\sum_{j>i}^{N}\frac{1}{|\mathbf{r}_\mathrm{i} - \mathbf{r}_\mathrm{j}|} + \sum_{A}^{M}\sum_{B>A}^{M}\frac{Z_A - Z_B}{|\mathbf{R}_A - \mathbf{R}_B|},\end{aligned} \tag{2.2}$$

where M_A and Z_A are respectively the mass and the atomic number of the nucleus A. The first two terms refer to the kinetic energy of the electrons and nuclei, while the remaining terms refer to the Coulomb interaction between electrons and nuclei, electrons and other electrons, and nuclei and other nuclei respectively. Despite the simplicity of the Schrödinger equation, its solution is very difficult to achieve. In fact the number of variables increases exponentially with the size of the system and approximations have to be made in order to get closer to the exact solution of the Schrödinger equation.

2.1.2 Born-Oppenheimer approximation

The Born-Oppenheimer approximation is used in order to reduce the dimensionality of the Schrödinger equation by splitting it into a nuclear and electronic part [43]. This is possible because the nuclei are much heavier than the electrons and their dynamics are much slower compared to the electron dynamics, so they can be considered static with respect to the electrons motion. Thus the two parts of the Schrödinger equation can now be written as:

$$\hat{\mathrm{H}}_\mathrm{e}\psi_e(\mathbf{r},\mathbf{R}) = E_{el}\psi_e(\mathbf{r},\mathbf{R}) \tag{2.3}$$

for the electronic equation and

$$\hat{\mathrm{H}}_\mathrm{n}\psi_n(\mathbf{R}) = E_n\psi_n(\mathbf{R}) \tag{2.4}$$

for the nuclear one.

Also the electronic and nuclear Hamiltonian ($\hat{H}_e$ and $\hat{H}_n$) are now simplified compared to Eq.2.2:

$$\hat{H}_e = -\frac{1}{2}\sum_i^N \nabla_i^2 - \sum_i^N \sum_A^M \frac{Z_A}{|\mathbf{r}_i - \mathbf{R}_a|} + \sum_i^N \sum_{j>i}^N \frac{1}{|\mathbf{r}_i - \mathbf{r}_j|}, \tag{2.5}$$

$$\hat{H}_n = -\frac{1}{2}\sum_A^M \frac{\nabla_i^2}{M_A} + E_{el}(\mathbf{R}) + \sum_A^M \sum_{B>A}^M \frac{Z_A - Z_B}{|\mathbf{R}_A - \mathbf{R}_B|}. \tag{2.6}$$

In $\hat{H}_e$ the nuclear kinetic energy is neglected and the nuclear Coulomb repulsion is approximated to a constant for a given nuclear configuration. In $\hat{H}_n$ all the electronic terms are neglected but for $V_{el}(\mathbf{R})$ which is the potential of the electrons acting on the nuclei.

We are interested in calculating the electronic energy and DFT is one of the most powerful computational techniques in this regard.

2.1.3 Density functional theory

DFT reduces the dimensionality of the electronic Schrödinger equation even more because it expresses the ground state energy of a system as a function of the electron density. DFT is in principle exact, because there exists a one-to-one correspondence between the the ground state energy of the system and its density, as the first Hohenberg and Kohn theorem states [33]. The energy of the ground state as a function of the density, ρ, reads as:

$$E_0^{el}[\rho] = T^{el}[\rho] + V^{el-n}[\rho] + V^{el-el}[\rho], \tag{2.7}$$

where $T^{el}[\rho]$ is the kinetic energy of the electrons, $V^{el-n}[\rho]$ is the nuclear potential acting on the electrons and $V^{el-el}[\rho]$ is the potential arising from the electron-electron interaction. The definition of $E_0^{el}[\rho]$ by Kohn and Sham [34] overcomes the inaccuracy of the very first attempt by Thomas and Fermi of determining the ground state energy as a function of the density [44, 45]. In the Thomas-Fermi model the kinetic energy of electrons is obtained from the treatment of a system with a homogeneous electron density, like the uniform electron gas. All the many-body interactions such as the electron-electron and electron-nucleus interactions are treated as classical. In the Kohn-Sham equation, $T^{el}[\rho]$ is the kinetic energy of the non-interacting electrons, and all the many-body interactions are then included in the $V^{el-el}[\rho]$ potential which is defined as:

$$V^{el-el}[\rho] = E^{Hartree}[\rho] + E^{xc}[\rho], \tag{2.8}$$

where the $E^{Hartree}[\rho]$ accounts for the Coulomb repulsion between the electrons and the $E^{xc}[\rho]$ accounts for the exchange and electron correlation.

The sum of $V^{el-n}[\rho]$ in Eq. 2.7 and $V^{el-el}[\rho]$ describes the potential due to all the electron interactions which is felt by a single electron. Thus it is possible to write the Schrödinger equation for a single electron as:

$$\left(-\frac{1}{2}\nabla^2 + V^{eff}(\mathbf{r})\right)\phi_0^i(\mathbf{r}) = E_0^i(\mathbf{r})\phi_0^i(\mathbf{r}), \tag{2.9}$$

where $\phi_0^i(\mathbf{r})$ is the Kohn-Sham orbital of the electron i, and $V^{eff}(\mathbf{r})$ is:

$$\begin{aligned} V^{eff}(\mathbf{r}) &= \frac{\delta}{\delta\rho(\mathbf{r})}\left\{V^{el-n}[\rho] + V^{el-el}[\rho]\right\} \\ &= V^{el-n}(\mathbf{r}) + \int \frac{\rho(\mathbf{r}')}{|\mathbf{r}-\mathbf{r}'|}\mathrm{d}^3r' + \frac{\delta E^{xc}[\rho]}{\delta\rho(\mathbf{r})}. \end{aligned} \tag{2.10}$$

The density at the position r is, then, the sum of the the Kohn-Sham orbitals over all the electrons:

$$\rho(r) = \sum_i^N |\phi_0^i(\mathbf{r})|^2. \tag{2.11}$$

The total electronic energy is calculated iteratively by solving equations 2.9 and 2.11. Second theorem of Hohenberg and Kohn [33] states, in fact, that the ground state electron energy can be calculated by using the variational principle. This means that the energy coming from the electron density of the ground state will always be the lowest.

So it seems that we have a solid theory to solve exactly the Schrödinger equation within the Born-Oppenheimer approximation. However this is not possible because an explicit expression of the last term in Eq. 2.10, that is the exchange-correlation functional, is not known. In the next section some of the most popular exchange-correlation functionals developed over the last decades will be discussed.

2.1.3.1 Exchange-correlation functionals

A large number of exchange-correlation functionals have been proposed over the years and still there is a lot of ongoing research to develop functionals that tackle different systems and processes.

The very first approximation proposed by Kohn and Sham makes use of the local

electron density, and is referred to as the local density approximation (LDA). Here the space is represented as a 3 dimensional grid, where the electron density within each infinitesimal cell is uniform. The exchange-correlation energy is then calculated as the energy of the uniform electron gas with that particular density, and the total exchange-correlation energy reads as:

$$E_{xc}^{LDA} = \int \rho(\mathbf{r})\epsilon_{xc}(\rho(\mathbf{r}))\mathrm{d}^3r, \tag{2.12}$$

where $\epsilon_{xc}(\rho(\mathbf{r}))$ is the exchange-correlation energy of the individual space unit. The LDA exchange energy is know exactly, while the formalism of the correlation energy is more complex and usually comes from the interpolation of quantum Monte Carlo values obtained for different densities of the uniform electron gas. Perdew and Zunger (PZ81) [46], Vosko, Will and Nusair (VWN) [47], and Perdew and Wang (PW91) [48] developed some of the most common functionals within the LDA. Although LDA is one of the most popular approximations because of its reasonable performance in describing solid sate at a low computational cost, it fails for systems where the density changes rapidly. This is the reason why it is inappropriate for the study of atoms and molecules.

The next level of approximation, known as the generalized gradient approximation (GGA) [49, 50, 51, 52], tries to overcome the failure of the LDA by adding the gradient of the electron density, $\nabla\rho(r)$, for each infinitesimal volume. The formalism of the GGA functionals is:

$$E_{xc}^{GGA} = \int \rho(\mathbf{r})\epsilon_{xc}(\rho(\mathbf{r}))\nabla\rho(\mathbf{r})\mathrm{d}^3r. \tag{2.13}$$

Perdew, Burke and Ernzerhof developed the PBE functional [53] which is mostly used in solid state and surface calculations. Also the combination of the exchange energy from the Becke's functional (B88) [54] and the correlation from the functional of Lee, Young and Parr (LYP) [55], or from the P86 functional of Perdew [56], are highly used especially for molecular systems. GGA functionals perform better than LDA in predicting the atomization energies, but the description of the structural properties, such as bond lengths and lattice constants, is still not optimal.

The subsequent improvement comes from adding the second derivative or Laplacian, of the electron density gradient, $\nabla^2[\rho(\mathbf{r})]$, in the expression of the exchange-correlation energy. This is a feature of the *meta*-GGA class of functionals. The revised-TPSS (rev-TPSS) [57] is one of the latest functionals of these, and it yields a better description of atomization energies and structural properties with respect

to LDA and GGA [58].

Local or semi-local exchange-correlation functionals lead to a large delocalization of the electrons which results in underestimation of the band gap of insulators and semiconductors. This has been recognized as one of the major pitfalls of standard-density functionals together with the lack of description of long range interactions. In the following paragraphs some of the solutions that have been proposed to alleviate these drawbacks of exchange-correlation functionals will be discussed, however a comprehensive perspective on DFT can be found in Ref. [59] and [60].

One practical solution to the delocalization problem comes from the class of hybrid functionals, wherein a certain fraction of the GGA exchange energy is mixed with the Hartee-Fock (exact) exchange. In contrast to LDA and GGA functionals, the Hartree-Fock approximation localizes the electrons, therefore the combination of the two approximations leads to a better description of band gaps [61]. The most popular hybrid functionals are PBE0 [62], HSE [63] and B3LYP [55, 47, 64].

Mixing DFT and Hartree-Fock approximations however does not solve the lack of description of the long range interactions, commonly referred to as van der Waals (vdW). They arise from the interaction between an instantaneous dipole and the consequently induced dipole in another region of space. The vdW interactions are weak and attractive, which decay as $-1/r^6$, where r is the distance between two atomic entities. The inability of standard DFT to treat the vdW interactions has prevented for years the use of this method to study systems where these are important, such as biomolecules (e.g. proteins, DNA base pairs), liquids, solids or processes like molecular adsorption. Note, some of the standard methods do reproduce the weak binding between molecules, like in the case of the LDA, but this is because of an inadvertent cancellation of errors. Although in some cases LDA predicts the minimum of the potential surface fairly right, it does not predict the correct potential shape. In fact, the standard methods describe the interatomic or intermolecular interactions coming from the density overlap, which decays exponentially with r and does not follow the typical $-1/r^6$ trend which arises from the dispersion interactions. Therefore the work reported in this thesis would not have been possible if new functionals, able to account properly for dispersion forces, were not designed. The recent review in Ref. [35] reports the developments in the field over the last decades, here we used two of the vdW methods for which the details will be reported in the next paragraphs.

The first class of functionals makes use of a correction term that accounts for the dispersion energy, which is added to the total energy calculated with one of the

standard functionals. The general formulation of the dispersion energy is:

$$E_{dis} = -\sum_{A,B} f(\mathbf{r}_{AB}, A, B)\frac{C_6^{AB}}{r_{AB}^6}, \tag{2.14}$$

where r_{AB}^6 is the distance between pair of elements A and B, and C_6^{AB} is the dispersion coefficient that depends on the pair, A and B. $f(r_{AB}, A, B)$ is the damping function which is used to bring the dispersion energy to zero at low values of r. The functionals within this class differ from one to another for the formulation of the C_6^{AB} coefficient. In 2004 Grimme developed the DFT-D functional [65] where the C_6 coefficients are calculated using experimental atomic polarizabilities. These coefficients are constant for different hybridization states of the atoms, so they do not account for the different chemical environments. The DFT-D2 functional [66] was then designed to be more general, using both the atomic polarizabilities and the ionization potentials of single atoms. The chemical environment is then taken into account in the DFT-D3 functional [67], where the C_6 coefficients have been calculated for several pairs of atoms in different hybridization states. Tkatchenko and Scheffler also proposed a functional known as vdW(TS) [68], which still makes use of the C_6 coefficients calculated from the atomic polarizabilities, but it includes the chemical environment by looking at the volume of the atoms. Thus, during each calculation the C_6 coefficient is scaled according to a factor obtained by comparing the electron density of an atom in the system to the density of the free atom.

The second class of functionals does not correct *a posteriori* the total DFT energy, but it calculates the dispersion interactions from the electron density. This is done by expressing the exchange-correlation energy as follow:

$$E_{xc} = E_x^{GGA} + E_c^{LDA} + E_c^{nl}, \tag{2.15}$$

where the first term is the exchange energy of one of the GGA functionals, the second is the local-correlation coming from LDA, and E_c^{nl} is the non-local energy which accounts for the long range interactions. E_c^{nl} is defined as the double integral of the electron density over space:

$$E_c^{nl} = \int\int \rho(r_1)\varphi(\mathbf{r}_1, \mathbf{r}_2)\rho(r_2)\mathrm{d}\mathbf{r}_1\mathrm{d}\mathbf{r}_2, \tag{2.16}$$

and $\varphi(r_1, r_2)$ is the correlation kernel that ensures the right form of E_c^{nl} at small and large distances.

The original formulations proposed by Dion *et al.* in 2004 [69] uses the exchange energy from the revPBE functional [70], and it is referred to as the vdW-DF. This functional however overestimates the binding distance between the molecule and subsequently underestimates the binding energies. With this in mind, a new functional was proposed, the vdW-DF2 [71], where both the exchange and formulation of the non-local correlation energy were changed. The vdW-DF2 gives a better description of the intermolecular binding distance and energy, but its prediction of the C_6 coefficients is not optimal [72]. Functionals like optB88-vdW and optPBE-vdW [36, 37] have been designed in order to improve even further the description of the dispersion forces. These functionals still belong to the class of vdW-DFs given that the exchange-correlation energy is the same as in Eq. 2.15 and the non-local correlation energy is the same as in Eq. 2.16, but the exchange energy comes from an optimized version of B88 and of PBE, respectively. The use of a less repulsive exchange energy results in an improved prediction of the intermolecular binding energy and distance for several systems [36, 37, 73].

In the two classes of dispersion-inclusive functionals just discussed the total dispersion energy arises from the sum of pairwise interactions, only meaning that many-body effects are neglected. The random phase approximation (RPA) [74] is a method based on the adiabatic-connection fluctuation dissipation theorem (ACFDT) which is able to account for the dispersion forces and the many-body effects, however its high computational cost has prevented this functional from becoming widely used in the condensed matter field. Very recently a new formulation of the vdW(TS) method has also been proposed in order to include many-body effects [75] at a reasonable computational cost.

2.1.3.2 Basis functions and Bloch's theorem

In order to practically perform a DFT calculation we need to choose a function which represents the electronic orbitals. These can be described by localized Gaussian functions (commonly used to study molecular systems) or plane waves (commonly used to study solid systems). Because of the nature of the systems that were studied in this work, plane waves were used to describe the electronic orbitals. The periodic shape of this function is particularly useful to describe the orbital of an electron in a solid which constantly experiences a potential with the same periodicity of the crystal. Thus, as Bloch's theorem states, the wavefunction of a single electron can be expressed as the product of a plane wave function and a function which has the

same periodicity of the potential felt by the electron:

$$\phi_{n,k}(r) = \exp(i\mathbf{k}\cdot\mathbf{r}) f_{n,\mathbf{k}}(\mathbf{r}). \tag{2.17}$$

$\exp(i\mathbf{k}\cdot\mathbf{r})$ is nothing but the Fourier transform of the orbital in reciprocal space, $\mathbf{k}$ is a vector in reciprocal space, and n is the index of a set of possible wavefunctions for a given k, which form an electronic band. $\mathbf{k}$ can be chosen within the entire reciprocal space, however since the energy eigenvalues are periodic, that is $\varepsilon_n(\mathbf{k}) = \varepsilon_n(\mathbf{k}+\mathbf{K})$ where $\mathbf{K}$ is a vector of the reciprocal space, $\mathbf{k}$ is usually limited to the first Brillouin zone. The k-space is continuous for an infinite crystal, but for practical calculations we need to use a discrete number of k points. Here the Monkhorst-Pack scheme [76] was used to sample the k-space.

2.1.3.3 Description of the core electrons

In the previous section it was shown that it is possible to describe the orbitals using the plane wave functions. Now, in order to have a good description of the electrons close to the nucleus, which are characterized by fast oscillations, a large number of plane wave functions is required, and this is quite computationally demanding. The first solution to this problem is known as the pseudopotentetial approximation. Here the core and valence electrons are separated and the potential felt by the valence electrons is replaced with a pseudopotential, which acts within a radial cut-off from the nucleus. The pseudopotential can be norm conserving, which means that the norm of the pseudo and real orbitals is the same; alternatively ultrasoft pseudopotentials [77] can be used. In the latter case, the norm of the pseudo and real orbitals is not conserved and this difference can be corrected by adding an extra charge density in the region within the cut-off. Another way of describing the core electrons is by using the projector augmented wave (PAW) method [78]. In this case the wavefunction is calculated from a starting pseudo wavefunction, and it is used to correct the approximated terms which have been calculated from the pseudo wavefunction. Thus the PAW is an all-electron method, but it requires a much smaller radial cut-off compared to the pseudopotential approximation.

2.1.4 Static and dynamic calculations

DFT has been discussed as a very useful tool to look at the properties of materials when the atoms are in static configurations and furthermore dynamical properties

of atoms can also be explored. *Ab initio* molecular dynamics (AIMD) is one of the most popular techniques to calculate dynamical properties of systems with a reasonable number (hundreds) of atoms. It couples MD methods to generate the dynamical trajectory of the atoms in a system with DFT, which is used to calculate the forces acting on the atoms in different configurations. Various methods to couple the dynamics and the force calculations exist, and the most popular ones are the Born–Oppenheimer and the Car–Parrinello [79, 80] approaches. In this work only the former has been used. AIMD yields a pure classical description of the nuclei, and it neglects any quantum behavior of the nuclei. Although this approximation has been shown to give a good description of many systems, it breaks down when we want to look at the dynamics of light nuclei, such as hydrogen but also carbon as will be shown in the next chapters. The first order quantum nuclear effect which is the zero point energy (ZPE) can be included by simply looking at the lattice dynamics with phonons calculations. Path integral molecular dynamics (PIMD) is an efficient way to incorporate higher order quantum nuclear effects (QNE) than ZPE into dynamical simulations [81]. In the next sections a brief description of MD, ZPE calculations and PIMD will be reported.

2.1.4.1 Molecular dynamics

MD is a technique where the trajectory of a N-particle system is calculated by a time integration of the Newton's equation of motion, which is defined as:

$$\mathbf{F}_i = m_i \frac{\mathrm{d}^2 \mathbf{r}_i}{\mathrm{d}t^2}, \tag{2.18}$$

where m_i and $\mathbf{r}_i$ are the mass and the coordinate of the atom i, and $\mathbf{F}_i$ is the force acting on the i-th atom as a result of the interaction with the other N-1 atoms in the system. Therefore it can be calculated from the potential energy, $V(\mathbf{r}_1, ..., \mathbf{r}_N)$, as:

$$\mathbf{F}_i = -\nabla_i V(\mathbf{r}_1, ..., \mathbf{r}_N). \tag{2.19}$$

Equations 2.18 and 2.19 can be solved numerically for a series of small time steps, and an integration algorithm needs to be employed. Among the various algorithms that have been proposed the velocity-Verlet has been used for the calculations in this work. With this algorithm the positions and the velocities are calculated at the same time. It is time-reversible, symplectic and it guarantees good stability. Particular attention needs to be payed to the selection of the time step: it has to

be short enough to preserve a good accuracy of the simulation, but sufficiently long to prevent a steep rise of the computational cost. Generally an appropriate time step should be small enough to sample the fast frequency modes of vibration of the system being examined, and for the study of the solid states a value of 1–2 fs is usually appropriate.

Throughout the MD simulation the number of particles (N), the volume (V) and the total energy of the system (E) are conserved. The trajectory is generated in what is known as the *microcanonical* ensamble, or NVE. In some cases a control over the temperature is advisable and often trajectories are produced in the *canonical* ensamble, NVT, where the temperature (T) is kept constant.

In order to control the temperature many thermostats have been proposed, however in this work we made use of the Nosé-Hoover thermostat. In this case a heat bath is connected to the system and the heat transfer between the two preserves the temperature of the systems from any drift.

2.1.4.2 Zero point energy: Phonon calculations

Standard MD simulations rely on the classical description of nuclei and neglect their quantum nature. First order quantum nuclear effects (QNEs) appear in the zero point energy (ZPE) associated with the energy of the ground state of a system. The ZPE arises from the natural fluctuations of the atoms in a systems even if this is at 0 K. Assuming that the interatomic potential is harmonic, the ZPE is expressed as:

$$ZPE = \frac{\hbar\omega}{2}, \tag{2.20}$$

where $\hbar$ is the reduced Plank's constant and ω is the frequency of a certain mode of vibration of a system.

DFT predicts the energies and forces for the ions at 0 K at the minimum of the potential energy surface thus not including the ZPE contribution. However in order to have information about the thermodynamic properties of a system at a finite temperature, the vibrational contribution can be included in the form of ZPE. One efficient way to calculate the vibrational energies in condensed matter is to integrate the phonon (i.e. vibrational) density of states of a crystal. Phonons are referred to as quasi–particles since they are quantization of the normal vibrational modes in the specific case of a crystal and phonon vectors and frequencies can be obtained from DFT calculations as follows.

The calculated interatomic potential energy is a function of the instantaneous position of the nuclei, thus it can be expanded by adding to the energy for the atoms at the equilibrium position, V_{equi}, the value of the energy for the atomic displacement (u_{li}) from the equilibrium position:

$$V = V_{\text{equi}} + \frac{1}{2} \sum_{li\alpha,l'j\beta} \Phi_{li\alpha,l'j\beta} u_{li\alpha} u_{l'j\beta} \tag{2.21}$$

where $\Phi_{li\alpha,l'j\beta}$ is the force–constant matrix and $u_{li\alpha}$ and $u_{l'j\beta}$ are the displacements of the atoms i and j in the cells l and l' along the Cartesian components α and β. The force–constant matrix relates the forces and the atomic displacements, if the potential is assumed to be harmonic and the anharmonic terms are ignored. The phonon frequencies are then obtained form the diagonalisation of the dynamical matrix which is nothing but a Fourier transform of the force–constant matrix.

The two common methods to obtain the coefficients of the force–constant matrix are known as the finite displacement and the linear response method or density functional perturbation theory (DFPT) [82].

The finite displacement method is very simple: each atom is displaced by a small amount and the forces acting in the new configuration of the atoms are calculated. The elements of the force–constant matrix can then be obtained from the proportionality between the forces and the displacements. This approach requires the use of a supercell so that the effect of a single displacement is negligible at the boundaries of each repeated cell. The use of a supercell can be avoided by calculating the force constant matrix within the framework of DFPT. This approach makes use of the Hellmann-Feymann theorem to show that a linear order perturbation on the crystal corresponds to variation of the electron density of the system, that in turn corresponds to a variation of the energy up to the second order of the perturbation. This implies that it is possible to calculate the energy of a perturbed state using just the wavefunction of the unperturbed state. The same concept can be used when the perturbation is a phonon, and the dynamical matrix can be calculated for any $\mathbf{q}$ vector in the reciprocal space for a given unit cell, without the need of a supercell. More details on DFPT and phonon calculations can be found in Ref. [82].

2.1.4.3 Path integral molecular dynamics

PIMD is one of the methods to account for higher order quantum nuclear effects than ZPE. A complete description of the approach can be found in Ref. [83] . However in brief this technique is based on the idea of the Feynmam path integral which states

that the path of a single quantum particle can be determined as the weighted sum of the infinite possible paths of the classical particle [84]. In other words a quantum particle can be described as an infinite number of replica of classical particles, all connected by harmonic springs. This can be depicted as a ring-polymer where every classical replica is referred to as a bead. The method used in PIMD to sample the phase space of this classical ring-polymer is molecular dynamics. As opposed to phase space, the time space is imaginary. This means that each bead represents an imaginary time segment and MD is merely used to sample configuration states. Real time information, such as structural details of the system can then be achieved by averaging over configurations in imaginary time.

2.2 Experimental techniques

In the previous sections some of the most popular computational tools to describe the structure and dynamics of materials have been briefly discussed. Of course these properties of materials can be determined also experimentally, exploiting the interaction between the atoms and a radiation beam, which can consist of electromagnetic radiation or subatomic particles like electrons or neutrons. In this study neutrons have been selected as the optimal probe to look at layered materials. There are several advantages in using neutrons with respect to other probes like X-rays with the main reason being that neutrons interact directly with the nuclei of the atoms, thus there is no correlation between the atomic number and the power of the scattering event. This is in contrast with X-rays, where the photons interact with the electron cloud and the power of the scattering event is proportional to the atomic number. This is why neutrons are a better choice when looking at systems containing light atoms. In addition, neutrons have a spin so they can interact with the magnetic moments in the sample, being in this way a good probe also for magnetic properties of materials.

Neutrons can be scattered from an atom such that their energy is conserved, this is called elastic scattering and it gives rise to a diffraction process which is used to look at the structure of materials. The energy of neutrons can also change after interacting with an atom, this is called inelastic neutron scattering (INS) and it leads to spectroscopy which is used to study the dynamics of atoms.

In the next sections a general overview of elastic and inelastic neutron scattering and of the instruments that have been exploited in this study will be reported. More detailed explanations of neutron scattering can be found in Ref. [85, 86, 87, 88]

2.2.1 Basics of neutron scattering

A general neutron scattering experiment can be described as a flux of incoming thermal neutrons (Φ) incident on a sample and scattered in solid angle, $d\Omega$, in the directions defined by the angles ϑ and φ, as it is pictured in Fig. 2.1.

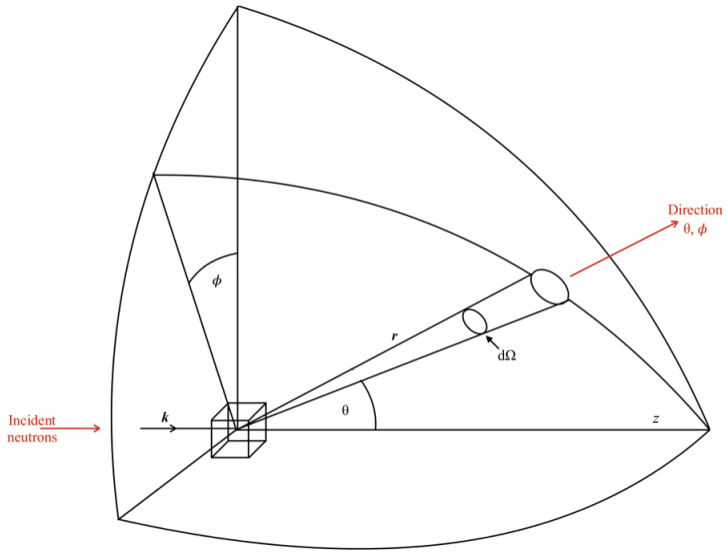

Figure 2.1: Geometry of a general scattering experiment, where an incident neutron beam is scattered by the target (sample) in a solid angle $d\Omega$, defined by the in–plane angles ϑ and φ. This graph has been customised from Ref. [87].

The quantity measured during a neutron scattering experiment is expressed in terms of scattering cross section, σ_{total}, defined as:

$$\sigma_{total} = \frac{\text{total no. of neutrons scatterd per second}}{\Phi}, \tag{2.22}$$

which is nothing but the effective area of a single nucleus that directly interacts with the incident neutrons. Since the nuclear diameter is $\sim 10^5$ smaller than the wavelength of the incoming neutrons, it is possible to treat the nuclei as point scatterers which scatter neutrons isotropically. Thus it is possible to express the incident and scattered wavefunctions as spherically symmetric waves, as reported in Eq. 2.23 and 2.24:

$$\Psi_i = e^{(ikz)}, \tag{2.23}$$

$$\Psi_f = -\left(\frac{b}{r}\right) e^{(ikz)}, \tag{2.24}$$

where k is the magnitude of the wavevector $\mathbf{k}$, z is the position of the incoming neutrons along the axis parallel to the $\mathbf{k}$ wavevector, r is the distance between the nucleus and the scattered waves and b is the scattering length which is a measure of the strength of the neutrons–nuclei interaction. This last parameter is related to the total scattering cross section by the relation:

$$\sigma = 4\pi b^2.$$

The total cross section can also be defined as the integral of the scattering cross section over all the small solid angles as:

$$\sigma_{total} = \int \frac{\mathrm{d}\sigma}{\mathrm{d}\Omega}\mathrm{d}\Omega, \tag{2.25}$$

where $\left(\frac{\mathrm{d}\sigma}{\mathrm{d}\Omega}\right)$ is referred to as differential cross section. Let us assume a system characterised by an initial state λ and final state $\lambda^{'}$ and that the initial neutron wavefunction is ψ_{k} and the final one is $\psi_{\mathrm{k}'}$, it is then possible to calculate the differential cross section as follows:

$$\left(\frac{\mathrm{d}\sigma}{\mathrm{d}\Omega}\right) = \frac{1}{\Phi}\frac{1}{\mathrm{d}\Omega}\sum_{\mathrm{k}' \text{ in } \mathrm{d}\Omega} W_{\mathrm{k},\lambda} \rightarrow W_{\mathrm{k}',\lambda'}, \tag{2.26}$$

where Φ is the flux of incident neutrons and $W_{\mathrm{k},\lambda} \rightarrow W_{\mathrm{k}',\lambda'}$ are the transition per second from the initial to final state. The terms of the sum in Eq. 2.26 can be determined by using the Fermi's Golden rule in conjunction with the Fermi pseudopotential. This pseudopotential is the potential between the nuclei and the neutrons which is assumed to be much weaker than the energy of the incoming neutrons and it allows to assume that the scattered wavefuctions are spherical S-waves. Thus bearing these assumptions in mind it is possible to reformulate the differential cross section as:

$$\left(\frac{\mathrm{d}\sigma}{\mathrm{d}\Omega}\right)_{\lambda\rightarrow\lambda'} = \frac{k}{k'}\left|\int b_j e^{i\mathbf{Q}\cdot\mathbf{r}_j}\mathrm{d}r\right|^2, \tag{2.27}$$

where b_j is the scattering length of the nucleus j in the position $\mathbf{r}_j$ and $\mathbf{Q}$ is the scattering vector defined as $\mathbf{Q} = \mathbf{k}_i - \mathbf{k}_f$.

So far no energy exchange between the sample and the incident neutrons has been taken into account. Let us assume that the incident neutrons have energy E, that the scattered neutrons have energy E' and that the difference between the initial and final energy is $E - E' = \hbar\omega$, where ω are vibrational frequencies. In this case the partial differential cross section is the ration between the number of neutrons with initial energy E and the number of the scattered neutron in the solid angle $\mathrm{d}\Omega$ with a final energy between E' and $E' \pm \mathrm{d}E'$, $N_{\mathrm{d}\Omega\mathrm{d}E'}$ and it reads as:

$$\frac{\mathrm{d}^2\sigma}{\mathrm{d}\Omega\mathrm{d}E'} = \frac{N_{\mathrm{d}\Omega\mathrm{d}E'}}{\Phi\mathrm{d}\Omega\mathrm{d}E'}, \tag{2.28}$$

where Φ is the flux of incident neutrons. It is possible to use the same assumptions as for the differential cross section and so one can express the partial differential cross section as:

$$\frac{\mathrm{d}^2\sigma}{\mathrm{d}\Omega\mathrm{d}E'} = \frac{k}{k'}\frac{1}{2\pi\hbar}\sum_{jj'} b_j b_{j'} \int_{-\infty}^{\infty} \left\langle e^{-i\mathbf{Q}\cdot\mathbf{r}_{j'}(0)} e^{i\mathbf{Q}\cdot\mathbf{r}_j(t)} \right\rangle e^{-i\omega t}\mathrm{d}t, \tag{2.29}$$

where b_j and $b_{j'}$ are the scattering lengths for the nucleus j and j' respectively and the first term of the integral is the average over all the starting times of observation of the system in the range from 0 to time t.

It is also possible to express the partial differential cross section considering the correlation between the particles of the system. In this case Eq. 2.29 will read as:

$$\frac{\mathrm{d}^2\sigma}{\mathrm{d}\Omega\mathrm{d}E'} = \frac{k}{k'}\frac{1}{2\pi\hbar}\left[\begin{array}{l} \bar{b}_j^2 \sum_{jj'} \int_{-\infty}^{\infty} \left\langle e^{-i\mathbf{Q}\cdot\mathbf{r}_{j'}(0)} e^{i\mathbf{Q}\cdot\mathbf{r}_j(t)} \right\rangle e^{-i\omega t}\mathrm{d}t \; + \\ (\bar{b}_j^2 - \overline{b^2} \sum_j \int_{-\infty}^{\infty} \left\langle e^{-i\mathbf{Q}\cdot\mathbf{r}_{j'}(0)} e^{i\mathbf{Q}\cdot\mathbf{r}_j(t)} \right\rangle e^{-i\omega t}\mathrm{d}t \end{array}\right], \tag{2.30}$$

where the first term in the square brackets is known as coherent scattering and refers to the correlation between the different nuclei on the system, which causes interferences effects and provides information about the structure of the sample. The second term is known as incoherent scattering and is related to the correlation between the position of the same nucleus at different time, so it provides information about the dynamics of the system.

2.2.2 Elastic neutron scattering: Diffraction

The diffraction process can be described as the results of the collision between radiation - in this case a neutron beam - and a particle, that occurs when the normal to one of the planes of a crystal and the incident radiation form a specific angle. Thus if we assume that the wavelength of the neutron beam is comparable to the interatomic distance in a material, and that the beam is scattered in the same way by the atoms of the same species (coherent scattering), then it is possible to use Bragg's diffraction law to gain information about the structure of a material. Bragg's law states that the distance between two planes (d) in a crystal is proportional to an integer multiple (n) of the wavelength of the incident radiation (λ):

$$n\lambda = 2d\sin\theta, \tag{2.31}$$

where θ is the the angle between the incident and scattered beam.

One of the most popular approaches to determine d is known as time–of–flight (TOF), which involves measuring the time taken by a neutron to go from the source to the detector, passing through the sample. By combining the de Broglie equation and Bragg's law, λ can be determined as:

$$\lambda = \frac{ht}{mL} = 2d\sin\theta, \tag{2.32}$$

where m is the mass of the neutron, h is Planck's constant and t is the time for a neutron to cover a distance L, which is the distance between the source and the detector. Consequently d can be calculated as:

$$d = \frac{ht}{2mL\sin\theta}. \tag{2.33}$$

So for each detector, which is fixed at a specific Bragg's angle θ, the intensity of the radiation is calculated as a function of the TOF.

The intensity of the scattered beam is expressed as the weighted average of the square of the total scattering $\rho(\mathbf{Q})$:

$$S(\mathbf{Q}) = \left\langle |\rho(\mathbf{Q})|^2 \right\rangle = \sum_{i,j} b_i b_j \left\langle \exp(i\mathbf{Q}\cdot(\mathbf{r}_i - \mathbf{r}_j)) \right\rangle, \tag{2.34}$$

where b_i and b_j are the scattering lengths, $(\mathbf{r}_i - \mathbf{r}_j)$ is the distance between the pair of particles i and j, and $\mathbf{Q}$, is the scattering vector. Since the diffraction process is elastic, that is the energy between the incident and scattered remain unchanged, the scattering vector $\mathbf{Q}$ is defined as the difference between the incident wave vector $\mathbf{k}_i$ and the scattered vector $\mathbf{k}_s$:

$$\mathbf{Q} = \mathbf{k}_i - \mathbf{k}_f, \tag{2.35}$$

with $|\mathbf{k}_i| = |\mathbf{k}_f|$.

Single-crystal diffractometer SXD [89] at the ISIS spallation neutron source was used in this work to look at the structure and displacement of the atoms of graphite. Here a polychromatic neutron beam is scattered by a single crystal sample and the scattered radiation is analysed by large-area position sensitive detectors. The Bragg's peaks are then obtained by looking at the neutron TOF. However the intensity of the Bragg peaks is attenuated by the thermal motion of the atoms and it appears as intensity away from the Bragg condition, called diffuse scattering. The atomic displacement, $\mathbf{u}$, is related to the Debye-Waller factor [90, 91], DW, by the following relation:

$$DW = \langle \exp(i\mathbf{Q} \cdot \mathbf{u}_i) \rangle^2 , \tag{2.36}$$

where $\mathbf{u}_i$ is the displacement of the atom i from its average position, and the brackets denote a thermal average. The Debye-Waller factor is a Gaussian envelope that describes the decrease of the intensity of the Bragg peaks with increasing $\mathbf{Q}$. Thus in order to reduce the effect of the Debye-Waller factor one can either reduce the atomic displacement by performing neutron scattering experiments at very low temperatures, or reduce $\mathbf{Q}$ by looking at small diffraction angles. Although diffuse scattering is generally neglected, it contains together with the Debye-Waller factor useful information about the dynamics of the atoms in the crystallographic network as will be shown in Chapter 4.

2.2.3 Inelastic neutron scattering: Spectroscopy

The scattering process can be used to explore the dynamics of the atoms in a system by looking at the energy difference between the incident and scattered beam. In the case of INS, the scattering vector is defined as in Eq. 2.35 with $|\mathbf{k}_i| \neq |\mathbf{k}_s|$, however the total energy and the momentum are conserved.

We now look how to relate the energy difference between the incident and scattered radiation to the atoms dynamics. Eq. 2.34 refers to the scattering intensity in the case of all pairs of atoms scattering at the same time, however scattering at different times reflects into a change of the energy of the scattered beam of $E = \hbar\omega$, where ω is a specific frequency of vibration of the atoms in the system. Thus the integration of the total scattering $\rho(\mathbf{Q}, t)$ over the time yields the complete form of the scattered beam intensity which reads as:

$$S(\mathbf{Q}, \omega) = \sum_{i,j} b_i b_j \int \left\langle \exp(i\mathbf{Q} \cdot \mathbf{r}_i(0)) \exp(-i\mathbf{Q} \cdot \mathbf{r}_j(t)) \right\rangle \exp(-i\omega t) \mathrm{d}t. \tag{2.37}$$

One can note that Eq. 2.37 is the time Fourier transform of the scattered intensity, so that the it can be measured in the energy or frequency domain.

In vibrational spectroscopy neutrons interacts with the vibrations of the atoms in the crystal, by gaining or losing energy in the form of a phonon, which are quanta of the lattice vibrations. As already mentioned in the previous section, the atoms moves around their average position in the crystal, and $\mathbf{u}_i$ is the measure of the displacement, so the instantaneous position of the i-th atom at time t can be defined as:

$$\mathbf{R}_i(t) = \mathbf{r}_i + \mathbf{u}_i(t).$$

Taking into account the instantaneous positions of the atoms, the function which describes the scattering involving a single phonon becomes:

$$\begin{aligned} S(\mathbf{Q}, \omega) &= \sum_{i,j} b_i b_j \exp(i\mathbf{Q} \cdot (\mathbf{r}_i - \mathbf{r}_j) T_i(\mathbf{Q}) T_j(\mathbf{Q}) \\ &\quad \times \int \left\langle [\mathbf{Q} \cdot \mathbf{u}_i(t)] \left[\mathbf{Q} \cdot \mathbf{u}_j(0) \right] \right\rangle \exp(-i\omega t) \mathrm{d}t, \end{aligned} \tag{2.38}$$

where $T_i(\mathbf{Q})$ and $T_j(\mathbf{Q})$ are the temperature factors, which are a reformulation of the Debye-waller factor in Eq. 2.36.

The TOSCA INS spectrometer at the ISIS neutron spallation source is an example of an instrument that can be used to gain information about molecular vibrations. It is an indirect geometry spectrometer, which means that it keeps $|\mathbf{k}_s|$ fixed, and it is used to explore the molecular region of the mid-infrared region (32-4000 cm^{-1}) [92, 93, 94]. The TOSCA spectrum shares the same resolution of a Raman or in-

frared spectrum, however, since the neutrons interacts with the nuclei, the neutron spectroscopy does not follow any selection rule and it can access modes of vibrations which are forbidden in the Raman and infrared spectroscopy.

INS can be also used to study nuclear quantum dynamics by looking at the atomic momentum distribution of individual atoms in a system. This can be achieved by exploiting the interaction between high energy neutrons (with energies > 1 eV) and the sample, and the high momentum transfer. This technique is called deep inelastic neutron scattering (DINS) [95] and it can be performed using the VESUVIO spectrometer [96] at the ISIS neutron spallation source.

At the other extreme, it is possible to use "cold neutrons" to explore molecular dynamics in a longer time-frame such as rotation or diffusion processes. OSIRIS [97, 98, 99] is the inverted-geometry spectrometer at the ISIS facility which allows to perform low-inelastic or quasi-elastic spectroscopy.

Chapter 3

Structural and energetic assessment of soft layered materials using van der Waals density functional theory

3.1 Introduction

In the previous chapter it was largely discussed how the accurate description of vdW forces within DFT is currently one of the most active areas of research in computational physics and chemistry. The fervent research into vdW forces is also driven by a desire to overcome the challenge they represent for theoretical approaches based on density functional theory (DFT). Indeed several schemes within DFT have now been proposed that account for dispersion in one way or another [100, 101, 102, 103, 69, 67, 68, 104, 105]. Although the accuracy of these methods has been established in many circumstances – particularly for purely vdW bonded systems – how they perform in the description of systems where both strong (covalent and ionic) and weak (vdW) bonding is involved is less clear. Layered materials are the perfect template to benchmark the performances of these new functional within DFT. Their anisotropic nature, with strong covalent intralayer bonds and much weaker interlayer bonds, dominated by vdW interactions, makes them challenging and intriguing materials to explore with theory. Here results on the structural and energetic properties of two layered materials, graphite and *hexagonal*-boron nitride (h-BN), are presented.

Graphite and h-BN are interesting materials to compare because, despite their different chemical composition, their interlayer spacings are essentially the same,

but why this is so is not completely understood. Furthermore, these two materials are also technologically appealing because of their characteristic anisotropy which is, of course, also key to many applications (e.g. lubrication [2], batteries [21], or gas storage [21, 29, 30, 106, 17]).

Graphite and h-BN have been widely examined before with theoretical methods and are increasingly being considered as model benchmark systems against which new methods are tested [107, 108, 109, 110, 111, 104]. By now, it is largely recognized that the PBE functional within the generalized–gradient approximation (GGA) fails to reproduce any significant interlayer bonding and that LDA gives bulk properties that are closer to experiment [107, 108, 109, 110, 112]. However, the superior performance of LDA in this regard has been explained in Chapter 2 to be fortuitous, as LDA relies on a local description of exchange and correlation and does not account for non–local interactions. Several of the functionals developed to give a more accurate treatment of vdW forces, (e.g. the approaches based on C_6 corrections to DFT [65, 68] and vdW-DF and vdW-DF2) have already been applied to graphite and h-BN and do, on the whole, offer improved performance [103, 113, 114, 115, 65, 116]. Also, highly expensive approaches based on the random phase approximation (RPA) [74] and quantum Monte Carlo (QMC) have been applied, yielding interlayer binding energies in good agreement with experiment [104, 117, 111].

A study of the intralayer and interlayer binding of graphite and h-BN obtained with the optB88-vdW and optPBE-vdW functionals as well as several others (LDA, PBE, PBE with the empirical dispersion correction of Grimme [66] and vdW-DF2) is presented in the following sections. Results from a variety of other functionals and theoretical methods are also brought together so that a clear picture of the current state of the field can be obtained. Moreover, a brief analysis of the nature of the interlayer bonding in both materials is presented.

3.2 Computational details

The DFT calculations have been performed with the periodic plane–wave basis set code VASP 5.2 [118, 119, 120] and six different exchange-correlation functionals, namely, LDA, PBE, PBE with an empirical dispersion correction of Grimme (DFT-D2), vdW-DF2, optB88-vdW, and optPBE-vdW. The calculations with the vdW correlation functional have been carried out self–consistently using an implementation [37] of the vdW-DF method [69] in VASP with the scheme of Román–Pérez

and Soler [121].

PAW potentials have been used, with LDA–based PAW potentials for the LDA calculations and PBE potentials for the PBE and all the various vdW–DF based calculations. For the calculations with the optB88-vdW functional both LDA and PBE potentials have been used and it was found that the bond lengths and energies obtained differed by $<$0.001 Å and $<$1 meV, respectively. This suggests that for the systems considered here it is not necessary to generate new PAW potentials for the various vdW-DFs. The vdW-DFs treat the exchange–correlation energy as defined by Eq. 2.15 where the first two terms, the exchange and LDA correlation energies, are calculated considering all the electrons within the PAW method as in the PBE calculations. While the last term, the non–local correlation energy, is calculated within a pseudopotential approximation, it has been shown to represent a valid approximation on a wide range of systems [37]. All results reported have been obtained with hard potentials using a very high 900 eV plane–wave cut–off. Tests with standard PAW potentials and a 600 eV cut–off yielded very similar results. Specifically differences in calculated distances were $\lesssim \pm 0.002$ Å and differences in calculated energies were $\lesssim \pm 0.02$ eV for the atomization energy and ± 2 meV for the interlayer binding when normal and hard PAWs were compared. However the somewhat extreme settings used in this study are justified by the desire to provide a well–converged set of results.

Two atom 7 Å high unit cells were used to calculate bond lengths and bond strengths within the isolated two–dimensional graphite or h-BN layers. The unit cells used to calculate the interlayer distances in bulk graphite and h-BN contained two AB-stacked layers. Periodic boundary conditions have been applied and thus the two layers in the unit cell are representative of the entire periodic crystal. The interlayer distance was changed by varying the cell dimensions along the z-axis over the range 5–14 Å. The h-BN calculations were also performed using an AA' stacking sequence where boron and nitrogen were placed on top of each other. We used a Monkhorst-Pack k-point grid of $24 \times 24 \times 2$ per (1×1) unit cell for graphite and $8 \times 8 \times 2$ per (1×1) unit cell for h-BN, which ensured that bond lengths and energies were converged to within 0.01 Å and 1 meV, respectively.

Atomization energies (E_{atom}) are defined as:

$$E_{\mathrm{atom}} = \frac{E_{\mathrm{lay}} - E_{\mathrm{isolated}}}{2}, \tag{3.1}$$

where E_{lay} is the total energy of a single layer of graphite or h-BN in the 2 atom

unit cell, and E_{isolated} is the total energy of the isolated atoms in the gas phase. The energies of the isolated atoms were obtained from spin-polarized calculations in a $12 \times 14 \times 16$ Å^3 box with Γ-point sampling of k space.

The interlayer binding energies of the bulk materials have been calculated by subtracting twice the energy of an isolated monolayer of graphite or h-BN (E_{lay}) from the energy of a graphite or h-BN bulk slab (E_{bulk}) and dividing this value by the total number of atoms (N) in the unit cell:

$$E_{\text{inter}} = \frac{E_{\text{bulk}} - 2E_{\text{lay}}}{N}. \tag{3.2}$$

Because of the periodic boundary conditions, the calculated interlayer binding energy represents the energy difference per layer between the bulk and the isolated layers. Hanke [116] and Björkman *et al.* [38] have shown, based on additivity arguments, that the interlayer binding energy is equivalent to the exfoliation energy. The latter is the energy required to take off the top layer from the material surface as measured by Zacharia *e*t al. for graphite [122].

The effects of zero–point–energy (ZPE) on the interlayer binding energy and binding distance have been estimated by considering a first–order harmonic correction to the interlayer potential energy. In this case, the ZPE is simply given by half the characteristic vibrational frequency. This ZPE contribution is added to the total dissociation energy which assumes static (i.e., infinitely heavy) atomic nuclei. The displacement due to ZPE motions has been estimated by calculating the average distance of the ZPE level on the binding energy curves reported in Figs. 3.1 and 3.2. Overall, as shown in Tables 3.2 and 3.4, ZPE effects are small in these systems ($\lesssim 5$ meV and $\lesssim 0.05$ Å on interlayer binding energies and distances) and insensitive to the functional used.

The elastic constant in the c–direction (C_{33}) has been calculated for both materials from the second derivative of the interlayer binding curve with respect to interlayer spacing c using:

$$C_{33} = \frac{2c_0}{\sqrt{3}a_0^2} \frac{\partial^2 E}{\partial c^2}. \tag{3.3}$$

Here, c_0 is the interlayer distance corresponding to the minimum, $\sqrt{3}a_0^2$ is the area of the unit cell, and E is the total energy.

3.3 Results

3.3.1 Graphite

Table 3.1 reports results for the C–C bond length and atomization energies for a single layer of graphite (graphene) obtained with the various functionals used in this study. From Table 3.1 it can been seen that all functionals considered give similar values for C–C bond lengths, $1.41 - 1.42$ Å in very good agreement with experiment. Turning to the atomization energies, LDA substantially overestimates the atomization energy by almost 20%, in line with previous calculations [107]. The other functionals offer much better agreement with experiment, coming within about 5% of the experimental value. The optB88-vdW functional performs particularly well in this regard, predicting an atomization energy essentially the same as the zero point energy corrected experimental value of -7.5 eV/atom.

Table 3.1: C–C bond lengths and atomization energies for a single layer of graphite (graphene) obtained in this work along with a comparison with other theoretical results and experiment. The experimental value for the atomization energy with zero point energy (0.16 eV) [123] removed is reported in square brackets.

Method	**Bond length (Å)**	E_{atom} **(eV/atom)**
This work:		
optB88-vdW	1.422	-7.55
optPBE-vdW	1.426	-7.65
vdW-DF2	1.428	-6.95
DFT-D2	1.424	-7.99
LDA	1.412	-8.96
PBE	1.424	-7.93
Other work:		
LDA	1.413 [107]	-8.89 [107]
vdW-DF for layered materials	1.426 [103]	–
RPA	–	~ -7.0 [104]
Experiment	1.421 [124]	~ -7.37 [107] [-7.53]

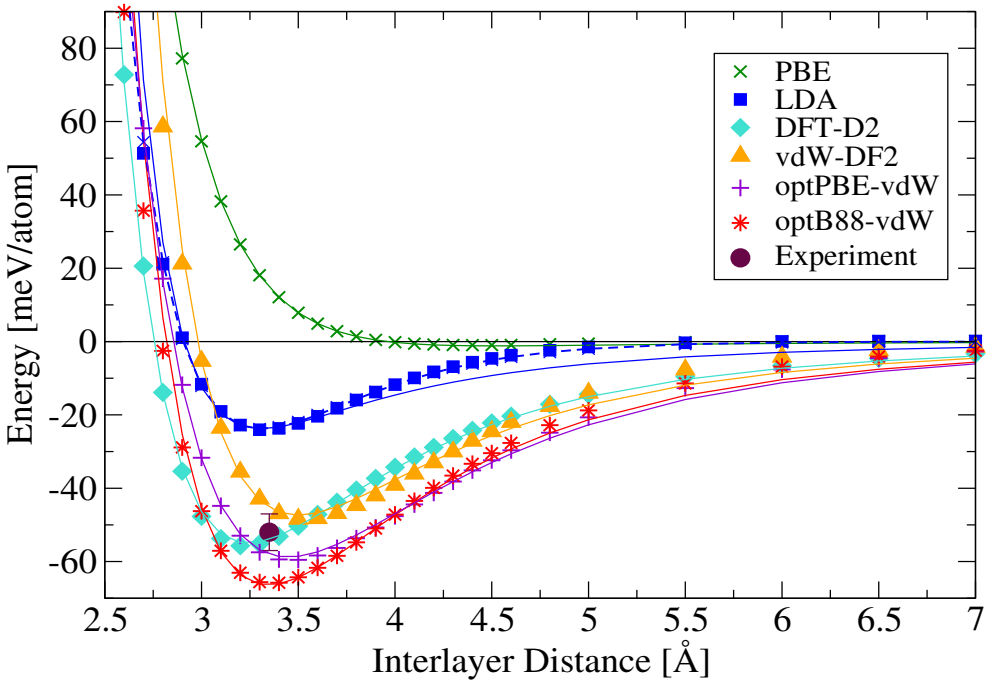

Figure 3.1: Binding energies as a function of interlayer distance in graphite. The discrete computational data (symbols) have been fitted to the potential: $E = a_0 \exp(-b_0 x) + e_0/x^4$ [125]. As the LDA considers atomic attraction to be dependent on electron–density overlap, the LDA fit (dark blue line) shows that the $1/x^4$ asymptotic behavior is not recovered. Better agreement is obtained when the second term is replaced by $a_1 \exp(-b_1 x)$ (dashed dark blue line). Experimental values are taken from Ref. [124] for the interlayer distance and from Ref.[122] for the energy.

The experimental interlayer spacing of graphite is well established at 3.33 Å [124]. The interlayer binding energy (exfoliation energy) is less well established and has been estimated to be -52 ± 5 meV/atom from extrapolations based on temperature programmed desorption experiments of polycyclic aromatic hydrocarbons from the basal plane of graphite [122]. Accurate explicitly correlated electronic structure techniques (QMC [111] and RPA [104]) agree well with the experimental interlayer spacing (Table 3.2) and predict interlayer binding energies which straddle the experimental value (-48 to -56 meV/atom), suggesting that the estimated experimental value is reasonable. The results for graphite interlayer distances and interlayer binding energies obtained with the various functionals considered in this study are reported in Table 3.2 and Figure 3.1. These show, as seen before, that PBE gives essentially no binding between the layers, except for a very shallow minimum (~ 2 meV/atom) at around 4 Å. Fortuitously, LDA predicts a binding energy minimum in good agreement with the experiment (3.31 Å). However, the binding

energy is underestimated (−20 meV/atom) and the energy incorrectly decays exponentially as the layer separation is increased (Figure 3.1), since LDA does not take explicit account of long–range interactions. Turning now to the functionals which account for dispersion, clear improvements are observed. DFT-D2 reproduces very well the interlayer binding energy, predicting a value of −52 meV/atom but slightly underestimates the interlayer distances by $\sim 3\%$ (3.21 Å). vdW-DF2 also predicts the interlayer binding energy in good agreement with experiment (−48 meV/atom), but overestimates the interlayer spacing by $\sim 6\%$ (3.54 Å) in the reported calculations. The optB88-vdW functional gives both an interlayer distance and binding energy in reasonable agreement with experiment: 3.36 Å and −65 meV/atom, respectively. Still better agreement is obtained with optPBE-vdW for the binding energy (−60 meV/atom), but in this case the interlayer distance is overestimated by $\sim 5\%$ (3.46 Å). In previous vdW-DF calculations, using either the original Dion *et al.* version of vdW-DF or vdW-DF2, good values for the interlayer energy were obtained but the interlayer distances were overestimated by about 0.2 Å [113] and 0.1 Å [114, 126], respectively, and in line with the results obtained with vdW-DF2 in this work. Hence, it is shown here that the optB88-vdW and optPBE-vdW functionals offer a slight improvement over previous vdW-DF calculations. Likewise for this system the new vdW functionals outperform the Tkatchenko–Sheffler (TS) correction scheme, which although often very accurate, predicts a large interlayer binding energy of −85 meV/atom.

Table 3.2: Interlayer distances, interlayer binding energies, and elastic constant, C_{33}, for graphite obtained in this work along with a comparison with other calculations and experiment. Values in square brackets have been corrected for ZPE effects as described in the text.

Method	**Interlayer distance (Å)**	$\mathbf{E_{inter}}$ **(meV/atom)**	C_{33} **(GPa)**
This work:			
optB88-vdW	3.36 [3.39]	−65 [−61]	38
optPBE-vdW	3.46 [3.48]	−60 [−56]	32
vdW-DF2	3.54 [3.58]	−48 [−44]	33
DFT-D2	3.21 [3.27]	−55 [−52]	36
LDA	3.31 [3.36]	−24 [−21]	31
PBE	~ 4	~ -2	–
Other work:			
LDA	3.29 [107]	–	–
	3.30 [111]	−24 [111]	–
	3.33 [117]	−24 [117]	–
	–	–	29 [127]
vdW-DF	3.76 [103]	−24 [103]	–
for layered materials	3.76 [128]	−22 [128]	–
vdW-DF	3.59 [113]	−53 [113]	–
vdW-DF2	3.47 [114]	−53 [114]	–
	3.48 [126]	−53 [126]	–
TS-PBE	3.33 [116]	−85 [116]	–
DFT-D3	–	−49 [65]	–
RPA	3.34 [117]	−48 [117]	–
QMC	3.35 [111]	−56 [111]	–
Experiment	3.33 [124]	-52 ± 5 [122]	36 ± 1 [127]

In addition, the elastic constant in the c direction, C_{33}, has been calculated for

each functional (except for PBE for which essentially no binding is obtained). The results in Table 3.2 show that all functionals predict a value within ±4 GPa of experiment (36 ± 1GPa) [127]. Particularly good is the performance of the DFT-D2 and optB88-vdW functionals which yield values of 36 and 38 GPa, respectively.

3.3.2 *Hexagonal*-boron nitride

Let us now turn to *h*-BN and consider how the various functionals perform for B–N bond length and atomization energies, and then interlayer binding. Table 3.3 reveals that, as with graphite, all functionals give values for the B–N bond length ($\sim$ 1.45 Å) in very good agreement with experiment. [129] From the computed atomization energies, LDA gives a slightly large value (−8.1 eV/atom) in line with previous LDA calculations [130] and vdW-DF2 slightly underestimates this energy. All other functionals give similar atomization energies of around −7.0 eV/atom.

Table 3.3: B–N bond lengths and atomization energies for a single layer of *hexagonal*-boron nitride obtained in this work along with a comparison with other theoretical results and experiment.

Method	**Bond length (Å)**	E_{atom} **(eV/atom)**
This work:		
optB88-vdW	1.449	−7.04
optPBE-vdW	1.452	−6.91
vdW-DF2	1.455	−6.66
DFT-D2	1.450	−7.08
LDA	1.437	−8.03
PBE	1.450	−7.02
Other work:		
LDA	1.420 [130]	−8.09 [130]
	1.435 [131]	–
vdW-DF for layered materials	1.449 [103]	–
Experiment	1.446 [129]	–

Concerning interlayer distances, the experimental value is the same as graphite, 3.33 Å [132]. For the interlayer binding energy, experimental values are not available, however some preliminary considerations can still be made. The results for h-BN interlayer distances and interlayer binding energies calculated with the functionals considered in this study are reported in Table 3.4 and Fig. 3.2. The results show that, as with graphite, PBE does not reproduce any binding between layers, except for a negligible minimum (~ -2 meV/atom) at around 4 Å. LDA gives better results than PBE since it predicts a clear interlayer binding minimum at 3.21 Å of -28 meV/atom. vdW-DF2 predicts an interlayer binding energy in the same range as for graphite but, as in the case of graphite, overestimates the interlayer spacing by $\sim 5\%$. The optPBE-vdW and optB88-vdW functionals reproduce interlayer distances in good agreement with experiment, $\sim 3.3 - 3.4$ Å, and the calculated interlayer binding energies obtained are around $60 - 65$ meV/atom. Quite large values for the binding energy are also obtained in our DFT-D2 calculations, ~ -80 meV/atom, and a rather poor interlayer separation of 3.08 Å is obtained. Indeed the interlayer binding energy predicted by DFT-D2 is almost 20 meV larger than it is for graphite. This is inconsistent with the other approaches (all the vdW-DFs and PBE-TS) and due to the particular choice of C_6 coefficients used in the DFT-D2 scheme, as discussed in the next section. The computed binding energies cannot at this point be compared to experiment but they can, of course, be compared to previous theoretical work with vdW-corrected DFT approaches. This reveals that the values obtained sit roughly in the middle of a broad range which extends from -26 to -86 meV/atom. The -26 meV/atom value comes from the vdW-DF for layered materials introduced in Ref. [103]. This appears to be an unrealistically low value for the binding energy since it is similar to LDA and also associated with a large interlayer spacing of 3.6 Å. The vdW-DF and vdW-DF2 functionals also predict rather large interlayer spacings of 3.54 and 3.44 Å, respectively, with interlayer binding energies both of -51 meV/atom, in line with the calculations performed with the vdW-DF2 functional in this work. At the upper end of the range is the PBE-TS scheme. It seems likely that, as was the case with graphite, this functional slightly overestimates the interlayer binding energy. However, the interlayer spacing predicted by PBE-TS coincides exactly with the experimental value.

Table 3.4: Interlayer distances and interlayer binding energies for *hexagonal*-boron nitride obtained in this work along with a comparison with other calculations and experiment. Values in square brackets have been corrected for ZPE effects as described in the text.

Method	**Interlayer distance (Å)**	$\mathbf{E_{inter}}$ **(meV/atom)**	C_{33} **(GPa)**
This work:			
optB88-vdW	(AB) 3.30 [3.31]	−65 [−60]	–
	(AA') 3.30 [3.32]	−65 [−60]	34.4
optPBE-vdW	(AB) 3.40 [3.41]	−60 [−56]	–
	(AA') 3.41 [3.42]	−60 [−56]	28.1
vdW-DF2	(AB) 3.51 [3.54]	−47 [−43]	–
	(AA') 3.49 [3.55]	−47 [−43]	28.3
DFT-D2	(AB) 3.07 [3.10]	−79 [−74]	–
	(AA') 3.08 [3.11]	−77 [−71]	55.0
LDA	(AB) 3.21 [3.29]	−28 [−24]	32.4
PBE	∼ 4	∼ −2	–
Other work:			
LDA	(AA') 3.24 [130]	–	–
	(AB) 3.24 [131]	–	–
	(AA') 3.25 [131]	–	–
vdW-DF for layered materials	3.63 [103]	−26 [103]	–
vdW-DF	3.54 [114]	−51 [114]	–
vdW-DF2	3.44 [114]	−51 [114]	–
TS-PBE	(AA') 3.33 [115]	−86 [115]	–
RPA+	3.31 [133]	–	–
Experiment	(AA') 3.33 [132]	–	32.4 [134]

Also for *h*-BN the C_{33} constant has been evaluated (Table 3.4). In this case the

spread of results for each functional is larger than we saw for graphite. LDA performs particularly well, predicting a value in very good agreement with experiments. The DFT-D2 functional, that performed very well for graphite, predicts a C_{33} (55.0 GPa) $\sim$ 70% larger than experiment (32.4 GPa) [134]. The optPBE-vdW and the vdW-DF2 functionals predict values about 4 GPa smaller than experiment while optB88-vdW predicts a value 2 GPa larger.

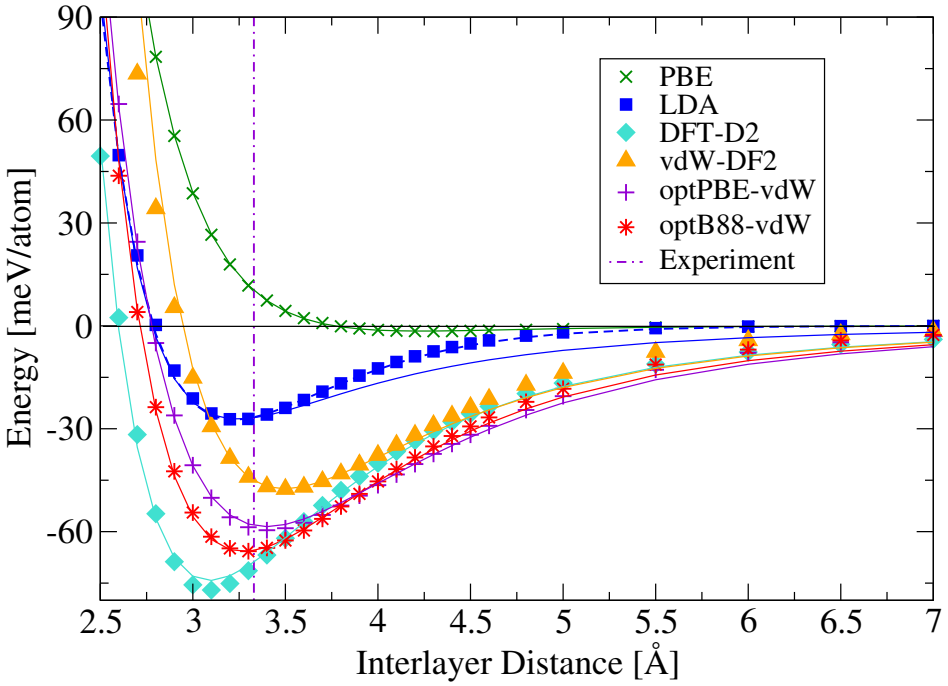

Figure 3.2: Binding energies as a function of interlayer distance in *hexagonal*-boron nitride with the AA' stacking. The discrete computational data (symbols) have been fitted to the potential: $E = a_0 \exp(-b_0 x) + e_0/x^4$. [125] As the LDA considers atomic attraction to be dependent on electron-density overlap, the LDA fit (dark blue line) shows that the $1/x^4$ asymptotic behavior is not recovered. Better agreement is obtained when the second term is replaced by $a_1 \exp(-b_1 x)$ (dashed dark blue line). The experimental value of the interlayer distance (indicated by the vertical line) is taken from Ref. [132].

3.4 Discussion and conclusion

It is interesting at this stage to compare the values obtained for the interlayer binding energy of graphite and *h*-BN. Looking at the results from all the functionals considered in this study and in previous work, almost all predict that the interlayer binding energy of graphite and *h*-BN is the same to within a few meV. The excep-

tion is the DFT-D2 approach which, because of the larger average C_6 coefficient of boron and nitrogen compared to carbon [1], predicts an interlayer binding energy $\sim 30\%$ larger for h-BN compared to graphite. The interlayer separation predicted by DFT-D2 for h-BN is also considerably shorter than the values obtained from the other functionals and so it looks likely that DFT-D2 is overestimating the interlayer h-BN interaction. Since all the other approaches predict such similar interlayer binding energies, it is interesting to consider why this is the case. To this end we decomposed the various contributions to the interlayer binding energies obtained from optB88-vdW. Specifically we decomposed the interlayer binding energy, $E_{\mathrm{inter(tot)}}$ in to:

$$E_{\mathrm{inter(tot)}} = E_{\mathrm{local(c)}} + E_{\mathrm{nl(c)}} + E_{\mathrm{rest}}, \tag{3.4}$$

where $E_{\mathrm{local(c)}}$ is the local correlation contribution to the total interlayer binding energy, $E_{\mathrm{nl(c)}}$ is the non–local correlation energy to it, and E_{rest} is the remaining contribution to the binding energy coming from all other components of the Kohn-Sham energy. The results obtained from this decomposition for the optB88-vdW functional at an interlayer separation of 3.3 Å are reported in Fig. 3.3. The first thing to notice from Fig. 3.3 is that all the components of the total energy are very similar and that there are no dramatic differences between the two materials in terms of the overall bonding decomposition. Looking more closely, however, one can see that the local correlation energy contribution is almost the same for both graphite and h-BN ($\sim$ 1 meV larger for h-BN) while the non–local correlation energy is $\sim$ 6 meV more negative (i.e., more attractive) for graphite than for h-BN. On the other hand the rest of the energy where the exchange and the electrostatic contributions are included, is $\sim$ 8 meV larger for graphite (i.e., more repulsive). Although all these energy differences are small, it is clear therefore that graphite and h-BN have similar interlayer binding energy because the stronger electrostatic interaction of h-BN (due to the polarity of the material) is compensated for by the stronger dispersive

[1] The relevant C_6 coefficients in DFT-D2 are: $C_6^B = 3.13$, $C_6^C = 1.75$, $C_6^N = 1.23$ (see Ref [66]). This leads to a C_6^{BN} coefficient $\sim 10\%$ larger than C_6^{CC}, which agrees very well with the observed 9 meV difference between interlayer binding energies of graphite and h-BN. In contrast, the optB88-vdW and optPBE-vdW functionals reproduce almost the same interlayer binding energy for both materials. We therefore compared the non–local corrections for graphite and h-BN obtained with the optB88-vdW functional with the D2 corrections for both materials. The non–local corrections for graphite and h-BN are $E_c^{nl}(G) = 116$ meV and $E_c^{nl}(BN) = 110$ meV, respectively. In order to compare these values with the D2–corrections, DFT-D2 calculations with the LDA correlation energy have been performed since the non-local correction contains some PBE–like semilocal correlation (see Eq. 2.15). We observed also in this case that the D2–correction for h-BN is ~ 9 meV larger than that for graphite, while the van der Waals scheme produced non–local corrections ~ 6 meV smaller.

interaction in graphite. This analysis is consistent with the excellent recent study of by Björkman *et al.* [38], which found similarities in interlayer binding energies for a large class of layered materials. In agreement with our analysis, this was attributed to a balance between repulsion and attractive interactions.

Finally, to conclude, we have presented results from a range of exchange–correlation functionals for the binding in graphite and h-BN. This has included results from the new optB88-vdW and optPBE-vdW functionals and a comparison with previous dispersion–corrected DFT studies on graphite and h-BN. Overall it is possible to conclude that the optB88-vdW and optPBE-vdW functionals provide a fairly computationally inexpensive means (e.g., compared to PBE, the calculation of bulk graphite takes $\sim 24\%$ more time) of obtaining reasonably accurate interlayer and intralayer structural and energetic properties for both graphite and h-BN. These functionals offer better performance than the original vdW-DF of Dion *et al.* for graphite and h-BN. An improved agreement with the experimental values has been obtained especially in the description of structural parameters, intralayer bond lengths and interlayer spacings. Recent studies have found that these improvements also apply to graphene interacting with metal surfaces and for bulk metals [37, 135, 136]. This, along with previous work with the optB88-vdW and optPBE-vdW functionals [36, 37, 73, 137, 138, 139, 140], suggests that a much broader range of systems can now be tackled with confidence with these functionals. There is, of course, much scope for improvement with regard to dispersion–corrected DFT studies of metals and semi–metals, in particular in understanding the role of many body correlation [35, 75, 141]. Despite the obvious differences, it was shown that graphite and h-BN have similar interlayer spacings and interlayer binding energies. The analysis of the various contributions to the interlayer binding energy reveals that this results from a cancellation of two terms. The polar nature of the h-BN means that the electrostatic contribution to the binding energy is more favorable than in graphite, an effect which is compensated for by the slightly greater dispersive contribution to interlayer binding in graphite. In Chapter 5 it will be shown that a similar compensation of electrostatic and dispersion applies to the adsorption of small molecules not only on the surface of graphite and h-BN, but also on the surface of other layered materials.

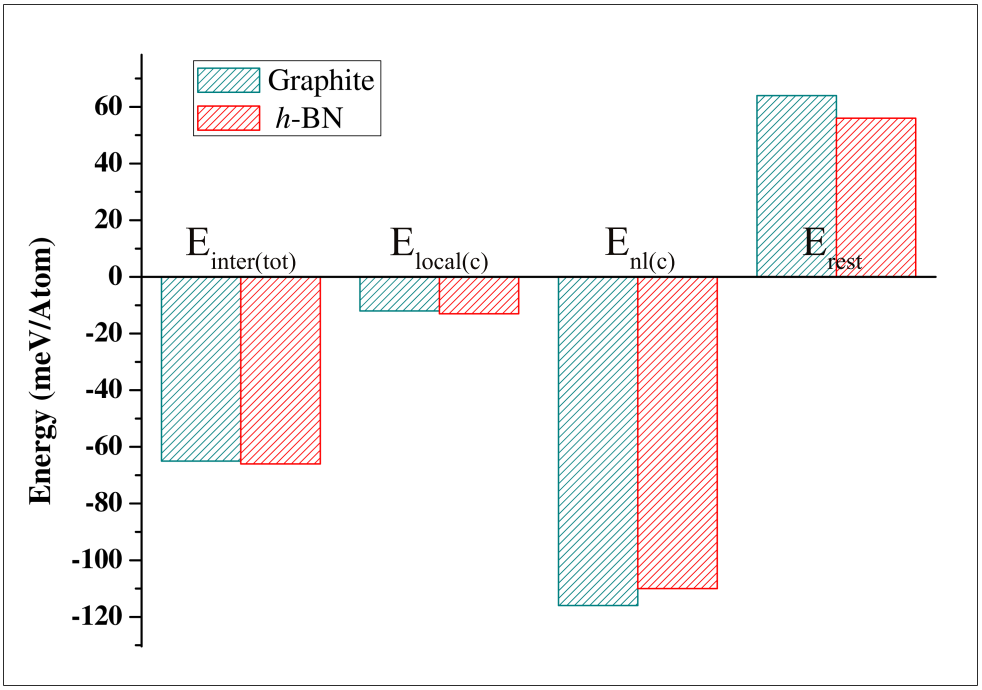

Figure 3.3: Decomposition of the interlayer binding energies of graphite and h-BN obtained with the optB88-vdW functional for an interlayer distance of 3.3 Å. The columns on the left are the total interlayer binding energies ($E_{\mathrm{inter(tot)}}$), which are decomposed into local correlation ($E_{\mathrm{local(c)}}$), non–local correlation ($E_{\mathrm{nl(c)}}$) and the remaining Kohn-Sham energy (E_{rest}) respectively.

Chapter 4

Theoretical and experimental study of the dynamics of carbon atoms in graphite

4.1 Introduction

Graphite has been studied so far in numerous ways, from both experimental and theoretical perspectives. Most of the time these studies have highlighted important physical and chemical properties of graphite that have then been exploited for sophisticated technological applications, from lubricant [2] to the use in battery technology [142], just to mention two of them. However still major gaps remain in the full physical description and understanding of some properties of graphite. For example, in Chapter 3 it was discussed that a feasible theoretical approach within DFT, which allows to look properly at the structure and energetics of the intra– and inter–layer bonds in graphite, became available only in the last decade. This approach can now be used to look at the dynamics of the carbon atoms in and out of the hexagonal network, which is still not completely understood.

An experimental description of the phonon dispersion in graphite has been reported in the literature, where inelastic X-ray and Raman spectroscopy have been used to get an accurate determination of the frequencies of vibration [143, 144, 145, 146, 147, 148, 149, 150, 151, 152, 153]. Theoretical works based on *ab initio* methods have also been reported in the literature [154, 127, 155]. Wirtz and Rubio [154], and Mounet and Marzari [127] predicted the phonon dispersion relation of graphite in good agreement with experiment using DFT at the local and semi–

local level of approximation (LDA and GGA). These predictions were then used to deeply understand the features of the phonon dispersion relation of graphite, like the electron-phonon coupling [155, 149, 156] which affects the high frequency modes of vibration in graphite, or to extract information about other properties like the thermal expansion [127]. The following study is instead devoted to investigate the nature of the carbon dynamics in graphite, especially along the c direction of the crystallographic cell. The contribution of the harmonic, anharmonic and higher order nuclear quantum effects in the modes of vibration as a function of temperature have been explored. In order to gain an in depth understanding of the carbon dynamics in graphite, anisotropic displacement parameters (ADPs) at different temperatures have been explored with a combination of experimental and theoretical techniques.

ADPs are defined as the second moment of the atomic probability distribution function, related to the displacement of the atoms in a crystal with respect of their average positions [157]. These parameters can be easily extracted by structure refinement of X-ray or neutron diffraction patterns by looking at the thermal diffuse scattering, which arises in a perfect crystal form the displacement of the atoms from their average position due to atomic vibrations. ADPs, by containing information about the atomic motion, can be used as additional parameters to explore the stability of certain bonds in materials as a function of temperature and spatial direction [158]. This is strictly connected with the study of phase transitions [159] and the degree of disorder of different materials [160]. In addition, the atomic displacement as a function of temperature is of great importance for the study of thermal and electronic transport in thermoelectric materials [161, 162, 163]. However, an accurate measurement of the ADPs requires high quality single crystals and powerful diffractometers. Single crystals are needed in order to access directly the atomic displacement along the three spatial directions. This process would be otherwise more complex and less accurate in the case of a powder where the atomic displacement is averaged along the different spatial directions. In addition in order to get a good resolution of the Bragg peaks powerful diffractometers are also needed. These are the main reasons why ADPs have not generally been measured, in fact a single crystal neutron scattering measurement of graphite is still not reported in the literature.

In the next sections the results of an accurate single crystal neutron diffraction (SXND) experiment will be discussed. These measurements were performed in order to obtain information about the ADPs of graphite as a function of temperature.

The experimental results have also been compared with theoretical predictions. Gutmann *et al.* implemented a formalism to extract ADPs from the eigenvectors and frequencies computed using DFT [159]. This new implementation overcomes the limitations of the standard calculations of ADPs based on the rigid-body model that in most cases does not account for the correlation between the internal modes of vibration and the translational modes [157, 159]. However there are several other approaches for examining the dynamics of solids from which ADPs can be computed. An estimate of the atomic displacement has been obtained also by using *ab initio* molecular dynamics (MD) and *ab initio* path integral molecular dynamics (PIMD). The availability of high quality experimental data allows us to compare and evaluate the different approaches to look at the solid dynamics. Indeed the comparison between the theoretical and experimental ADPs has highlighted not only that the carbon dynamics is highly anharmonic, especially along the c direction, but that it is also affected by higher order quantum nuclear effects, beyond the zero point energy.

The experimental and computational settings used for this study are reported in the Section 4.2. Section 4.3 show the results of the SXND experiment and DFT calculations which is then followed by a discussion and conclusion in Section 4.4.

4.2 Methods

4.2.1 Experimental details

The diffraction pattern of a single crystal graphite of 2 mm width from Nanotech Innovation was investigated at different temperatures, namely 5, 50, 100, 200 and 300 K, using the SXD diffractometer at the ISIS pulsed neutron source in the UK.

SXD is located on the 50 Hz S3 beamline of the first target station at ISIS. The sample environment is positioned at 8.3 m from the moderator and is shined on by a polychromatic neutron beam (wavelengths in the range of 0.2–10 Å) with a section of 12 mm in diameter. 11 large–area–position–sensitive detectors, which are placed at fixed angles collect the scattered neutrons as a function of their time–of–flight (TOF). Each detector consists of 64×64 optically encoded ZnS scintillators, with an active area of 192×192 mm^2 and a 3×3 mm^2 resolution. The large detectors together with the possibility of rotating the sample along two different axes allow a large section of reciprocal space to be mapped. The detector positions and the distance of the sample from the detectors were previously calibrated by looking at

the positions of the Bragg peaks of a sample with a known unit cell. A V/Nb sphere was also used to establish the incident neutron flux viewed by the detectors [89].

The single crystal graphite was mounted on a conic metallic support using a silver-glue and wrapped with a thin aluminium foil. The sample was accurately positioned at the centre of the rotational system and at the centre of the neutron beam, by using a laser that aligned along the neutron beam direction and an equipment that replicates the geometry of the sample. Once the sample was carefully positioned, the instrument was evacuated and the diffraction patterns were measured for several crystal orientations (0°, 30°, 50°, 70°, 90°, 110° and 130°); this procedure allows a complete sampling of the first Brillouin zone.

4.2.1.1 Structure refinement

The data for each temperature and orientation were treated with the SXD2001 software [164]. The lattice parameters were obtained by refining the position of the measured Bragg peaks and the structure factors (i.e. intensities of the Bragg peaks) by using the procedure that follows. Possible Bragg peaks were searched for each of the collected frames of data. Then the matrix **U** which describes the orientation of the cell axes with respect to the laboratory coordinate system, and the matrix **B**, which represents the lattice vectors in an orthonormal setting, were generated in order to account for most of the peak positions based on the expected crystal unit cell. The **UB** matrices, cell constants and other experimental parameters were then refined using all the identified Bragg peaks in order to optimise the agreement between observed and expected position of the peaks [89]. The ADPs along with the atomic coordinates were refined with the JANA2006 software [165], which is based on the Levenberg-Marquart least squares algorithm, using the structure factors obtained form SXD2001.

4.2.2 DFT and phonon calculations

The DFT calculations were performed with the periodic plane–wave basis set code, VASP 5.3 and six different exchange-correlation functionals: LDA, PBE, PBE-D2, vdW-DF2, optB88-vdW, and optPBE-vdW. Hard PAW potentials using a cut–off of 900 eV were used, with LDA–based PAW potentials for the LDA calculations and PBE potentials for the other functionals. A four atom unit cell was first optimised so that the forces acting on the atoms were converged to within 1×10^{-3} eV/Å and the total energy for each geometrical step was converged to within 1×10^{-7} eV.

Reciprocal space was sampled using a Monkhorst-Pack k-point grid of 24×24×2 per (1×1) unit cell of graphite.

The real–space force constants were calculated in a 2×2×1 supercell using density functional perturbation theory (DFPT) [82], and eigenvectors and phonon frequencies were extracted using the Phonopy software [166]. From the computed eigenvectors and frequencies it was possible to extract the ADPs. The ADP, $u_{kl,n}$ for a specific atom, n is the element of the thermal displacement tensor in the directions defined by the indexes k and l and it can be calculated as the integral of the phonon frequencies, $\omega_{\vec{q}}$, and the eigenvectors $\vec{e}_{\vec{q}k,n}$,

$$u_{kl,n} = \frac{1}{2m_n} \int \frac{\hbar}{\omega_{\vec{q}}} [\vec{e}_{\vec{q}k,n} \cdot \vec{e}^{*}_{\vec{q}l,n}] \coth\left(\frac{\hbar\omega_{\vec{q}}}{2k_B T}\right) \mathrm{d}\omega \mathrm{d}q. \tag{4.1}$$

Here m_n is the atomic mass of carbon, $\vec{e}^{*}_{\vec{q}l,n}$ is the eigenvector complex conjugate, and $\coth\left(\frac{\hbar\omega_{\vec{q}}}{2k_B T}\right)$ accounts for the phonon population as a function of the temperature.

The intensity $I_{TDS}(\vec{q})$ of the thermal diffuse scattering can be calculated as follows:

$$I_{TDS}(\vec{q}) = C \sum_{j=1}^{n_{branches}} \frac{1}{\omega_{\vec{q}j}} \coth\left(\frac{\hbar\omega_{\vec{q}}}{2k_B T}\right) \cdot |F_j(\vec{q})|^2, \tag{4.2}$$

where F_j is the one-phonon structure factor and reads as:

$$\begin{aligned} F(\overrightarrow{q}) = \; & \textstyle\sum_{n=1}^{n_{atoms}} \frac{b_n}{\sqrt{m_n}} \cdot \exp(-\frac{1}{2} \sum_{k=1}^{3} \sum_{l=1}^{3} u_{kl,n} q_k q_l \;) \\ & \times (\overrightarrow{q} \cdot \overrightarrow{e}_{q,n,j}) \cdot \exp(-i \overrightarrow{q} \cdot \overrightarrow{x}_n), \end{aligned} \tag{4.3}$$

where m_n, b_n and $\overrightarrow{x}$ are respectively the mass, the neutron scattering length and the coordinate in an orthonormal crystal basis of the nth atom in the unit cell.

4.2.3 *Ab initio* molecular dynamics simulations and path integral molecular dynamics

Ab initio MD simulations have been performed at 50, 100, 200 and 300 K in a 8×8×1 supercell. The systems were first equilibrated by running a simulation in the canonical ensemble for about 30 ps with a time step of 2 fs. The Nosé-Hoover thermostat has been selected and the wavefunction was calculated using the optB88-vdW functional and the CP2K code [167]. After the equilibration, the simulations ran for about 40-50 ps with a time step of 2 fs and using the microcanonical ensemble.

The trajectories of the atoms were extracted and for each of them the variance of the position was calculated. An estimate of the ADPs was then calculated as the average of the variance of all the atoms.

Quantum nuclear effects have been taken into account by running PIMD simulations at 50 and 200 K in a 8×8×1 graphite supercell, for 5 ps with a time step of 1 fs. These simulations were performed using the i-PI code [168] for the calculation of the nuclear dynamics and the CP2K code for the calculation of the forces, again using the optB88-vdW functional. The i-PI code makes use of the coloured-noise, generalized Langevin equation thermostat [169, 170, 171] and it is designed to reduce the number of replicas in the quantum simulations. Thus it was possible to use only 16 replicas and still obtain a good picture of the carbon nuclear quantum dynamics at 50 and 200 K. This number of replicas was decided upon after running test calculations of the out–of–plane ADP, u_{33}, of graphene at 50 K as a function of the number of beads. The simulations were performed using the i-PI code for the calculation of the nuclear dynamics and the LAMMPS code [172] for the calculation of the forces, using the Tersoff graphene potential [173, 174] optimised by Lindsay and Broido [175]. By using the force field approach for the calculation of the forces it was possible to run simulation for 30 ps with a time steps of 1 fs, on a graphene sheet of 960 atoms and using up to 64 replicas of the system. Fig. 4.1 shows that 16 replicas is a good compromise between convergence and computational cost. The ADPs were then calculated as of the average of the variance of all the atoms for each replica. It must be noted that the u_{33} obtained for graphene are almost one order of magnitude larger than graphite (Fig. 4.10). This can be due to a higher out–of–plane mobility of the carbon atoms in graphene, where the vibrations of the atoms will be less hindered because of the absence of neighbouring layers [176].

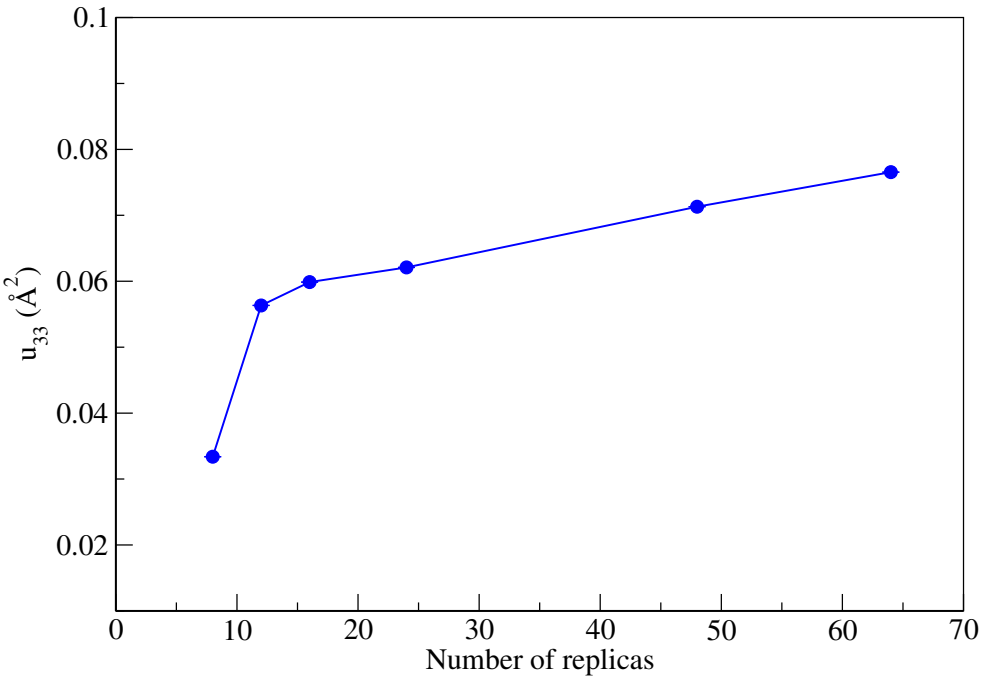

Figure 4.1: u_{33} calculated for different numbers of path integral replicas, from 8 to 64 at 50 K. The simulations were performed using the i-PI code for the calculation of the nuclear dynamics and the LAMMPS code for the calculation of the forces, using the optimized Tersoff graphene potential.

4.3 Results

4.3.1 Graphite lattice constant and thermal expansion

From the SXND experimental data, like the one reported in Fig. 4.2, it has been possible to extract the lattice constants of graphite at different temperatures. Table 4.1 shows that the unit cell of graphite expands with temperature, however because of its anisotropy, the expansion along the c axis (0.60%) is larger than that along the a and b axis (0.06%).

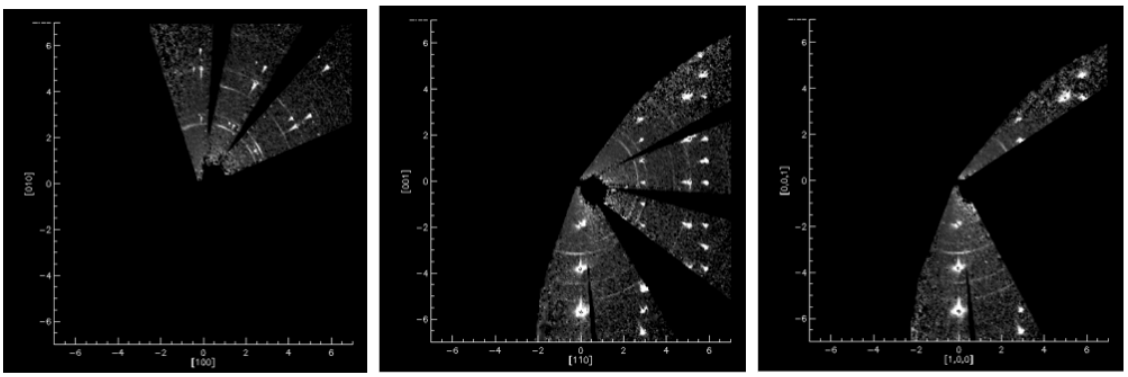

(h k 0) (0 k l) (h 0 l)

Figure 4.2: Graphite diffraction patterns at 300 K obtained on the SXD diffractometer at the ISIS neutron source facility in Didcot. The left panel shows diffraction along the hk0 crystallographic direction, the panel one shows diffraction along the 0kl direction and the panel on the right shows diffraction along the h0l direction.

Table 4.1: Graphite lattice constants a, b and c as a function of temperature obtained with single crystal neutron diffraction experiment.

Temperature (K)	$\boldsymbol{a = b}$ **(Å)**	$\boldsymbol{c}$ **(Å)**
5	2.4610±0.0015	6.6719±0.0060
50	2.4613±0.0016	6.6768±0.0056
100	2.4616±0.0016	6.6808±0.0060
200	2.4624±0.0016	6.6958±0.0062
300	2.4615±0.0016	6.7117±0.0064

The experimental results in Table 4.1 are in line with previous X-ray single crystal diffraction measurements performed as a function of temperature [177, 178]. Baskin and Meyer found c lattice constants of 6.672±0.001 Å, 6.676±0.001 Å and 6.708±0.001 Å at 4.2, 78 and 297 K, respectively [177]. The measurements of Nelson and Riley focused more on the expansion of graphite at higher temperature, however they found a c lattice constant of 6.7117±0.0001 Å, and an a lattice constant of 2.45626±0.0001 Å at 288 K [178], which agrees with the values at 300 K in Table 4.1. Interestingly Nelson and Riley looked for the first time at the negative expansion of the a lattice constant in the range of temperatures from 288 to 873 K. This effect is due to the anisotropic expansion of the cell, that is larger along c than within

the layer. In fact in this range of temperature the thermal energy activates the vibrations of the atoms out–of–plane, thus the projection of the atomic positions on the *ab* plane results in a contraction of the in–plane lattice constants. Whereas at higher temperature the thermal energy is equally absorbed by the phonons along both directions, balancing the expansion of both lattice constants [178]. The results reported here have been obtained at low temperatures, where the a lattice constant is barely affected by such a small thermal energy exchange. However the values of a between 200 and 300 K might indicate the observation of a small lattice contraction in the present measurements.

In Chapter 3 the performance of different functionals (standard and vdW inclusive ones) in describing the structure of graphite was assessed. All the functionals used in this study predict the in–plane lattice constants within 0.5% of the experimental value at 5 K, (Tables 3.2). This lattice constant is a measure of the length of the covalent bond of carbon atoms in graphite and the prediction of such a structural feature is accurate for standard exchange–correlation functionals. Turning to the out–of–plane properties, Tables 3.2 has shown that optB88-vdW gives the best description; for this reason most of the calculations presented in the next sections are performed using this functional.

4.3.1.1 Graphite phonon dispersion relation

Once it was assessed that both experiment and theory yield a good description of the structure of graphite, the carbon dynamics were analysed, specifically looking at the phonon properties. Fig. 4.3 shows the phonon dispersion distribution of graphite, that is the phonon frequencies for each q point of the Brillouin zone as computed with optB88-vdW. The phonon properties were calculated also with the other functionals and the left part of Fig. 4.3 reports the results of the vibrational density of states (v–DOS) obtained with optB88-vdW and the other functionals.

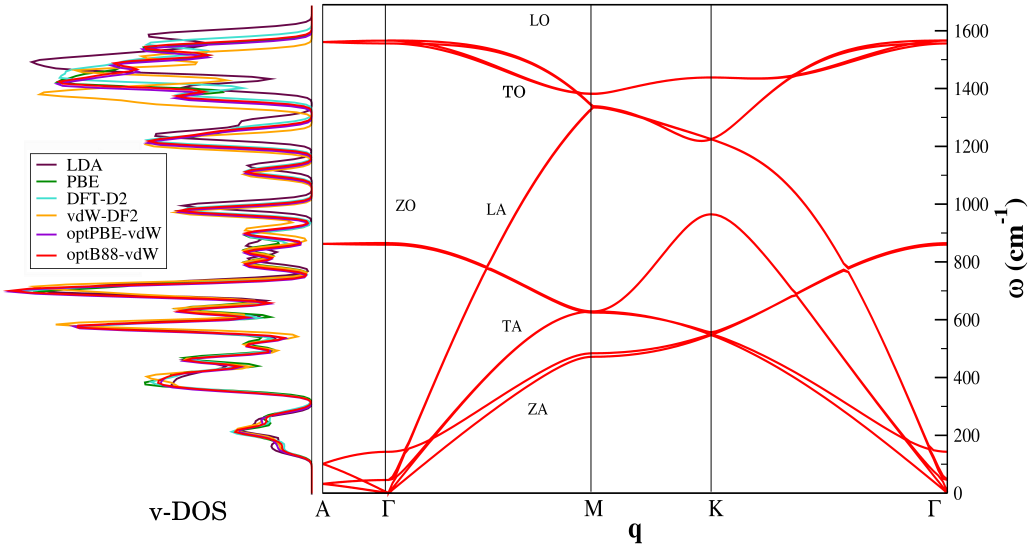

Figure 4.3: (Right) Phonon dispersion relation of graphite calculated with the optB88-vdW functional. The frequencies of each phonon branch as a function of the q point of the Brillouin zone are in cm^{-1}. The high symmetry points of the Brillouin zone are highlighted on the x axis. (Left) The vibrational density of state (v–DOS) calculated with different functionals is represented on the left panel.

Fig. 4.3 reveals that the description of low frequency modes of vibrations is not significantly affected by the choice of the exchange–correlation functional. This result is somehow counterintuitive because of the different performance of the functionals in the prediction of the structure and energetics of graphite, especially where long range vdW interactions are important. In fact, Fig. 3.1 in Chapter 3 shows the different descriptions of the interlayer binding energy as a function of the interlayer distance in graphite, obtained with different functionals. However looking closer one can notice that although the position of the potential minimum is different for each functional, the amplitude of the curves, that is the amplitude of the expansion of all graphite layers is very similar. This similar curvature of the potential curves could explain the similarity of the phonon dispersion curves. However this still does not explain why PBE completely fails in the description of the inter–layer energetics but gives reasonable values for the phonon eigenvectors and frequencies, if the lattice parameters are constrained to the experimental values. This has been investigated by looking at an extremely large displacement of the layers resembling the out–of–plane acoustic mode of vibration (ZA) in graphite. The results of the interlayer binding energy as a function of the fractional coordinates of one of the layers in graphite unit cell are reported in Fig. 4.4. Despite the different values of the energy, the shape of the potentials is similar for all the functionals tested and

this can explain the similarity of the v–DOS at low frequencies.

At high frequencies the v–DOS appears to be slightly more affected by the choice of the functional. The high frequency modes of vibration are related to the in–plane dynamics of the atoms, and they are more sensitive to the value of the bond length, as previously shown by Mounet and Marzari [127]. LDA slightly underestimates the carbon–carbon bond length (∼2.45 Å) compared to the other functionals (∼2.46 Å) and this is reflected in a ∼ 4% overestimation of the average value of the high frequency optical phonon modes, as it can be seen from the dark purple curve in Fig. 4.3. On the other extreme there is the vdW-DF2 which overestimates the carbon–carbon bond length (∼ 2.47 Å) compared to the other functionals and to experiment. This leads to a ∼ 3% underestimation of the high frequency optical phonon modes, as showed from the yellow curve in Fig. 4.3.

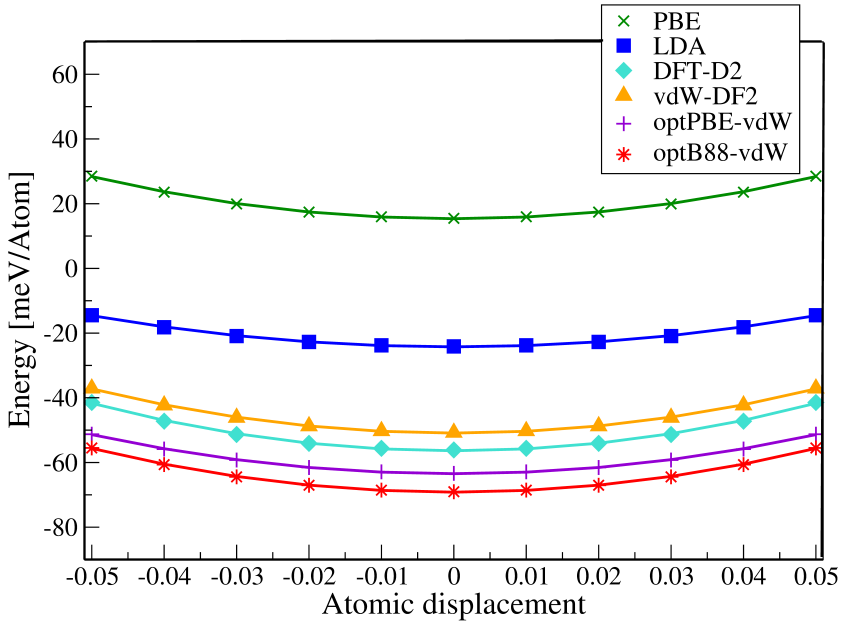

Figure 4.4: Interlayer binding energy as a function of the interlayer distance in the fixed unit cell. The discrete computational data point have been fitted to a harmonic potential. Although the energy is very much dependent on the functional, the shape and amplitude of the potential energy is not.

The graphite v–DOS has also been measured experimentally using the TOSCA spectrometer at ISIS. The results of this experiment are still under examination and more details about it are reported in Appendix A. However it is still possible to benchmark the present phonon calculations by comparing the phonon frequencies calculated with optB88-vdW with the experimental values in Ref. [145, 179, 154, 150]. Table 4.2 shows that the low frequency modes, that is ZA, TA, and LA are

predicted within a few cm^{-1}, usually no more than ~ 10 cm^{-1}, of the experimental values especially around the A and Γ points. The high frequency modes, that is LA, TO, and LO are not described as well by this functional and by standard DFT in general. Table 4.2 shows that the high frequency optical mode of vibration, TO and LO at the Γ point are ~ 18 cm^{-1} lower than the experiment. At the M point the predictions of the frequency of the LA and TO modes are overestimated by ~ 43 cm^{-1} and ~ 15 cm^{-1} respectively with respect to the experiment. The opposite trend is observed for the LO mode, which is ~ 57 cm^{-1} lower than the experimental value. Finally at the K point the prediction of the LA mode is closer to experiment, however the prediction of the frequencies of the TA and TO modes are ~ 40 cm^{-1} overestimated and underestimated respectively. This is due to the known failure of standard DFT in capturing the Kohn anomalies in graphite, which are described as the attenuations of the phonon frequencies due mostly to the electron-phonon coupling [155, 127]. Mauri and coworkers show that approaches beyond standard DFT are needed in order to grasp a very accurate description of the electron-phonon coupling [155, 127]. However it will be shown in the next section that this poor performance of the standard DFT functionals is not going to affect the final results and conclusions of this study.

4.3.2 Anisotropic displacement parameters

We now discuss the ADPs at different temperatures which have been calculated from the computed eigenvectors and frequencies and have been compared to experiment. The experimental ADPs were extracted from the single crystal diffraction pattern at different temperatures after the structure refinement procedure. Atomic displacements are closely related to the thermal diffuse scattering which is visible around the Bragg reflections in X-ray and neutron diffraction patterns, as shown in Figs. 4.5 and 4.2. The temperature increase induces a larger atomic displacement which in turn increases the thermal diffuse scattering in the diffraction pattern. Fig. 4.6 shows the simulated diffraction patterns of single crystal graphite at different temperatures calculated from Eq. 4.2 using the eigenvectors and frequencies obtained from the phonon calculations with the optB88-vdW functional. Here the effect of temperature on the diffuse scattering is evident. Because of the anisotropy of graphite, the carbon displacement along the c lattice vector, i.e. in the h0l plane, is more distinctive than along the a and b vectors (hk0 plane). The same behaviour is then reflected in the values of the ADPs.

Table 4.2: Comparison of the phonon frequencies calculated with the optB88-vdW functional and experimental values reported in the literature.

q point	**Mode**	ω **(cm^{-1})**	ω **(cm^{-1}) Exp.**
A	ZA	101	∼92 [145, 179]
	TA	32	∼38 [145, 179]
	LA	32	∼38 [145, 179]
	ZO	861	–
	TO	1559	–
	LO	1559	–
Γ	ZA	143	∼129 [145, 179]
	TA	0	–
	LA	45	43 [150]
	ZO	859	868 [154], ∼863 [145]
	TO	1564	1582 [154]
	LO	1564	1582 [154]
M	ZA	∼470	∼460 [145]
	TA	∼628	∼629 [145]
	LA	1333	1290 [154], 1290 [145]
	ZO	∼628	∼629 [145]
	TO	1337	1323 [154]
	LO	1333	1390 [154]
K	ZA	547	∼565 [145]
	TA	963	1008 [145]
	LA	1224	1194 [154], ∼1209 [145]
	ZO	547	∼565 [145]
	TO	1224	∼1265 [154]
	LO	1438	–

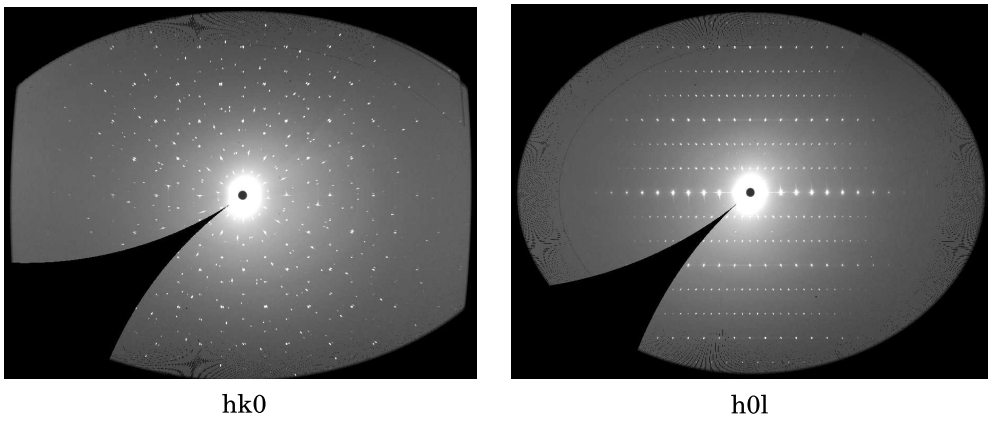

Figure 4.5: Graphite diffraction patterns at 300 K obtained on the BW5 high-energy X-ray diffractometer at the HASYLAB/DESY in Hamburg. The left panel shows diffraction along the hk0 crystallographic direction. The panel on the right shows diffraction along the h0l crystallographic direction, where the characteristic graphite layered structure along the c axis is apparent, from the arrangement of the Bragg peaks along equally spaced horizontal lines.

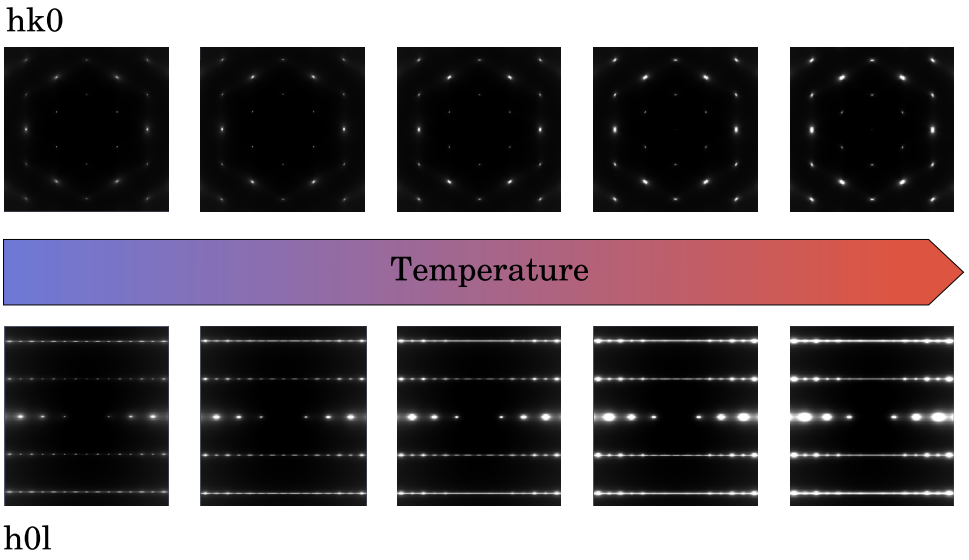

Figure 4.6: Single crystal graphite diffraction pattern at different temperatures (5, 50, 100, 200, 300 K), calculated with optB88-vdW functional. The upper panels show the atom diffraction along the hk0 crystallographic plane, where the typical hexagonal pattern is depicted. The upper panels show the atom diffraction along the h0l crystallographic plane, where the typical layered structure is depicted. The diffraction pattern show how the diffuse scattering increase with the temperature. The thermal diffuse scattering has been calculated from Eq. 4.2, using the eigenvectors and frequencies from the phonon calculations using the optB88-vdW functional.

The atomic displacement is usually described by ellipsoids, where the amplitude

in the three spatial dimensions are the ADPs, u_{11}, u_{22} and u_{33}. The experimental thermal displacement of the carbon atoms in graphite is reported in Fig. 4.7, where one can see how the ellipsoids become more elongated along the c axis with temperature. The results of the computed and experimental ADPs are summarized in Fig. 4.8 and Fig. 4.10. Let us look first at the ADPs of the atoms in the in-plane directions, namely u_{11} and u_{22} reported in Fig. 4.8. The u_{11} and u_{22} at 5, 50, and 100 K calculated from Eq. 4.1 are in very good agreement with experiment. At higher temperatures (200 and 300 K) this theoretical prediction overestimates the experimental ADPs by as much as $\sim 50\%$, especially at 300 K. This disagreement can be explained as the failure of the harmonic approximation at higher temperature, where the atomic vibrations can no longer be safely assumed to be harmonic.

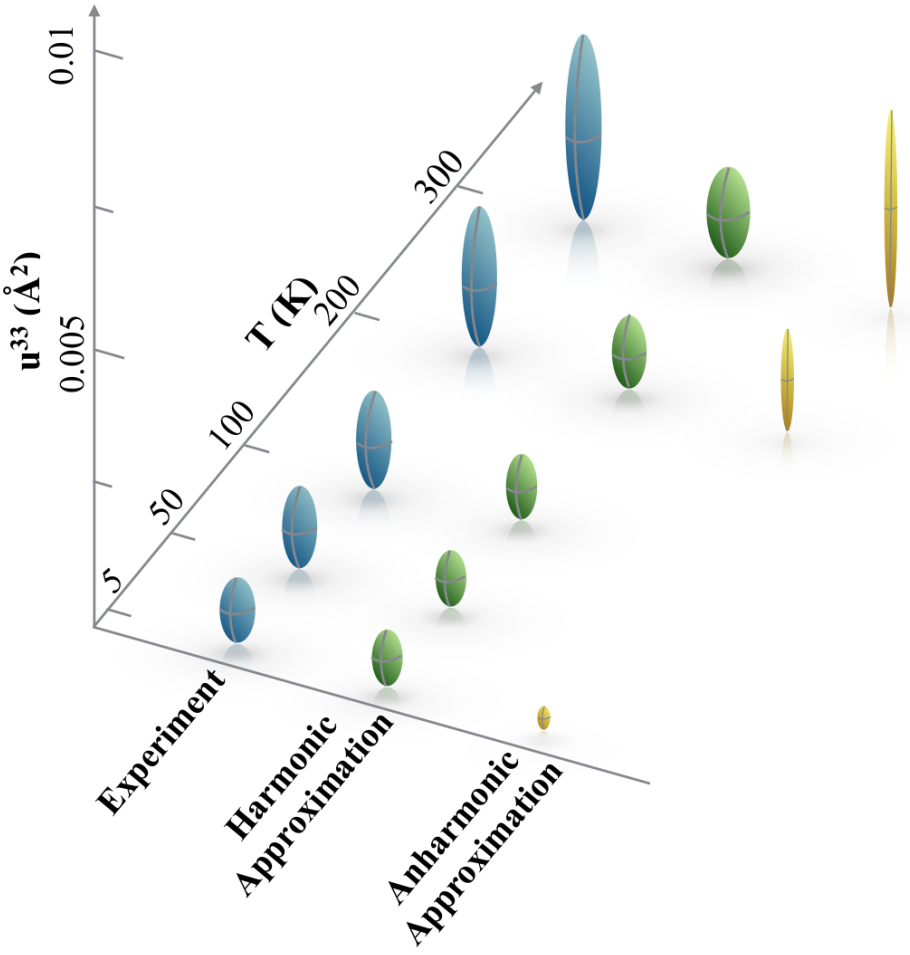

Figure 4.7: Atomic displacements at different temperatures can be represented by an ellipsoid, where the amplitude in the three dimensions are the ADPs, u_{11}, u_{22} and u_{33}. The blue ellipsoids represent the experimental atomic displacement. The green and yellow ellipsoids are obtained from the ADPs, extrapolated from the phonon calculations and *ab initio* MD simulations at different temperatures (using the optB88-vdW functional). The width of each ellipsoids represents the u_{11} and u_{22}, while the height represents the u_{33}.

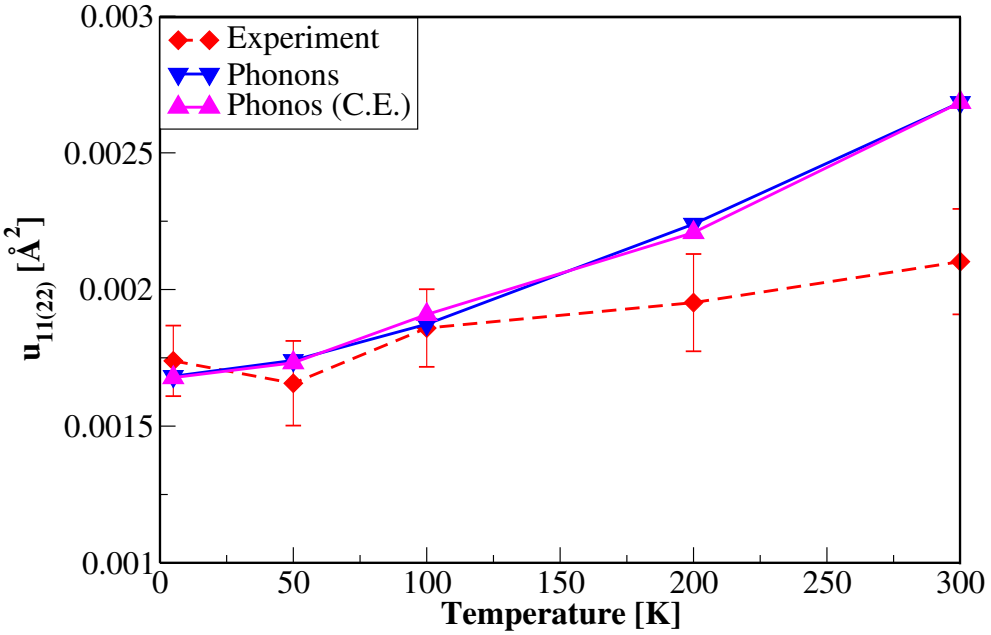

Figure 4.8: In–plane anisotropic displacement parameters (ADPs) of the carbon atoms, namely u_{11} and u_{22}, are reported as a function of temperature calculated with the optB88-vdW functional (solid lines). The computed ADPs are compared to the single crystal neutron diffraction experiment results (dashed line). Blue triangular data points refer to the standard ADPs calculation from the computed eigenvectors and frequencies within the harmonic approximation. Magenta triangles correspond to quasi–harmonic results, obtained by performing phonon calculations in unit cells with (temperature dependent) experimental lattice parameters.

Moving to the ADPs along the out–of–plane direction, u_{33}, reported in Fig. 4.10 it is possible to observe that the theoretical values are constantly and substantially underestimated by almost a factor of two with respect to experiment. In addition Fig. 4.7 highlights that the overall shape of the atomic displacement predicted by the simulations is substantially different from what found experimentally. There are several possible reasons for such disagreement, the first is related to the cell dimension. The ADPs have been calculated for the optimized unit cell structure at 0 K, however the experiment shows that the unit cell expands with temperature especially along the c direction. Thus in order to check this effect, the quasi–harmonic approximation has been used. For each temperature the cell dimensions have been set to the experimental values and the entire process leading to the ADPs has been repeated using the optB88-vdW functional. Results in Fig. 4.10 show that taking into account the thermal expansion of the cell has a very small effect on the ADPs and does not improve the prediction of u_{33}. It is also possible to argue that the disagreement between the theoretical and experimental u_{33} might come from an

inaccurate description of some vibrational modes from standard DFT, as discussed in 4.3.1.1. Fig. 4.9 shows the results of a test where the diffuse scattering has been calculated subtracting the contribution of the main out–of–plane modes of vibration, namely LA, ZA and ZO. One can observe that those modes are mainly responsible for the great part of the diffuse scattering in graphite and, according to the results in Table 4.2, are predicted within a few cm^{-1} of experiment. So this test shows that the poor description of the high frequency modes from DFT is not the main reason for the disagreement between the theoretical and experimental u_{33}.

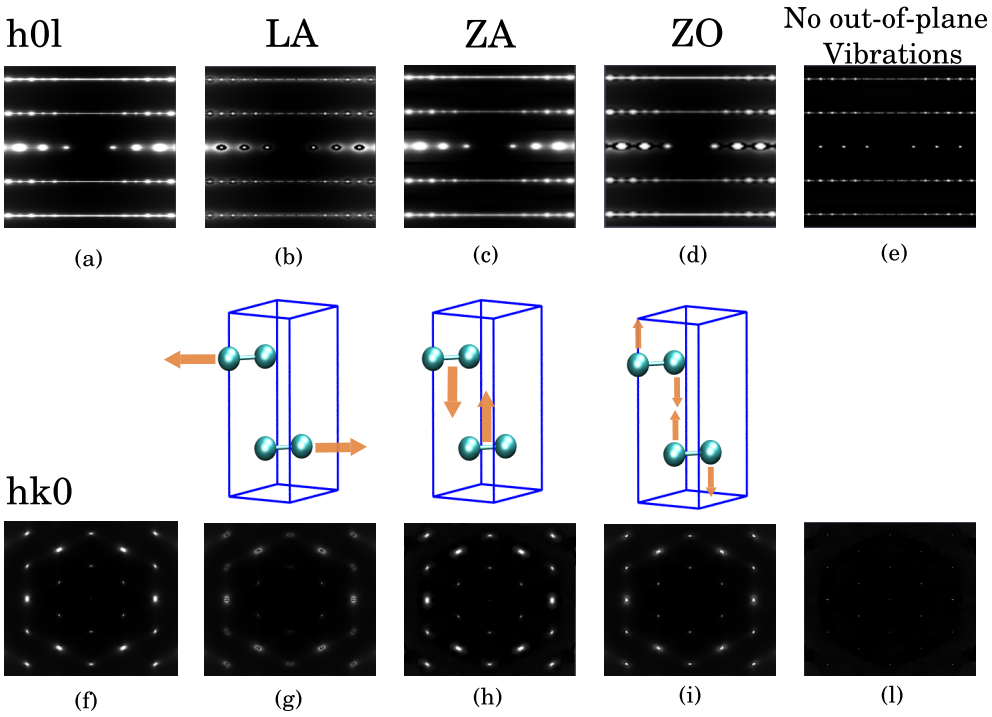

Figure 4.9: Single crystal graphite diffraction pattern at 300 K, calculated from Eq. 4.2, using the eigenvectors and frequencies from the phonon calculations using the optB88-vdW functional. (a) and (f) represent the total thermal diffuse scattering in the plane h0l and hk0 respectively. In (b) and (g) the diffuse scattering is calculated from Eq. 4.2, subtracting the contribution of the LA mode. In (c) and (h), and in (d) and (i) the contribution of the ZA and ZO modes are neglected, respectively. (e) and (l) represent the thermal diffuse scattering in the plane h0l and hk0 if the contributions of the all three modes are neglected.

As mentioned for the case of u_{11} and u_{22} the harmonic approximation can play an important role in the description of the dynamics of the atom, especially when vibrational modes become softer, as in the case of the out–of–plane vibrations. It has already been shown that the quasi–harmonic approximation is not enough to account properly for the displacement along the c direction. The comparison between

experiment and *ab initio* MD simulations highlights the extent of the anharmonicity in the carbon dynamics in graphite. The results of the *ab initio* MD in Fig. 4.10 clearly show that the inclusion of the anharmonicity improves the description of the u_{33} at high temperatures: the value at 300 K is in fact in perfect agreement with the experiment, and the prediction at 200 K is slightly improved with respect to the extrapolation from the phonons. At low temperature (50 K), however, the performance of *ab initio* MD is even worse than the extrapolation from the phonons. Here the inclusion of the quantum nuclear effects are as much important as the anharmonic effects, and PIMD simulations predict u_{33} finally in better agreement with experiment. The preliminary results of the PIMD simulations at 200 K reported in Fig. 4.10 suggest that QNEs might still be important at higher temperatures. Although the inclusion of the anharmonicity improves the prediction of the out–of–plane displacement with respect to the harmonic approximation, it is still underestimated compared to experiment. This disagreement can arise from the complete neglect of the QNE in ab initio MD simulations. However still a better convergence (in term of simulation length) needs to be reached in the case of the PIMD simulation at 200 K in order to safely state what the role of QNE is at such a temperature.

Finally we note that classical and quantum MD simulations have not been used to predict the in–plane ADPs at high temperatures because these values are numerically very small and they are highly affected by many computational parameters: cell dimension, potential energy cut-off and number of replicas in the case of PIMD. The calculation of the accurate value of the u_{11} and u_{22} requires expensive and long simulations, and this goes beyond the purpose of this work.

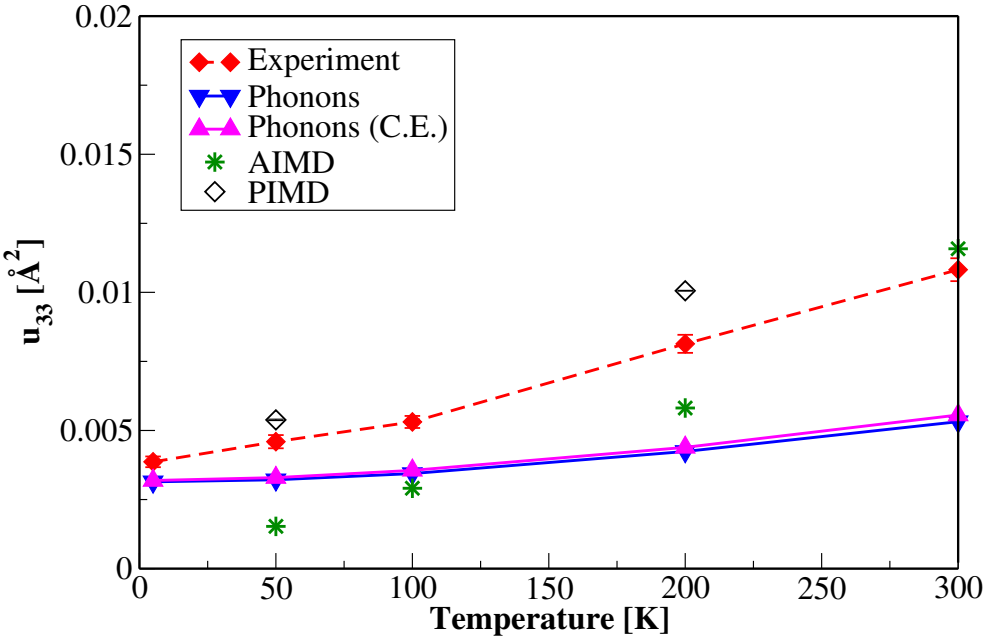

Figure 4.10: Anisotropic displacement parameters (ADPs) of the carbon out–of–plane ADP, u_{33}, as a function of temperature calculated with the optB88-vdW functional (solid lines). The computed ADPs are compared to the single crystal neutron diffraction results (red dashed line). Blue triangular data points refer to ADPs calculated from the computed eigenvectors and frequencies. Magenta triangles correspond to quasi–harmonic results, obtained by performing phonon calculations on the unit cell derived from experimental data. Green stars are the results of *ab initio* MD simulations and black squares are the results of PIMD simulations.

4.4 Discussion and conclusion

The results reported here have shown that the complete picture of the carbon dynamics in graphite is achievable if a combination of static and dynamic DFT is used. The in–plane ADPs at low temperature can be safely extracted from phonon eigenvectors and frequencies calculated within the harmonic approximation. This approximation, however, fails at high temperature and for the description of the out-of–plane displacement of carbon atoms in graphite. In the case of the out–of–plane ADPs, the major contributions come from the transversal acoustic modes of vibration, which are soft modes and highly anharmonic. This is the reason why extrapolation of u_{33} from the phonon calculations disagrees with the experiment at all temperatures. *Ab initio* MD performs better than the harmonic approximation in describing u_{33} at higher temperatures but it is worse at low temperature. *Ab initio* MD does not rely on the harmonic approximation, but it does rely on a clas-

sical description of the nuclei. Thus the improvement coming from the inclusion of anharmonicity is counterbalanced by the classical treatment of the nuclei, which results in an underestimation of u_{33}. In fact in this range the extrapolation of the ADPs from phonon calculations yields better agreement with experiment than *ab initio* MD because the first order QNE, that is the zero point energy, is taken into account in the last term of Eq. 1.

The out–of–plane displacement of graphite carbon atoms can be split in to two regimes, by applying the Einstein solid model [180, 181]. In this case a solid is assumed to be composed by independent harmonic oscillators, so the mean squared displacement of a single particle can be assumed to be quantum and harmonic at low temperature and classical and harmonic at high temperature. The harmonic regime can be identified by the linear trend of the ADPs at high temperature and, in the case of the harmonic oscillator, the linear extrapolation yields to a zero mean square displacement at 0 K. Any deviation from such a linear extrapolation highlights anharmonicity in the atomic dynamics in the solid. In the case of graphite, the linear extrapolation of the experimental u_{33} at 100, 200 and 300 K does not yield a zero displacement at 0 K. This confirms that above 50 K the carbon dynamics are anharmonic and the harmonic approximation is no longer applicable. The u_{33} at temperatures below 50 K, on the other hand, belongs to the quantum regime, confirming the results from PIMD simulations.

This study shows that the carbon displacement in graphite is highly anisotropic and its accurate description is not straightforward. In fact although the in–plane dynamics can be safely treated within the harmonic approximation for temperature below 50 K, the out–of–plane dynamics needs more careful treatments. These results also highlight that the general picture of the carbon atom as a classical nucleus, breaks down at temperatures lower than 300 K. This can be of high importance for future studies of processes at low temperature where carbon dynamics needs to be taken into account, like studies of molecular diffusion on carbon based materials and the investigation of electric and thermal transport properties.

Further studies about the carbon dynamics in graphite are currently ongoing. Specifically, additional experiments have been performed by using the VESUVIO spectrometer at ISIS which are in the process of being analysed in detail. The VESUVIO spectrometer provides direct access to the momentum distribution of the individual atoms without the need of a structure refinement procedure, as opposed to the measurement of the ADPs from the diffraction pattern. Knowing the momentum distribution of the individual atoms allows to obtain their mean kinetic energy

and therefore a straightforward measurement of the ZPE of the atoms. The comparison between experimental and predicted values will then be used to benchmark even further the computational procedures discussed so far. More details about the measurement of the momentum distribution and some preliminary results are reported in Appendix B.

Chapter 5

Beyond graphite and *h*-BN: The role of van der Waals interactions in other layered materials and in their hydrogen uptake

In the previous chapters it was discussed how the accurate description and understanding of vdW dispersion forces in chemical and physical systems is one of the most active areas of research in contemporary computational science [35]. Despite the large number of recent studies examining vdW-dominated systems [182, 183, 37, 184, 38, 39], there are still major gaps in our understanding, precisely when it comes to the role of the vdW forces in processes like adsorption on surfaces.

Particular attention has been devoted during the years to the study of physical adsorption, or physisorption, of small molecules on different kinds of materials [73, 185, 186, 187]. The physisorption of gas molecules on surfaces does not involve any breaking and formation of chemical bonding between the adsorbate and the substrate, but relies on very weak interactions due to vdW forces [187]. It is exactly this feature that makes the physisorption process a very appealing answer to problems like gas-storage, because it can promise fast load–unload kinetics [13, 188].

In addition layered materials are also very promising as part of the solution for gas–storage problems, as discussed in Chapter 1 [189, 190]. The characteristic anisotropy of these materials enables them to expand, creating the possibility of adsorption on the surface and absorption between the layers of small molecules like hydrogen. Despite the large number of layered materials, mainly graphite and

its derivatives have driven attention so far for their interaction with hydrogen. A remarkable number of theoretical works has been reported in the literature where mainly the adsorption of the hydrogen molecule on graphene [191, 192, 193, 194, 195, 196, 197] or on graphite nanofibers [198, 199, 196] has been investigated. Most of them report studies using Møller-Plesset second order perturbation theory (MP2) to study the physisorption of hydrogen on polycyclicaromatic hydrocarbons, like coronene, usually taken as a model for graphite in MP2 calculations in order to reduce the computational cost [196, 197, 195]. Only a few works have taken into proper account vdW forces for the study of the periodic system [193, 194]. Very few theoretical and experimental studies are reported about the interaction of hydrogen and the remaining layered materials, first of all the graphite inorganic analog, *h*-BN [200] and the class of transition metals dichalcogenides [201, 202, 203, 204].

Recent studies reported by Björkman *et al.* show that most layered materials are characterized by very similar interlayer binding energies, despite the different atomic composition and geometry [38, 39, 40]. This similarity has been explained as a balance between repulsive and attractive interactions between the layers. Thus it is interesting to test if the same behaviour is maintained also in the case of another process dominated by vdW forces, which is hydrogen adsorption on layered materials.

As discussed in the previous chapters, the recent availability of new functionals within DFT able to properly treat the long range interactions, expand the applicability of DFT to systems and processes where weak interactions are important, like physisorption. Here different functionals which properly treat the long–range interactions have been used in first instance to calculate and compare the interlayer properties of some transition metal dichalcogenides, namely molybdenum disulfide (MoS_2), molybdenum diselenide ($MoSe_2$), molybdenum ditelluride ($MoTe_2$), tungsten disulfide (WS_2) and titanium diselenide ($TiSe_2$), in addition to the interlayer properties of graphite and *h*-BN already discussed in Chapter 3. Then, the same functionals have been used to investigate hydrogen adsorption on the surface of these transition metals dichalcogenides and on the surface of graphite and *h*-BN. The substrates in this study have been selected in order to look at the effects of several different variables on hydrogen adsorption. The first is the class of materials, that is graphite–like or transition metal dichalcogenides. The second is the role of the different atomic composition of each material. Within graphite–like substrates, graphite and *h*-BN have been selected. These materials have very similar structures and intra– and interlayer energies, but different atomic compositions that can affect

the strength of the hydrogen adsorption. For the transition metal dichalcogenides, for a given transition metal (Mo in this case) the effect of the different chalcogen (X=S, Se, Te), and for a given chalcogen (X=S) the role of the transition metal (M=Mo, W) on the hydrogen adsorption has been investigated. Finally the effect of different structures in the case of the MoX_2 and $TiSe_2$ has also been explored.

In the following sections details of the computational method are reported. Results of the interlayer binding energies, cell parameters and adsorption energies of hydrogen on different surfaces are shown in section 5.2. This chapter is then concluded with a discussion in section 5.3.

5.1 Methods

The DFT calculations have been performed with the periodic plane–wave basis set code VASP 5.3 and five different exchange-correlation functionals, namely, optB88-vdW, optPBE-vdW, vdW-DF2, DFT-D2 and TS-PBE. The calculations have been carried out self–consistently using an implementation of the vdW-DF method in VASP with the scheme of Román–Pérez and Soler, and the implementation of the Tkatchenko-Scheffler correction by Bučko *et al.* [205]. PBE–based PAW potentials have been used and all results reported have been obtained with standard potentials using a 600 eV plane–wave cut–off. For each structure a Monkhorst-Pack k-point grid of $8 \times 8 \times 2$ per unit cell has been used.

Molybdenum transition metal dichalcogenides, are layered materials where each layer is composed of a transition metal covalently bonded to two chalcogen atoms, forming a *sandwich* structure as shown in Fig. 5.1. The class of the molybdenum dichalcogenides and WS_2 are characterized by the same structure and the layers follow the AB stacking, as the case of the graphite. The $TiSe_2$ has a slightly different structure which is characterized by the AA stacking of the layers, as the case of *h*-BN. The bulk properties of each material have been optimized using a multiple step procedure. For the MoS_2, $MoSe_2$, $MoTe_2$ and WS_2 a six atom hexagonal unit cell has been used, and for $TiSe_2$ a three atom unit cell has been used, as shown in Fig. 5.1. First a full relaxation of the ions, cell shape and volume has been performed. The values obtained for the in–plane lattice constant (a) and height of the cell (c) have been used as a first guess for the subsequent step. The out–of–plane lattice constant, c, has then been optimized by changing systematically the height of the cell in a range of ± 0.5 Å from the initial guess, while the in–plane lattice constant a was kept fixed and the ions were relaxed. The value of c corresponding to the minimum

energy has been used to optimize the a lattice constant. In this case c has been kept constant and a has been systematically changed in a range of ± 0.5 Å from the initial guess. The procedure was iterated until a common minimum was found. Generally one iteration was sufficient to find the two minima.

For each material the interlayer binding energy (E_{inter}) was calculated by subtracting twice the energy of an isolated monolayer (E_{lay}) from the energy of the bulk (E_{bulk}) and dividing this value by the area of the cell (A) to obtain it in meV/Å^2.

$$E_{\text{inter}} = \frac{E_{\text{bulk}} - 2E_{\text{lay}}}{A}. \tag{5.1}$$

The interlayer binding energy and the c for each material has been obtained by interpolating the data using a Morse potential.

The cell parameters obtained by the unit cell optimization were used to optimize a slab of 3 layers transition metal dichalcogenides as showed in Fig. 5.1, that was then used as substrate for the hydrogen adsorption calculations. In this case the 3×3 supercells containing 3 layers of each transition metal dichalcogenides were used. Also slabs of 4 layers graphite and h-BN were optimized using a $3 \times 3 \times 2$ supercell. In all cases vacuum of ~ 15 Å has been added to avoid any interaction with the periodic image. All the structures were optimized by fully relaxing all the ions.

The optimized slab was used as a substrate to calculate the adsorption energy of a single hydrogen molecule on the surface of each material. The optB88-vdW functional has been used to explore any preferential position or orientation for the hydrogen molecule adsorbed on the layered materials. Different starting configurations of the hydrogen molecule on the layered materials have been chosen on the basis of pure symmetry arguments and are reported in Fig. 5.2. For all the configurations the H_2 has been set initially at about 3 Å and relaxed as well as the first layer of the substrate, while the remaining layers were kept fixed. For each configuration the adsorption energy (E_{Ads}) has been calculated by subtracting from the total energy of the system ($E_{\text{H}_2/\text{Sub}}$) the energy of an isolated hydrogen molecule (E_{H_2}) and that of the bare substrate (E_{Sub}):

$$E_{\text{Ads}} = E_{\text{H}_2/\text{Sub}} - E_{\text{H}_2} - E_{\text{Sub}} \tag{5.2}$$

All the other functionals, namely the optPBE-vdW, vdW-DF2, DFT-D2 and the TS-PBE, were used to calculate the adsorption energies of the hydrogen molecule just on the hollow site of the different materials. Note that the hydrogen adsorption

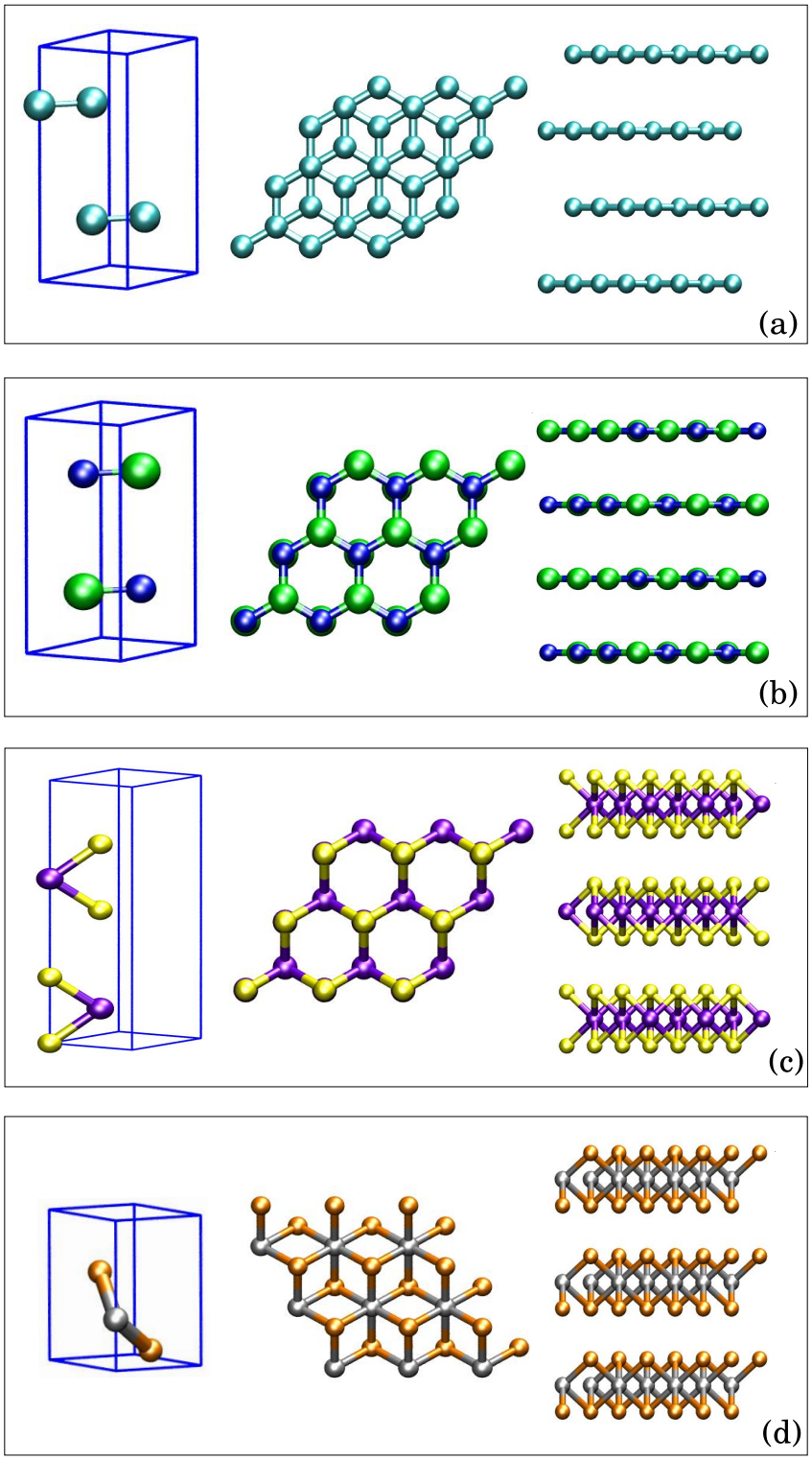

Figure 5.1: In (a) and (b) the representative unit cells, top and front views of the bulk graphite and h-BN are shown. In (c) the representative unit cell, top and front view of molybdenum dichalcogenides (MoX_2) and of the tungsten disulfide (WS_2) are reported, where transition metals are in purple and the chalcogens are in yellow. The unit cell, top and front view of titanium diselenide ($TiSe_2$) are reported in (d), where the titanium atoms are represented in silver and selenium in orange.

on WS_2 was not calculated using the DFT-D2 and TS-PBE functional, because of the lack of C_6 and vdW radius for the tungsten in the VASP code.

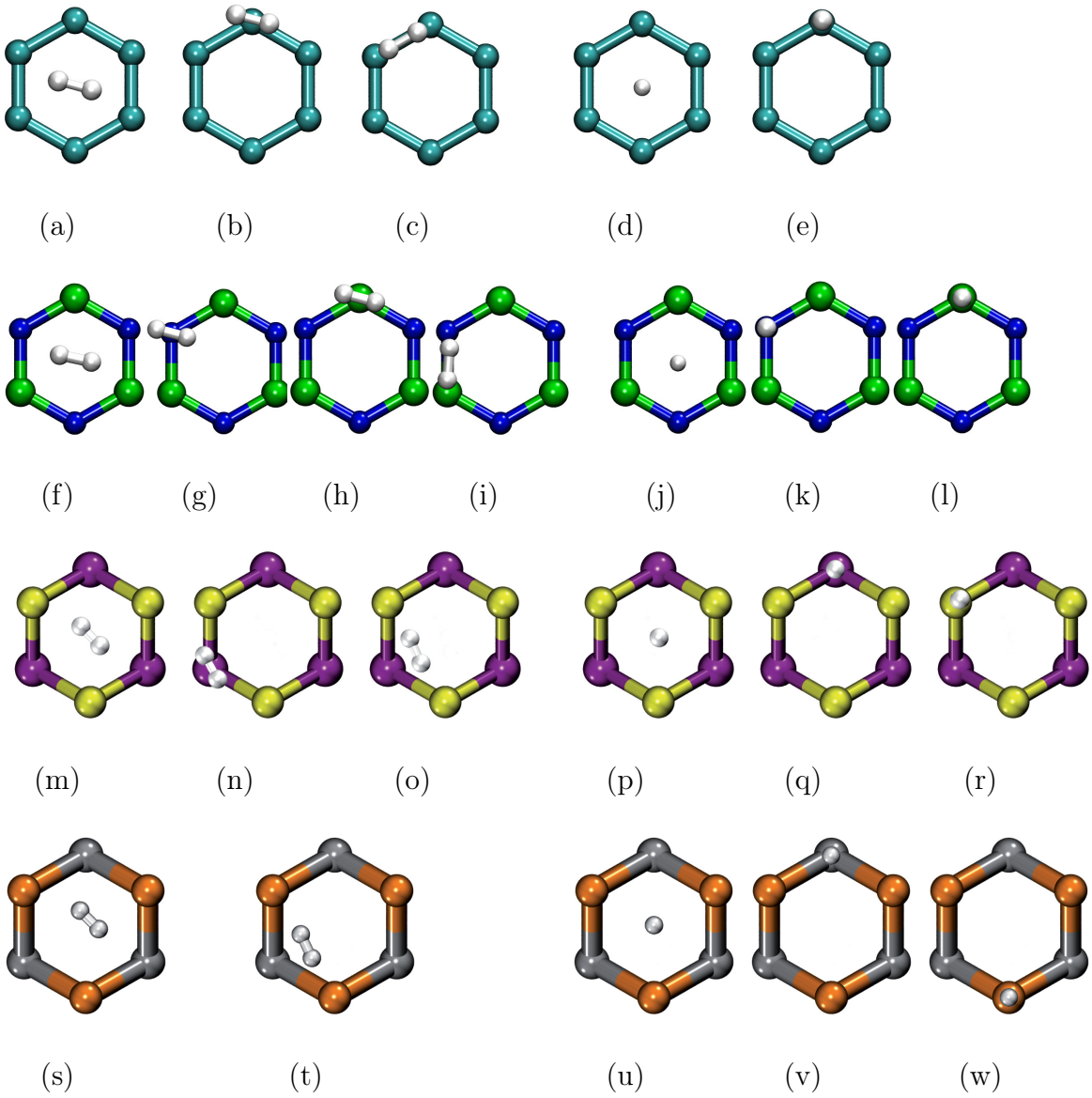

Figure 5.2: Initial configurations of hydrogen on the surface of various layered materials. In the first row, configurations of the hydrogen molecule on the graphite surface. (a), (b) and (c) represent the hydrogen molecule parallel to the surface on the hollow, top and bridge site of graphite. (d) and (e) represent the molecule on the hollow and top sites respectively, but perpendicularly oriented to the surface. The same configurations, from (f) to (l) have been analysed for *h*-BN, considering the additional top site due to the presence of the B and N atoms on the surface. In the third row different configurations of the hydrogen molecule adsorbed on the molybdenum dichalcogenides (MoX_2) and tungsten disulfide (WS_2) are reported. In (o), (p) and (q) the hydrogen molecule is parallel on the surface while in (r), (s) and (t) the gas molecule is perpendicular. In the last row the configurations of the hydrogen molecule oriented parallel and perpendicular on the surface of the $TiSe_2$ are shown.

5.2 Results

5.2.1 Interlayer binding energies

The interlayer binding energies and the geometrical properties of the selected transition metal dichalcogenides (MoS_2, $MoSe_2$, $MoTe_2$, WS_2 and $TiSe_2$) have been calculated using the optB88-vdW functional. Fig. 5.3 reports the interlayer binding energy as a function of the out–of–plane lattice constant (c) for the transition metal dichalcogneides analysed here. From the graph it can be seen that the interlayer binding energies are all very similar and they lie in the range of -17 to -25 meV/Å^2.

Looking at the results in more detail, one can observe that the choice of the transition metal, as in the case of the MoS_2 and WS_2, does not significantly affect the structure or the interlayer binding energy. Indeed the binding curves in Fig. 5.3 for these two transition metal dichalcogenides basically overlap. In addition Table 5.1 shows that also the calculated in–plane lattice constant (a) does not change much moving from the molybdenum to the tungsten. This similarity is confirmed also by the experimental values for the lattice constants and by the random phase approximation (RPA) calculations of the interlayer binding energies performed by Björkman *et al.* [39].

Let us look at the role of the chalcogen atom in the case of the molybdenum dichalcogenides. Fig. 5.3 shows that although the lattice constant c expands going from the sulfur to the tellurium, the interlayer binding energy does not change dramatically, and it lies in the range from -25 to -28 meV/Å^2. From Table 5.1 one can observe that a also expands moving from MoS_2 to $MoTe_2$ and this trend is in agreement with the experimental lattice constants. It seems that the increasing polarizability of the chalcogen atoms is balanced by the expansion of the unit cells, that turns into comparable interlayer binding energies. Furthermore the insert in Fig. 5.3 summarises and highlights that a very similar physics governs the interlayer interactions in these transition metal dichalcogenides. This graph actually shows that the binding curves normalised by the minimum interlayer binding energy and the corresponding optimized lattice constant for the MoX_2 and WS_2 perfectly overlap. The normalised curve for the $TiSe_2$ is slightly broader with respect to the curves for MoX_2 and WS_2. It must be noted, however, that $TiSe_2$ is characterized by a a different structure compared to the other transition metal dichalcogenides, in addition to the different atomic composition. Despite the slightly different structure and atomic composition, it still shows a similar interlayer binding energy with re-

spect to MoX_2 and WS_2. This result is confirmed also by experiment and the RPA calculations as it is reported in Table 5.1 and exactly the same trend has also been reported in the following Ref. [38, 39, 40].

The interlayer binding energy of graphite and *h*-BN obtained from optB88-vdW has been discussed in detail in Chapter 3. Table 5.1 reports the lattice constants and the interlayer binding energy for these layered materials as well as the comparison with the experimental lattice constants and the RPA interlayer binding energies. Although the lattice constants predicted by optB88-vdW are in good agreement with experiment, the interlayer binding energies are slightly overestimated compared to the RPA calculations. This trend has already been addressed and discussed in Chapter 3. However from a pure qualitative analysis of the results, Table 5.1 highlights that even though graphite and *h*-BN are characterized by a complete different structure compared to the transition metal dichalcogenides, which is reflected in the shape of the normalised interlayer binding curve, the interlayer binding energies are still very similar. These results are in full agreement with those of Björkman *et al.* [38].

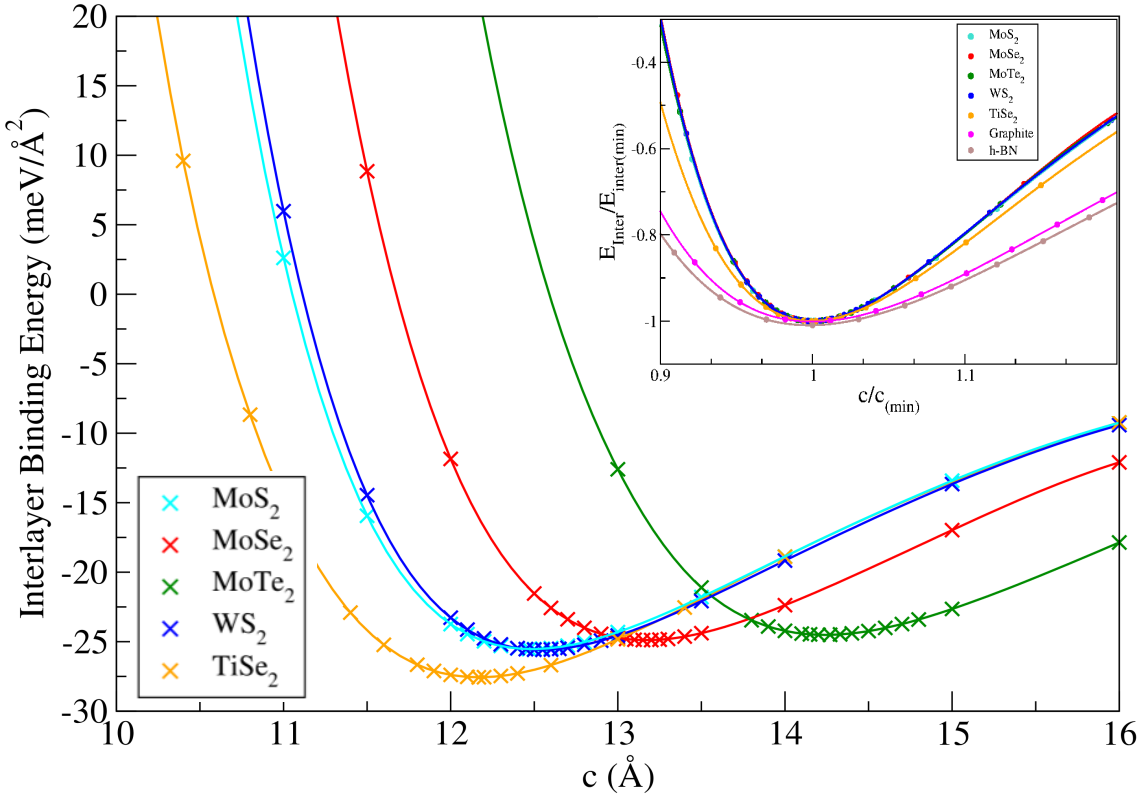

Figure 5.3: Interlayer binding energy as a function of the lattice constant c for the transition metal dichalcogenides. $TiSe_2$ has AA stacking and its unit cell can be defined by a single layer, the other transition metal dichalcogenides are characterized by AB stacking and their unit cell is composed of two layers. In order to make a reasonable comparison of the structural properties of the materials, the $TiSe_2$ lattice constant has been doubled. The insert shows the same curves normalised for the minimum interlayer binding energy, $E_{inter(min)}$ and the corresponding optimal lattice constant, c_{min}.

5.2.2 Adsorption energy of hydrogen on layered materials

The adsorption of molecular hydrogen on graphite, h-BN, MoS_2, $MoSe_2$, $MoTe_2$, WS_2 and $TiSe_2$ has been examined using the optB88-vdW functional. Different starting positions and orientations of hydrogen on top of the layered materials have been explored, as illustrated in Fig. 5.2. However the optimization process does not lead to major changes in the initial configurations of the hydrogen molecule.

The results summarised in Table 5.2 show that the hydrogen adsorption energy does not change dramatically on the different surfaces, spanning from a maximum of -84 meV/H_2 in the case of graphite to a minimum of -57 meV/H_2 in the case of $MoTe_2$. By looking first to the simpler layered materials, that is graphite and h-BN,

Table 5.1: Lattice constants, cell heights and interlayer binding energies for the layered materials predicted using the optB88-vdW functional. The interlayer binding energies and the geometrical parameters are compared respectively to RPA calculations and experimental values reported in the Ref.[39].

Material	a (Å)	c (Å)	E_{inter} (meV/Å^2)	a^{expt} (Å)	c^{exp} (Å)	$E_{inter}{}^{RPA}$ (meV/Å^2)
Graphite	2.468	6.712	26	2.456	6.696	18
h-BN	2.509	6.594	25	2.510	6.690	14
MoS_2	3.193	12.487	25	3.162	12.302	21
$MoSe_2$	3.329	13.170	25	3.289	12.927	20
$MoTe_2$	3.578	14.242	28	3.442	19.973	21
WS_2	3.191	12.539	26	3.153	12.323	22
$TiSe_2$	3.539	6.084	28	3.536	6.004	17

one can observe that they physisorb hydrogen in a very similar manner. On both surfaces a strong preferential orientation for the gas molecule is not highlighted, since the adsorption energies differ no more than ~ 7 meV from one configuration to another. However both materials show a slight preference to physisorb hydrogen on the hollow site, parallel to the surface. Although the adsorption energies and the distances from the surface are similar, hydrogen is more strongly adsorbed by graphite, with a value of -84 meV/H_2. Although this energy is somehow larger than the experimental value of -52 meV/H_2 found by Mattera and coworkers [206], this trend is in line with previous theoretical works where hydrogen physiorption on nanostructured graphite and BN are compared. Wang *et al.* [207], Zhou *et al.* [208] and Krishnan *et al.* [209] all show that the physisorption energy of hydrogen is larger on nanostructured graphite than on nanostructured BN.

Let us turn to the transition metal dichalcogenides. Also in this case a preferential position or orientation is not heavily highlighted and the adsorption energies for the different configurations differ by a few meV for each material. Table 5.2 shows also that although hydrogen adsorption energies on the different transition metal dichalcogneides are very similar, it is possible to define a trend that is almost in line with the trend of interlayer binding energies calculated with the optB88-vdW functional. The different transition metal, in the case of the MoS_2 and WS_2, does not affect either the adsorption energy or the distances of the centre of mass of the hydrogen molecule from the surface, which are respectively ~ -64 meV/H_2 and ~ 3.1 Å. The choice of the chalcogen atom has a greater impact on the adsorption energy. That is because the chalcogen atoms are at the interface and directly interact with the hydrogen molecule. Moving from MoS_2 to $MoTe_2$ it can be seen that the hydrogen–substrate distance increases from ~ 3.1 to ~ 3.4 Å. The increasing distance correlates with a decrease of the adsorption energy from ~ -64 meV/H_2 in the case of the MoS_2 to ~ -56 meV/H_2 in the case of the $MoTe_2$. The hydrogen adsorption energy seems to be not affected by the different structure of the $TiSe_2$, where the energy and distance are in line with the other transition metal dichalcogenides.

Other functionals have also been used to calculate the adsorption energy of the hydrogen on the hollow site of the different layered materials for both the parallel and perpendicular orientations of the gas molecule with respect to the surface. The results obtained with the optPBE-vdW, vdW-DF2, DFT-D2 and TS-PBE functionals are summarised in Table 5.3. All functionals predict the distances of the hydrogen centre of mass from the surface in good agreement with each other, within about

0.1 Å for each system. On the other hand more evident fluctuations can be identified for the adsorption energies. Among the vdW-DFs, the optPBE-vdW predicts the highest hydrogen adsorption energies, ranging from ~ -100 mev/H_2 on graphite to ~ -72 mev/H_2 on $MoTe_2$. vdW-DF2 predicts the lowest adsorption energies, ranging from ~ -70 meV/H_2 in the case of graphite to ~ -40 mev/H_2 for $MoTe_2$. The optB88-vdW, DFT-D2 and TS-PBE are within these limits as can be observed from Table 5.3. A closer look at the results reveals also that, although the adsorption energies predicted by the different functionals are different, their trend is always repeated. Since a comprehensive experimental study of the adsorption energies of hydrogen on the layered materials is not reported in the literature, it is difficult to state about the accuracy of the functionals tested here. However the qualitative analysis seems to highlight that all the functionals predict the highest adsorption energies for graphite and h-BN among the materials studied. The adsorption energy on the transition metal dichalcogenides seems to be overall homogeneous, although it is slightly sensitive to the different chalcogen atoms. All the functionals predict a reduction of the adsorption moving from the sulfur to the tellurium.

5.3 Discussion and Conclusion

Similar adsorption energies of the hydrogen molecule on the surface of different layered materials can be explained as a balance of attractive and repulsive interactions. This balance has already been addressed as the reason for similar interlayer binding energy of the layered materials [38, 39, 40] as has also been shown in Chapter 3. Fig. 5.4 shows the decomposition of the adsorption energies into the repulsive and attractive contributions, similar to the decomposition of the interlayer binding energies reported in Chapter 3. Local and non–local correlation energies are a measure of the attractive interactions and the exchange energy, added to all other components of the Kohn-Sham energy can express the repulsive interactions. From Fig. 5.4 it can be seen that for all the layered materials the local correlation contributes marginally to the total adsorption and that the attractive energy is almost purely due to the long–range interactions. The non–local correlation energy and the repulsive energy have larger impact on the total adsorption and they vary among the layered materials. For all systems these variations cancel each other resulting in overall similar adsorption energies and $TiSe_2$ is a clear example of such a balance. On the other hand it can also be observed that the higher adsorption energies of the hydrogen on graphite and h-BN seem to be mostly due to their slightly higher

Table 5.2: Adsorption energies and hydrogen–substrate distances for hydrogen adsorbed on a selection of layered materials calculated with the optB88-vdW functional. All the configurations are named according to Fig. 5.2. M and X refers to the transition metal and chalcogen respectively. The hydrogen–substrate distances refer to the distance of the molecule centre of mass from the substrate surface. All the adsorption energies are expressed in meV/H_2 and the distances in Å.

Configuration	**Graphite**		**h-BN**		**MoS_2**		**$MoSe_2$**		**$MoTe_2$**		**WS_2**		**$TiSe_2$**	
	E_{Ads}	d	E_{Ads}	d	E_{Ads}	d	E_{Ads}	d	E_{Ads}	d	E_{Ads}	d	E_{Ads}	d
Parallel														
Hollow	-84	3.00	-78	3.00	-64	3.10	-60	3.21	-56	3.42	-64	3.10	-64	3.06
Bridge X-X	-78	3.15	-72	3.03	-64	3.13	-61	3.24	-57	3.49	-64	3.13	-61	3.09
Top M	-77	3.14	B: -75	3.01	-67	3.03	-64	3.13	-60	3.30	-67	3.01		
			N: -68	3.1										
Perpendicular														
Hollow	-79	3.09	-74	3.05	-63	3.19	-60	3.28	-56	3.47	-64	3.18	-64	3.18
Top M	-77	3.16	B: -71	3.05	-66	3.14	-63	3.21	-59	3.42	-66	3.17	-64	3.10
Top X			N: -74	3.16	-57	3.42	-54	3.55	-50	3.80	-57	3.45	-51	3.52

Table 5.3: Adsorption energies and hydrogen–substrate distances of hydrogen adsorbed on the layered materials calculated with different functionals. All the adsorption energies are expressed in meV/H_2 and the distances are in Å. Hydrogen adsorption on WS_2 was not calculated using the DFT-D2 and PBE-TS schemes, because of the lack of a C_6 coefficient and vdW radius for tungsten in the VASP code.

Substrate	**optB88-vdW**		**optPBE-vdW**		**vdW-DF2**		**DFT-D2**		**PBE-TS**	
	E_{Ads}	d	E_{Ads}	d	E_{Ads}	d	E_{Ads}	d	E_{Ads}	d
Graphite	-84	3.00	-104	3.08	-74	3.01	-64	2.89	-82	3.00
	-79	3.09	-98	3.18	-67	3.06	-67	2.91	-75	3.15
***h*-BN**	-78	3.00	-101	3.11	-67	3.06	-65	2.86	-80	3.00
	-74	3.05	-97	3.18	-65	3.17	-71	2.90	-75	3.17
MoS_2	-64	3.10	-84	3.16	-58	3.06	-41	3.21	-58	3.02
	-63	3.19	-81	3.24	-57	3.15	-45	3.21	-56	3.16
$MoSe_2$	-60	3.21	-79	3.24	-53	3.22	-44	3.21	-52	3.13
	-60	3.28	-78	3.33	-54	3.27	-49	3.21	-53	3.26
$MoTe_2$	-56	3.42	-73	3.35	-40	3.30	-44	3.21	-48	3.32
	-56	3.47	-72	3.42	-42	3.25	-51	3.21	-50	3.42
WS_2	-64	3.10	-84	3.13	-57	3.07				
	-64	3.17	-82	3.21	-57	3.14				
$TiSe_2$	-64	3.06	-83	3.10	-57	3.00	-46	3.21	-59	3.07
	-64	3.18	-81	3.19	-56	3.07	-51	3.21	-56	3.02

non–local correlation energies.

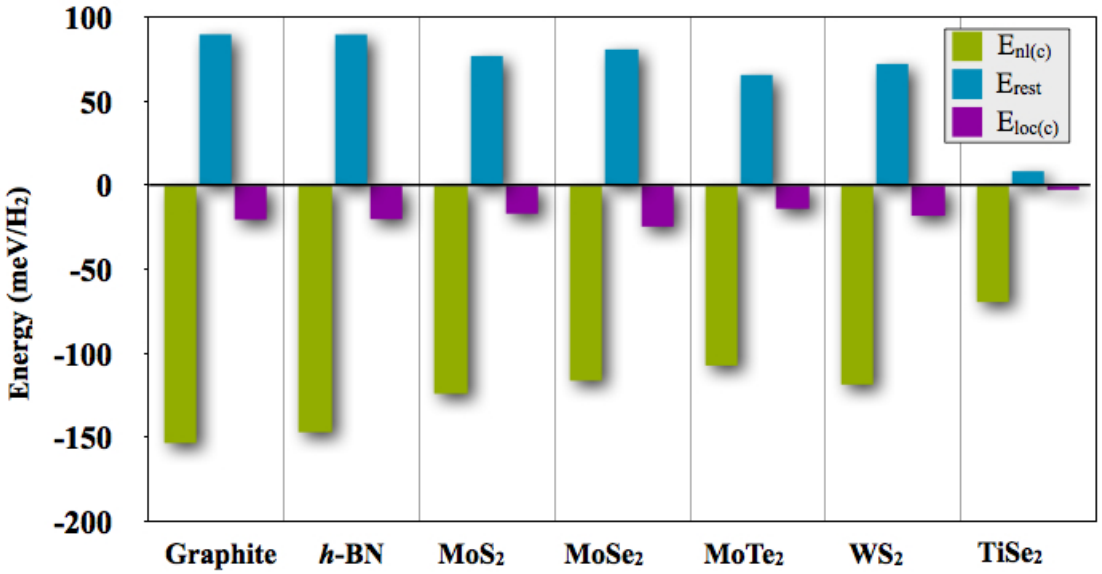

Figure 5.4: Decomposition of the adsorption energy of the hydrogen on the surface of the layered materials obtained with the optB88-vdW functional. The negative values are due to the correlation energy, specifically to the non–local (green bars) and local (purple bars). The positive values refer to the exchange and the remaining Kohn-Sham energy (blue bars).

Although the energy decomposition explains the general reason for the similar hydrogen adsorption energy, it does not clarify however the subtle trend for the different layered materials. Essentially, it does not explain why the hydrogen adsorption energy on materials characterized by higher polarizabilities is similar or even lower than the adsorption energy on less polarizable materials.

In order to have a clearer idea of the relation between the different polarizabilities of the substrate on the hydrogen adsorption energy, results of the PBE-TS functional have been analysed in more detail. Indeed the method developed by Tkatchenko and Scheffler aims to calculate the dispersion energy using reference atomic polarizabilities and C_6 coefficients of the free atoms. The chemical environment of the specific atom is also taken into account by looking at the effective atomic volume, which is used to obtain the environment specific dispersion coefficient [68]. Let us look first at the PBE-TS results for the hydrogen adsorbed on graphite and h-BN reported in the Table 5.4. On both materials the adsorption energy of the hydrogen perpendicularly oriented on the top site is about -69 meV/H_2 and the distance of the hydrogen centre of mass from the surface is ~ 3.16 Å. These results are due to the very similar polarizability (~ 6.91 a.u./Å^3 for graphite and ~ 6.29 a.u./Å^3 for

h-BN) and structure of the two materials, as shown in the first two columns of Table 5.4. More interesting is the case of the transition metal dichalcogenides. Looking at Table 5.4 one can observe that for MoX_2 the polarizability of the material slightly increases moving from sulfur to tellurium. The increasing polarizability is balanced at the same time by both the in– and out–of plane expansions of the material. A similar effect is resembled in the case of the hydrogen adsorption: the increasing polarizability of the chalcogen atoms on the surface is balanced by a larger distance of the hydrogen centre of mass from the surface. This results in a slight lowering, of about 7 meV/H_2, of the hydrogen adsorption energy moving from MoS_2 to $MoTe_2$. Looking closer at the atomic volumes, particularly at the vdW radii of the chalcogen atoms, it is possible to see that although they increase moving from the sulfur to the tellurium, the overlap between the hydrogen and the chalcogen atomic volumes is kept constant.

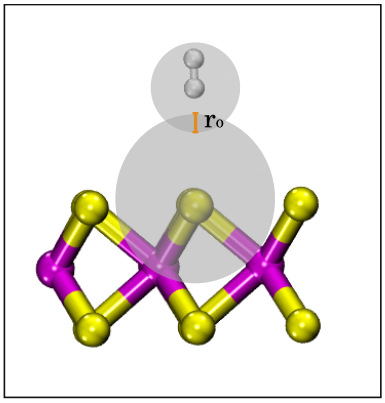

Figure 5.5: Schematic description of the overlap of the hydrogen and surface atom volume overlap. The grey circles represent the section of the atomic volumes, and the darker grey area is their overlap. r_o refers to the maximum height of the overlap section.

Table 5.4 reports the vdW radii of the free atoms (R_0) and of the radii optimised for the chemical environment (R_0(optim.)), in addition to the overlap of the vdW radii for the free and optimised atoms, namely r_o and r_o(optim.). Fig. 5.5 reproduces a simplified description of the overlap of the atomic vdW radii. The values of r_o are similar for all the transition metal dichalcogenides, especially when the atomic volumes, and the the vdW radii, are adjusted for the chemical environment. In this case r_o(optim.) lies in a very narrow range, from 0.42 to 0.47 Å for all the transition metal dichalcognides studied. It is also surprising that analogous values for r_o(optim.) have been found for graphite and h-BN, 0.41 and 0.51 Å respectively.

Table 5.4: Summary of the results of the PBE-TS calculations. The first column shows the ratio between the in–plane (a) and out–of–plane (c) lattice constants of the layered materials. Then the C_6 coefficients normalized by the unit cell volume are reported as a measure of the polarizability of the materials. The forth column shows the adsorption energies expressed in meV/H_2 for the hydrogen perpendicularly oriented on the top site. The following two columns report the distance of the hydrogen centre of mass from the surface and the distance between the lowest hydrogen and the surface,respectively. Then the van der Waals radii before and after the TS optimization are reported in the following two columns (R_0 and R_0(optim)). The last two sets of data refer to the height of the section of the overlap of the atomic volumes before and after the TS optimization (r_o and r_o (optim.)). All the distances and radii are expressed in Å.

System	c/a	C_6/Vol	E_{Ads}	**d X-H**	**d X-H1**	R_0	R_0**(optim.)**	r_o	r_o **(optim.)**
Graphite	2.75	6.91	-69	3.18	2.81	1.90	1.81	0.74	0.41
***h*-BN**	2.65	6.29	-69	3.15	2.71	2.06	1.92	0.92	0.54
MoS_2	3.81	23.32	-44	3.42	3.05	2.04	2.02	0.63	0.42
$MoSe_2$	3.87	26.44	-40	3.52	3.14	2.14	2.12	0.63	0.45
$MoTe_2$	3.98	29.84	-37	3.58	3.21	2.23	2.21	0.66	0.45
$TiSe_2$	3.36	24.38	-42	3.45	3.07	2.14	2.13	0.70	0.47

The slightly different value for hydrogen on the *h*-BN can be explained by the presence of two different atomic species on the same surface. This is a different scenario compared to the transition metal dichalcogenides and graphite, where the surface is occupied by a single atomic species.

These r_o seem to suggest that there is an *optimal* value for the overlap of atomic vdW radii that guides the height of the hydrogen on the surface and that eventually affects the adsorption energy. Thus the stronger polarizability of some atomic species is cancelled out by their larger atomic volume. This affects the position of the hydrogen molecule on the surface, that has to reach an *optimal* value for the atomic volume overlap in order to minimize the repulsion between the substrate and the adsorbate. Another interesting feature that can be highlighted from Table 5.4, is that also the overlap of the free atom volumes is similar for almost all the materials investigated (with the exception of the *h*-BN, due to the two–species surface). This result could in principle mean that it would be possible to predict within 0.1 Å accuracy the height of the hydrogen physisorbed on the surface knowing the atomic radii of the species and the averaged value of the radii overlap. Recently Alvarez has performed a comprehensive study about the vdW radii and the distribution of the distances of different elements physi- and chemisorbed to a particular probe element [210]. One finding of this study is that vdW interactions are characterised by a distance between two species which is 0.7 Å shorter than the sum of the vdW radii of the single species. This value refers to the free atoms and encouragingly agrees with the value of r_o obtained here for the overlap of the volumes of the free atoms.

The results reported in this chapter have shown that two of the vdW–dominated properties of the layered materials analysed here are very similar. Specifically it was discussed that interlayer binding energies and hydrogen adsorption energies span over a very narrow range of values. This seems to be due to a balance between the atomic polarizabilities and volumes. One of the findings of this study is that this balance, particularly in the hydrogen adsorption process, translates to an optimal value of the atomic volume overlap that consequently defines the distance of the hydrogen molecule from the surface and the energy of adsorption. Certainly more systems need to be analysed, including different surfaces and different adsorbates to further generalize this result. It would also be interesting to assess the performances of the best polarisable force fields [211] with respect to the semi-empirical and *ab-initio* vdW corrected density functionals. This will then be useful to set up accurate force field simulations in order to look also at the dynamics of the hydrogen

adsorption process on the different layered materials. However it is worthwhile to highlight that this finding can not only form the basis for further studies focused on understanding the adsorption process, but could also give insight for the design of new adsorbing materials.

Chapter 6

Exploring No Man's Land: Hydrogen Uptake by Potassium-intercalated Graphite

6.1 Introduction

Chapter 5 has shown that the adsorption energy of molecular hydrogen on different layered materials is not greatly affected by the atomic composition of the substrate. Despite the similarity of the hydrogen adsorption energy on the layered materials analysed, graphite had the strongest interaction with the gas molecule, and here the absorptive properties of a particular type of modified graphite will be further discussed.

Because of its anisotropy, graphite can absorb small molecules between the layers, however this process is not spontaneous. Fig. 6.1 shows that in order to absorb one hydrogen molecule, graphite needs to expand the interlayer spacing by $\sim 30\%$ leading to an interlayer distance of 5.50 Å. This occurs at an energetic cost which makes the absorption process in bare graphite unfavorable. However it is possible to intercalate other atoms between the graphite layers, that can penetrate graphite more easily and that can tune the interlayer spacing close to the optimal value. In the last thirty years, many studies showed how alkali metals, potassium, cesium and rubidium, can be easily intercalated in to graphite and they can increase the interlayer spacing even more than the $\sim 30\%$ [28, 212, 29, 213, 214, 215, 41]. Furthermore, a one electron donation from the metal to the graphite has been observed theoretically and experimentally, and this property is meant to be responsible for a stronger interaction

between the hydrogen molecule and the substrate [28, 216, 217, 218, 29, 42, 213].

Here a theoretical study is reported for hydrogen uptake in one particular graphite–intercalated–compound (GICs), namely the potassium compound KC_{24}.

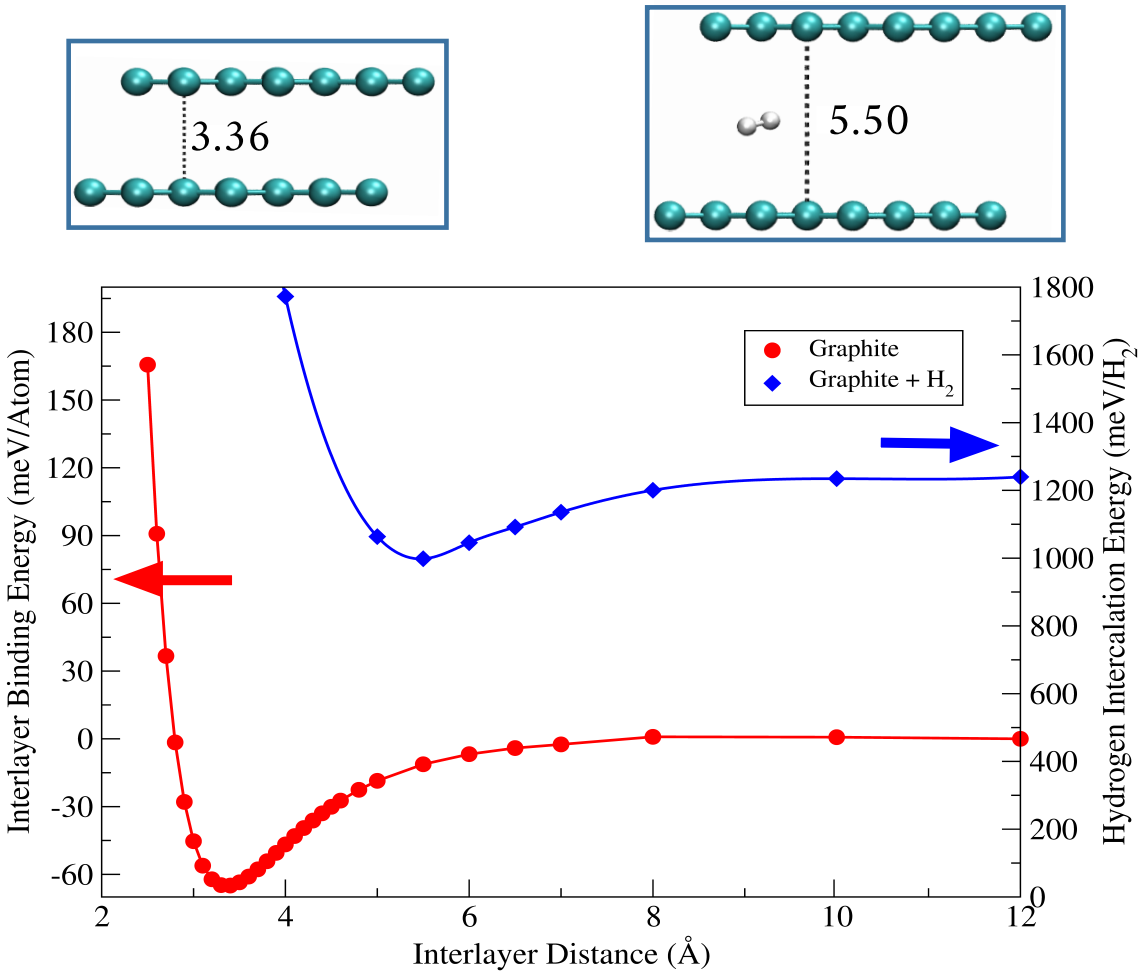

Figure 6.1: Interlayer binding energy of pristine graphite (red curve) and hydrogen intercalation energy (blue curve) calculated with the optB88-vdW functional. Graphite interlayer distance needs to expand up to 5.5 Å in order to absorb the hydrogen molecule, as shown in the upper panel of the figure. The blue curve shows that this process it is not spontaneous, and it arises at a high energy cost of ∼1 eV. The interlayer binding energy has been calculated using Eq. 3.2. The hydrogen intercalation energy has been calculated by subtracting the energy of an isolated hydrogen molecule (E_{H_2}), and the energy of the pristine graphite (E_{Graph}) from the total energy of the system ($E_{Graph-H_2}$): $E_{InterH_2} = E_{Graph-H_2} - E_{H_2} - E_{Graph}$.

Despite the influence of the GICs in the absorption of hydrogen for storage purposes, a full understanding of their properties and their interaction with the gas molecule is still missing. This is especially true in the case of the KC_{24}. Indeed for

this material a definitive structure is still not available. It is known that the KC_{24} is defined as a so–called stage–*2* material because the potassium atoms are absorbed every two graphite layers, bringing an alternation of full and empty interlayer areas (galleries, in jargon and hereafter). The empty galleries maintain the interlayer spacing of 3.33 Å and the A|B stacking sequence, while the full galleries expand to 5.4 Å [219, 29] and adopt an A|A stacking sequence. The reason for such a stacking of the full galleries is due to the potassium which is positioned in the hollow site of the first layer. This preferential position of the potassium atom drives the second layer to overlap exactly the first one. Then the third layer, which forms the empty gallery with the second one, overlaps following the natural stacking of the graphite, A|B [21].

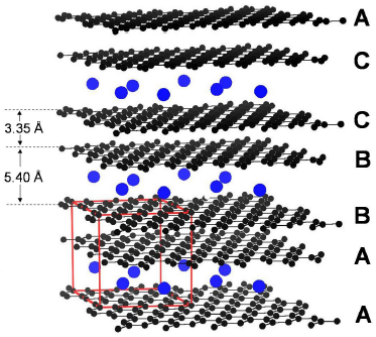

Figure 6.2: Stacking sequence in the KC_{24}. Figure from the J. Purewal, *Doctoral thesis*, California Institute of Technology (2010) [220].

The *in–plane* structure, on the other hand, is not well defined. At high temperature potassium atoms adopt a disordered, liquid–like structure [221] caused by a disorder–order transition found experimentally at about 126 K [222, 223, 224]. At low temperature, there is still not a full agreement between the X-ray diffraction pattern and the proposed models. The first proposed structure reported in Fig. 6.3 is obtained by populating the graphite layers with potassium atoms, forming a periodic triangular lattice and ensuring the KC_{24} stoichiometry. This structure is described as $(\sqrt{12} \times \sqrt{12})$-$R30°$ where the potassium lattice is incommensurate, that is rotated by 30° with respect to graphite. Although the $(\sqrt{12} \times \sqrt{12})$-$R30°$ structure reproduces the right stoichiometry and has been used as model for some theoretical studies [225], it is not consistent with X-ray diffraction [224]. Another incommensurate structure, the $(\sqrt{7} \times \sqrt{7})$-$R19.11°$, has been proposed on the basis of the low temperature in–plane structure of RbC_{24} and CsC_{24}. These two materi-

als have a domain structure, where the $(\sqrt{7} \times \sqrt{7})$-$R19.11°$ periodicity is observed. This kind of periodicity leads to a KC_{28} stoichiometry, which is balanced by a more dense concentration of potassium atoms in the boundary regions between the domains, that guarantees the final KC_{24} stoichiometry [224, 21]. Also this model is fully used in the theoretical studies, although experimental evidence has still not been found in the case of KC_{24}. The last structure is called relaxed closed–packed where the potassium atoms have been positioned at distances of $2a$, $\sqrt{7}a$ and $3a$ and were allowed to relax in the nearest hexagons centres. The resulting structure has a diffraction pattern more similar to the experiment, but due to the high number of atoms required for its description, it is not very used for the theoretical studies.

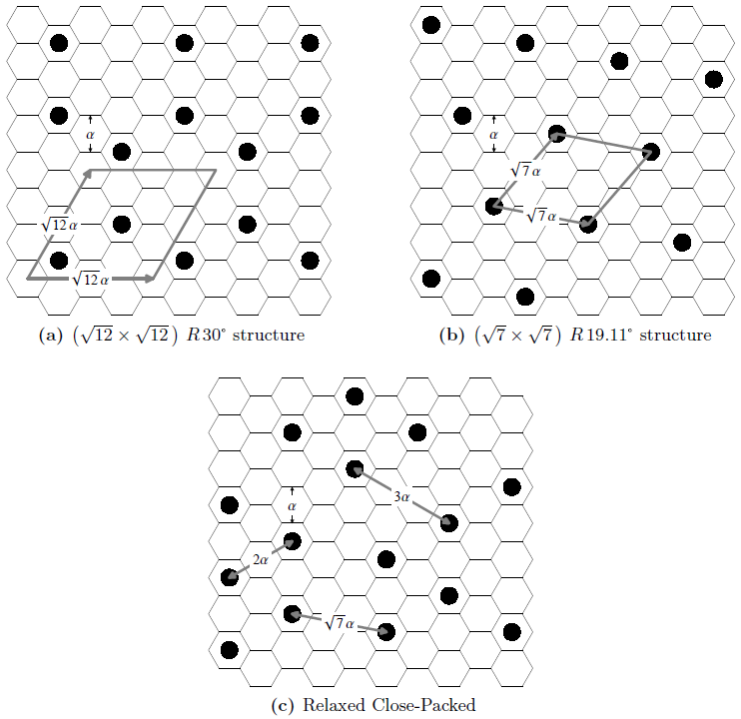

(a) $(\sqrt{12} \times \sqrt{12})$ $R30°$ structure

(b) $(\sqrt{7} \times \sqrt{7})$ $R19.11°$ structure

(c) Relaxed Close-Packed

Figure 6.3: Different structures proposed for KC_{24}. (a) refers to the $(\sqrt{12} \times \sqrt{12}$ *)*-$R30°$ structure with a KC_{24} stoichiometry. (b) refers to the $(\sqrt{7} \times \sqrt{7})$-$R19.11°$ with a KC_{28} stoichiometry. (c) shows the relaxed close–packed structure that is characterized by a liquid–like structure. Figure from the J. Purewal, *Doctoral thesis*, California Institute of Technology (2010) [220].

Here both the stoichiometric, $KC_{24,}$ and the structure of the domain with KC_{28} stoichiometry have been used to investigate the interaction between the substrate and the hydrogen, within the DFT framework. Other theoretical studies have been reported in the literature where the same hydrogen–KC_{24} interaction has been stud-

ied [30, 219, 29, 226]. However these studies were performed within the generalised gradient approximation, neglecting the vdW forces that must play a role in the hydrogen physisorption process. In addition an extensive study about the absorption energy as a function of the hydrogen concentration has still not been performed theoretically.

In the next sections a complementary study to the ones already reported in the literature will be presented, where the physisorption of hydrogen in KC_{24} has been studied as a function of the hydrogen concentration and including vdW interactions in the modeling of such process.

6.2 Methods

As in the other chapter, DFT calculations have been performed with the periodic plane–wave basis set code VASP 5.2 and the optB88-vdW exchange–correlation functional. PBE–based PAW potentials have been used and all the results reported have been obtained with hard potentials using a 900 eV plane–wave cut–off.

The convergence of the results to k-point sampling has been checked for KC_{24}. A Monkhorst-Pack k-point grid of $4 \times 4 \times 2$ per $(\sqrt{12} \times \sqrt{12})$ unit cell ensured that the intercalation energies were converged to within 0.02 meV.

Two different unit cells have been used for the KC_{24} and KC_{28} as reported in Fig. 6.4. The KC_{24} has been described using a $(\sqrt{12}\times\sqrt{12})$-$R30°$ unit cell containing 48 carbon and 2 potassium atoms. The KC_{28} has been described using a $(\sqrt{7}\times\sqrt{7})$-$R19.11°$ unit cell containing 28 carbon atoms and 1 potassium atom. In both cases the cell contains two layers of graphite in order to reproduce an AB|BA stacking. Geometry optimisation was performed in order to find the interlayer spacing of the intercalated and empty galleries. The interlayer spacings have been calculated changing the height of the unit cell in the range between 8.2 and 9.2 Å. In each cell the carbon atoms of one graphite layer have been fixed in all directions, while in the second layer they were fixed in the x and y directions and they were relaxed in the z direction. The potassium atoms were relaxed in all directions.

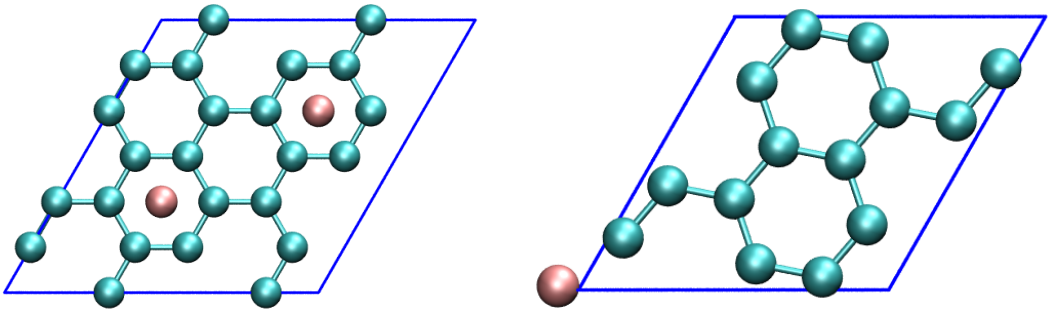

(a) KC_{24} (b) KC_{28}

Figure 6.4: Unit cell for KC_{24} and KC_{28}. (a) shows the $(\sqrt{12} \times \sqrt{12})$-$R30°$ cell and (b) shows the $(\sqrt{7} \times \sqrt{7})$-$R19.11°$ cell.

The interaction of hydrogen with the potassium-intercalated compounds has been investigated for both substrates. The hydrogen molecules have been placed in the centre of the empty hexagonal rings in KC_{28} and KC_{24} and the hydrogen concentration per potassium atom has been changed up to the complete saturation of the two unit cells, so KC_{28}–$(H_2)_x$, with $1 \leq x \leq 6$ and KC_{24}–$(H_2)_x$, with $1 \leq x \leq 5$ have been analysed. For KC_{28}–$(H_2)_x$ and KC_{24}–$(H_2)_x$, with $1 \leq x \leq 3$ the absorption energies for three different initial configurations of the hydrogen molecules have been calculated. The hydrogen molecule was initially positioned perpendicular with respect to the graphite layers and forming a T–shape with the potassium atom ($H_{\perp T}$), parallel to the graphite layer forming a T–shape with the potassium ($H_{\parallel T}$) and aligned with the potassium atom ($H_{\parallel K}$). In every configuration the molecules were positioned in the hollow site of the graphite layer at an initial distance of ~ 3 Å. All the initial configurations are reported in Fig. 6.5 and 6.6. A geometry optimization was then performed in order to obtain the final configuration of the hydrogen molecules and the final interlayer spacing.

The intercalation energy for the KC_{24} and KC_{28} (E_{Int}) has been calculated by subtracting the energy of an isolated potassium atom (E_{K}) multiplied by the number of the potassium atoms per unit cell (N), and the pristine graphite (E_{Grap}) from total energy of the intercalated system (E_{KCx}) and dividing by N:

$$E_{\mathrm{Int}} = \frac{E_{\mathrm{KCx}} - N \times E_{\mathrm{K}} - E_{\mathrm{Grap}}}{N} \tag{6.1}$$

The energies of graphite have been calculated using the same cells described before, without the potassium atoms and setting the interlayer spacing at 3.36 Å. The energy of the isolated potassium atom was obtained from calculations in a $12 \times 12 \times 12$ Å^3

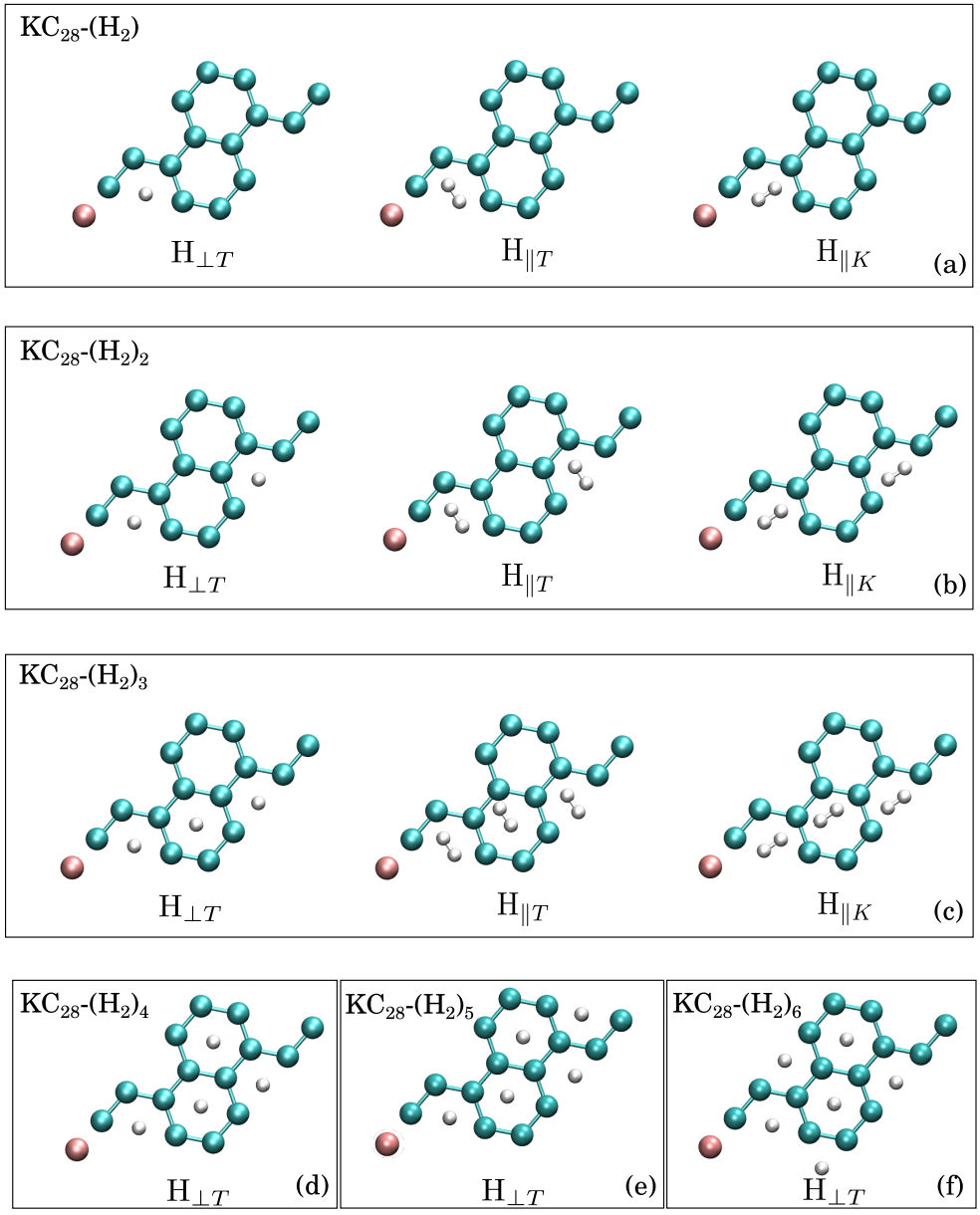

Figure 6.5: Initial configurations of hydrogen in the intercalated gallery of KC_{28}. (a) Different positions and orientations for the system KC_{28}–(H_2), where $H_{\perp T}$ describes the hydrogen molecule perpendicular to the substrate, forming a T–shape with the potassium atom, $H_{\parallel T}$ and $H_{\parallel K}$ describe the hydrogen molecule parallel to the substrate and forming T–shape with the potassium aligned to it respectively. (b) and (c) report the same configurations for the hydrogen molecules for KC_{28}–$(H_2)_2$ and KC_{28}–$(H_2)_3$, respectively. (d), (e) and (f) show the $H_{\parallel T}$ configuration for KC_{28}–$(H_2)_4$, KC_{28}–$(H_2)_5$ and KC_{28}–$(H_2)_6$, respectively.

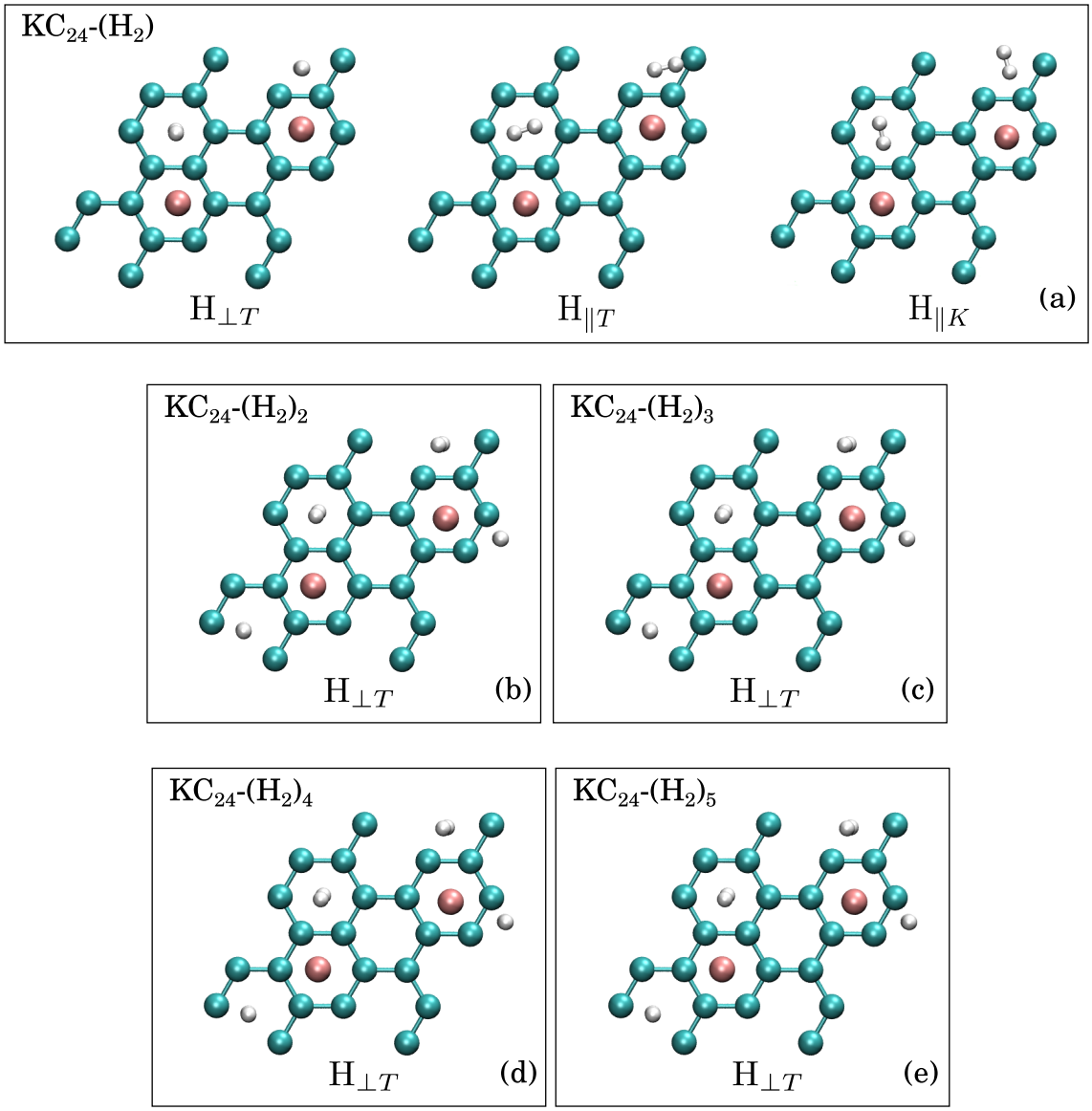

Figure 6.6: Initial configurations of hydrogen in the intercalated gallery of the KC_{24}. (a) Different positions and orientations for the system KC_{24}–(H_2), where $H_{\perp T}$ describes the hydrogen molecule perpendicular to the substrate, forming a T–shape with the potassium atom, $H_{\parallel T}$ and $H_{\parallel K}$ describe the hydrogen molecule parallel to the substrate and forming T–shape with the potassium aligned to it respectively. (b), (c), (d) and (e) show the $H_{\parallel T}$ configuration for KC_{24}–$(H_2)_2$, KC_{24}–$(H_2)_3$, KC_{24}–$(H_2)_4$ and KC_{24}–$(H_2)_5$, respectively.

box with Γ-point sampling.

The absorption energy for the hydrogen molecules in KC_{28} and KC_{24} (E_{Abs}) has been calculated by subtracting the energy of an isolated hydrogen molecule (E_{H_2}) multiplied by the number of molecules per unit cell (N), and the energy of the substrate (E_{KC_x}) from the total energy of the system ($E_{KC_x-H_2}$) and dividing by N:

$$E_{Abs} = \frac{E_{KC_x-H_2} - N \times E_{H_2} - E_{KC_x}}{N} \tag{6.2}$$

The energies of KC_{28} and KC_{24} have been calculated using the same cells described before, without the hydrogen molecules and setting the interlayer spacing at 5.40 Å. The energy of the isolated hydrogen molecule was obtained from calculations in a $12 \times 12 \times 12$ Å^3 box sampled at the Γ-point.

An estimate of the zero point energy (ZPE) was calculated using the harmonic approximation for frequencies obtained from the finite displacement method. For the whole system (i.e. carbon, potassium and hydrogen) vibrations were evaluated for the potassium and hydrogen atoms, while all the carbon atoms were fixed. Then the final ZPE was calculated by subtracting of the contributions of KC_x, where vibrations were evaluated for the potassium atoms while all the carbon atoms were fixed, and the isolated hydrogen molecule. Then the ZPE has been subtracted from all calculated absorption energies.

6.3 Results

6.3.1 The substrates: KC_{24} and KC_{28}

The first set of calculations focused on finding what are the different structural and energetic features of KC_{24}, described with a $(\sqrt{12} \times \sqrt{12})$-$R30°$ cell, and KC_{28}, described with a $(\sqrt{7} \times \sqrt{7})$-$R19.11°$ cell (Fig. 6.4), and if one of the two structures is energetically preferred. Fig. 6.7 shows the results of the geometry optimisation for both cells using the optB88-vdW functional. One can observe that the predicted interlayer spacings for the full and empty galleries for both materials are very similar, 5.36 Å and 5.33 Å for the full gallery of KC_{24} and KC_{28} respectively, and 3.34 Å for the empty galleries in both cases. These interlayer spacings for the intercalated galleries are in both cases in good agreement with the experimental value of 5.35 ± 0.01 Å obtained by neutron diffraction [29]. However the calculated intercalation energies, -6.00 eV for KC_{24} and -6.80 eV for KC_{28}, show a large difference of

$\sim$ 0.8 eV between the two. Fig. 6.7(c) and Fig. 6.7(d) show charge density difference plots for both structures, obtained by subtracting from the charge density of the KC_x the charge densities of graphite and potassium. From these pictures one can observe that there is an electron transfer from the potassium atom to the graphite atoms, a phenomenon which has already been observed experimentally [216, 217, 227] and makes the potassium atom positively charged. The Bader analysis reveals that the number of the valence electrons on the intercalated potassium atom is reduced from 9 to $\sim$ 8.15 and this extra charge is delocalised on the surrounding carbon atoms. This could be one of the possible reasons for the larger stability of the KC_{28} structure, where the positively charged potassium atoms are separated by 6.52 Å, compared to the case of KC_{24} where they are at shorter distance of 4.94 Å. In fact a rough estimate of the Coulomb potential energy difference of two systems composed by two positive charges separated by 6.52 Å in one case and by 4.94 Å in the other, gives a value of $\sim$ 0.7 eV, which is in line with the calculations.

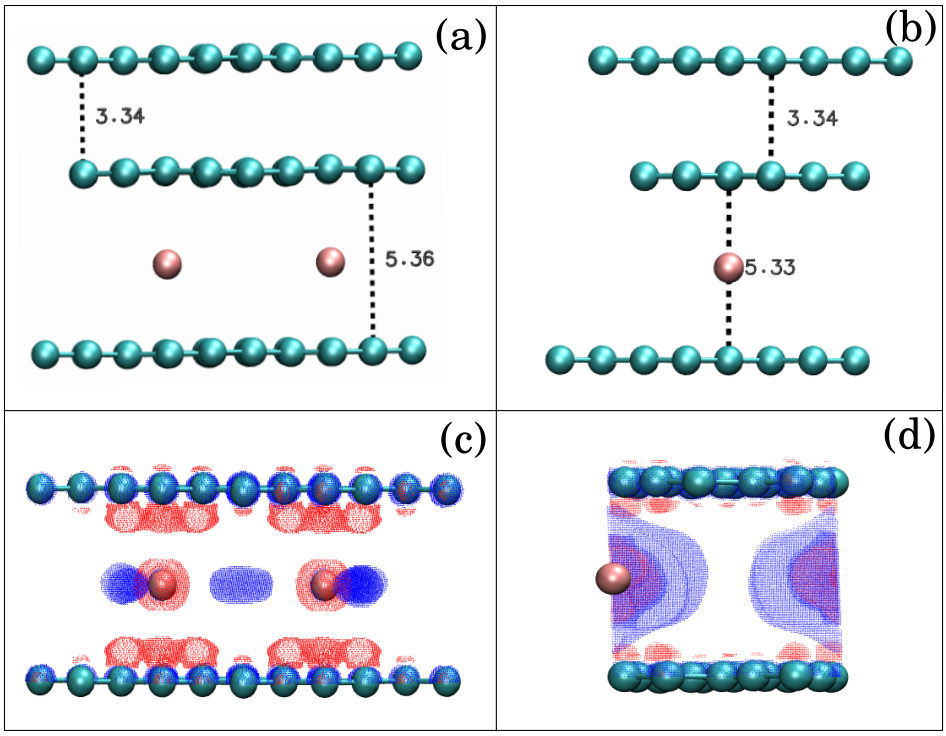

Figure 6.7: (a) and (b) show the final configurations from the geometry optimization of KC_{24} and KC_{28}, respectively. In (c) and (d) plots of the charge density difference at $\Delta\rho = \pm 0.013$ e/Å^3 for both materials are reported. The blue areas represent an electron charge depletion, the red ones an electron charge gain.

Looking at the substrate structure also provided the opportunity to examine the

role of vdW forces in the description of these materials. Calculations with the PBE functional, have been performed on two structures: KC_{14}, where the empty galleries have been neglected and KC_{28}. The PBE functional predicts the right interlayer spacing for KC_{14}, where the two graphite layers are held together by the presence of the charged potassium atoms. The presence of the empty galleries in KC_{28}, where the graphite layers are held together by pure vdW forces, makes the intercalation energy impossible to converge as a function of the unit cell dimension along the z direction, as can be seen in Fig. 6.8. These results suggest that the inclusion of vdW dispersion forces is essential for the accurate description of these particular intercalated compounds.

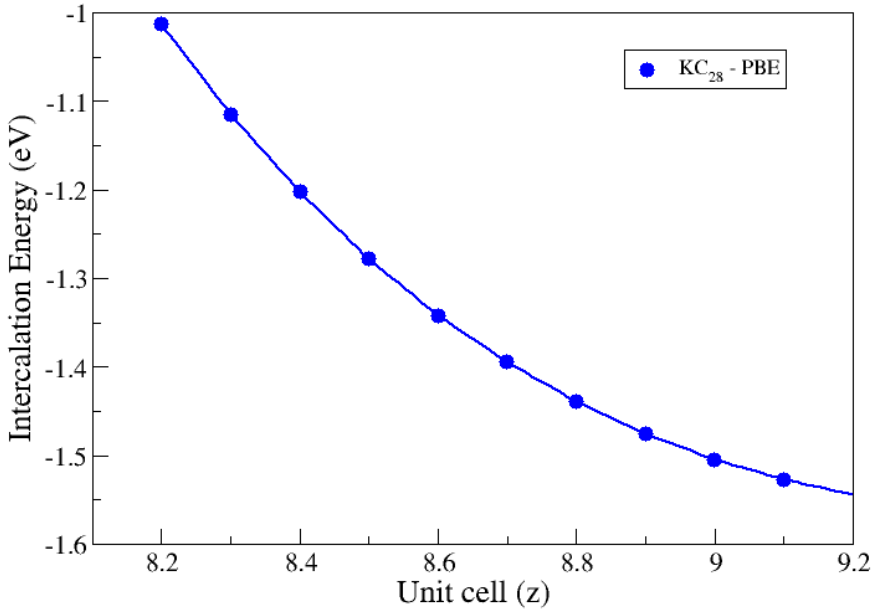

Figure 6.8: Intercalation energy calculated with the PBE functional as a function of the cell dimension in the z direction, for the case of KC_{28}. The energy continuously drops as the lattice expands because of the neglect of the vdW forces in PBE.

6.3.2 Hydrogen absorption in KC_{28} and KC_{24}

Once the two substrates, KC_{28} and KC_{24} have been optimised, their interaction with hydrogen has been investigated by looking at different hydrogen configurations and concentrations. Let us look first at hydrogen absorption in the case of the more stable

KC_{28} substrate. Here the absorption energy has been calculated using Eq. 6.2 for three different starting configurations of the hydrogen molecule, as shown in Fig. 6.5. The optimised structures for one molecule per potassium atoms are reported in Fig. 6.9, where one can see that the optimal configuration for the hydrogen molecule is to form a T–shape with the potassium. The geometry optimisation of the $H_{\parallel K}$ configuration (where the hydrogen molecule is parallel to the graphite plane and aligned to the potassium atom), in fact, still results in the hydrogen molecule forming a T–shape with the potassium atom, as illustrated in Fig. 6.9. The same behaviour has been observed for higher hydrogen concentrations.

From Table 6.1 the largest absorption energy is obtained when the hydrogen is oriented perpendicular to the surface, forming a T–shape with the potassium atom, and positioned in the hollow site at a distance of ~ 2.90 Å from the closest potassium atom. This result agrees with elastic and inelastic neutron scattering experiments [217, 227, 29] and previous theoretical calculations [228, 227, 29, 30].

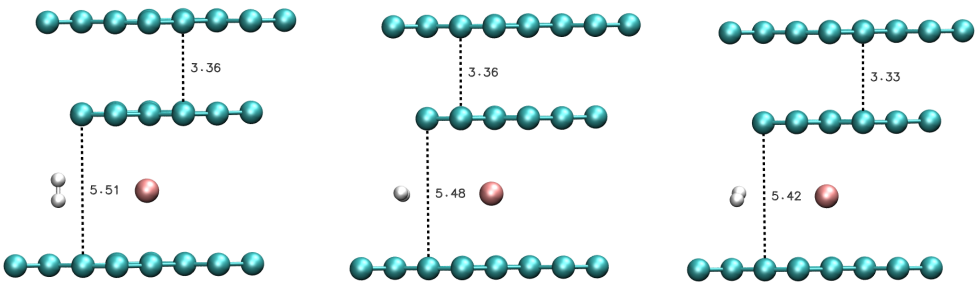

(a) $H_{\perp T}$ (b) $H_{\parallel T}$ (c) $H_{\parallel K}$

Figure 6.9: Optimised configurations of hydrogen in the intercalated gallery of KC_{28}. Here only the cases of one hydrogen molecule per potassium atom are reported. Similar results have been observed for the other hydrogen concentrations and the hydrogen absorption energies and the optimised interlayer distances are reported in Table 6.1. The interlayer distances for the intercalated galleries are also showed.

The reported results show also that the different configurations are non–degenerate as opposed to hydrogen adsorbed on pristine graphite, as shown in Chapter 5. Indeed hydrogen is free to move and rotate on the surface of pristine graphite, as it was found experimentally [229], however molecular rotations are already hindered if the shape of the carbon substrate is modified, as it was observed in the case of the carbon nanohorns [230]. Table 6.1 shows that the energy differences of the different orientations for a single hydrogen molecule per potassium are about 10-15 meV. The hindering of the rotation of the hydrogen molecule in the case of the intercalated

systems agrees with neutron scattering experiments, that found the hydrogen rotation to be obstructed when the molecule interacts with KC_{24} [227, 29]. This is due to the presence of the permanent quadrupole moment and an induced dipole in the hydrogen molecule caused by the electron transfer from the potassium to the graphite layers, which exposes the hydrogen molecule to a positively charged particle, as reported in Fig. 6.10. This result is in line with previous DFT calculations [30, 29, 226] in the case of KC_{14}, and it explains the preferential orientation of the hydrogen molecule. It must be noted that previous calculations were performed on the PBE level of approximation, however the inclusion of vdW interactions does not change the description of the electron transfer and the consequent induced dipole on the hydrogen molecule.

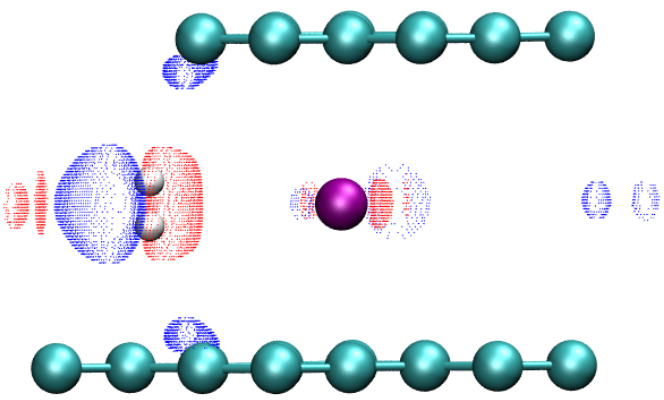

Figure 6.10: Plot of the charge density difference at $\Delta\rho = \pm 0.001$ e/Å^3 for hydrogen one molecule absorbed in KC_{28}. The red areas represent an electron charge depletion, the blue an electron charge gain.

Table 6.1 shows that moving to higher hydrogen concentrations, namely two and three molecules per potassium atom, the rotation of the molecule is even more obstructed, leading to a larger difference of about 20-25 meV between the most stable configuration, $H_{\perp T}$ and the less stable ones, $H_{\parallel T}$ and $H_{\parallel K}$. This is the reason why for hydrogen concentrations higher than three molecules per potassium atom, only the $H_{\perp T}$ configuration has been investigated.

Table 6.1: Results for the interlayer spacing of the full gallery of the KC_{28} and absorption energies at different hydrogen concentration (x) per potassium atom and configurations. The different configurations are named according the Fig. 6.5. The energies have been corrected for the zero point energy ($\sim$ 50 meV).

x	**Interlayer spacing (Å)**			**Absorption energy (meV)**		
	$H_{\perp T}$	$H_{\parallel T}$	$H_{\parallel K}$	$H_{\perp T}$	$H_{\parallel T}$	$H_{\parallel K}$
1	5.51	5.48	5.42	-121	-107	-112
2	5.64	5.54	5.61	-151	-125	-127
3	5.77	5.84	5.71	-147	-126	-126
4	5.75			-11		
5	5.72			81		
6	5.73			127		

The absorption energies as a function of the hydrogen concentration in Table 6.1 show that the largest values are obtained for the medium concentrations, that is two and three hydrogen molecules per potassium atom. This means that the optimal capacity of KC_{28} is between two and three hydrogen molecules per potassium atom, as shown in Fig. 6.11. Also this result is in line with the experiments reported in the literature. Works by Watanabe *et al.* [231], Lovell *et al.* [29] and also Purewal *et al.* [219] found a concentration slightly higher than two hydrogen molecules ($\sim$ 2.10) per potassium atom. Within this range of concentrations the average distance between the centre of mass of the hydrogen molecules close to the potassium atoms is about 3.26 Å, which is very much in line with the distance corresponding to the minimum of the H_2–H_2 intermolecular potential ($\sim$ 3.25 Å) [13, 232]. Thus, it is possible to assume that within this range of concentrations, in addition to the interaction between hydrogen and the substrate are attractive, also the H_2–H_2 interactions are attractive, therefor stabilise the adsorption energies.

The present DFT calculations predict the interlayer spacing of the full galleries in the cases of the medium concentrations to be 5.64 and 5.77 Å, for two and three hydrogen molecules per potassium, respectively. These values are in line with the experimental value of 5.64 ± 0.01 Å, corresponding to the saturation state, that is $\sim$ KC_{28}–$(H_2)_2$ [29]. It is also interesting to note that the intercalated galleries expand even further during the absorption process, going from 5.36 Å to about

5.75 Å for high hydrogen concentrations. This further expansion of the galleries has been also claimed to have a role in the thermodynamics of the whole hydrogen absorption process [217, 231].

Let us look closely at the energies of absorption. A value for the enthalpy of absorption of ~ -93 meV at half coverage (that we believe to correspond to $\sim KC_{28}$–$(H_2)_1$ in our case) has in fact been obtained from isotherms in the temperature range of 63 and 196 K [233, 231]. The optB88-vdW functional predicts a ZPE corrected adsorption energy of a single hydrogen molecule per potassium of ~ -121 meV, which is overestimated by $\sim 30\%$ compared to the experiment. Previous calculations were performed by using the PBE functional for the KC_{14} system, where the empty galleries were neglected, and predict an absorption energy of -78 meV [30, 226]. The ZPE correction reported for the PBE calculations, however is almost four times smaller than the ZPE in the present calculations. In the former case, only the motion of the hydrogen centre of mass has been evaluated, as opposed to the present study where the entire system has been assessed. It must also be noted that both DFT calculations of the absorption energies have been performed at 0 K. In order to have a proper comparison against the experimental value, the effect of the temperature needs to be taken into account. It can be estimated by correcting the calculated value by RT, where R is the Botzmann constant and T is the temperature. For the temperature on the experimental range, RT is ~ 11 meV, and it brings the optB88-vdW adsorption energy closer to the experiment with a value of ~ -110 meV, while it makes the PBE prediction worse, leading to an adsorption energy of ~ -68 meV. The difference between the results of this work obtained with the optB88-vdW and the PBE results in Ref. [30, 226] is due to the lack of the long range correlation contribution to the absorption energy in the case of the PBE calculations. It was also found that the inclusion of the empty galleries does not seem to be relevant for the value of the absorption energy. Indeed the absorption energy of a single hydrogen molecule in KC_{14} (-121 meV) using optB88-vdW is very much in line with the absorption energy in KC_{28} (-121 meV) at 0 K.

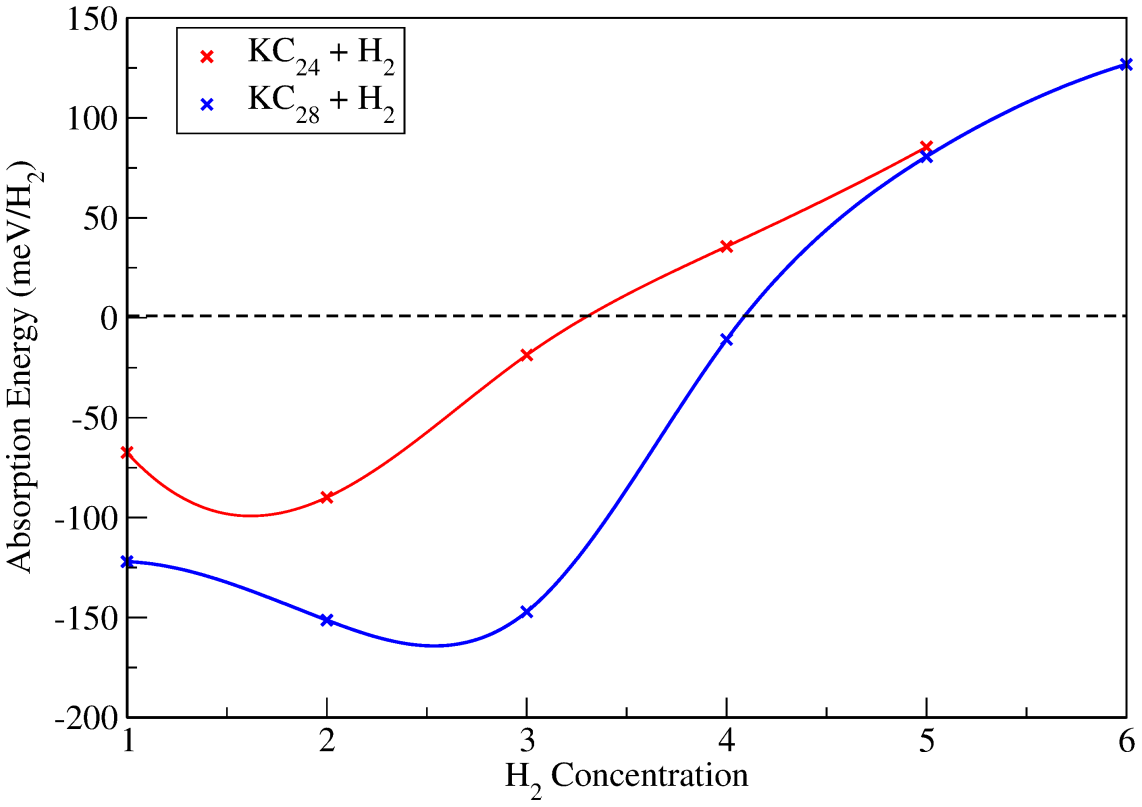

Figure 6.11: Absorption energy as a function of hydrogen concentration in KC_{24} and KC_{28} calculated with the optB88-vdW functional.

A similar investigation of the hydrogen absorption has been performed for KC_{24}, with the complete configuration analysis for one, two and three hydrogen molecules per potassium atom. From Table 6.2 and from Fig. 6.12 it can be seen that in spite of the starting hydrogen molecule configurations, a hydrogen molecule prefers to form a T–shape with the potassium atom in the final optimised structures. Table 6.2 shows that for hydrogen concentrations larger than one molecule per potassium atom, the optimized structures are basically degenerate. The largest difference in the absorption energy is ~ 17 meV, which is reported just for the case of one hydrogen molecule per potassium atom. For concentrations higher than three hydrogen molecules per potassium atom, that is KC_{24}–$(H_2)_4$ and KC_{24}–$(H_2)_5$ only $H_{\perp T}$ and $H_{\parallel T}$ starting configurations have been investigated. Results in Table 6.2 show that also the intercalated gallery of the KC_{24} expands up to $\sim 6\%$ as it was found in the case of the KC_{28}. Fig. 6.11 shows that the most stable system has a hydrogen concentration between one and two hydrogen molecules per potassium atom. This result is lower than the value of 2.10 hydrogen molecules per potassium atom found experimentally. The absorption energy of -67 meV in the case of the KC_{24}–$(H_2)_1$

is slightly underestimated with respect to the experimental value of ~ -93 meV in the temperature range of 63 and 196 K [233, 231]. This difference between theory and experiment is even more dramatic when the temperature effect is taken into account by including the RT correction, which in this case brings the prediction of the adsorption energy to ~ -57 meV.

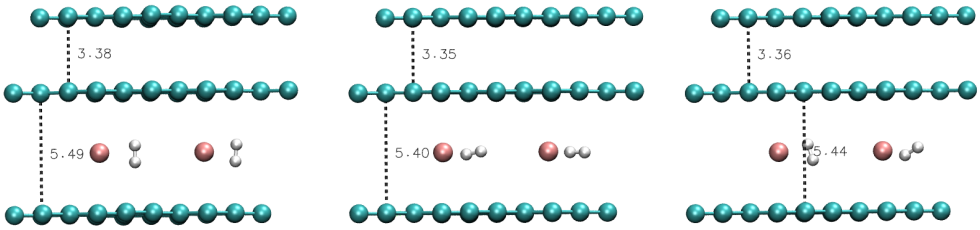

(a) $H_{\perp T}$ (b) $H_{\parallel T}$ (c) $H_{\parallel K}$

Figure 6.12: Optimised configurations of hydrogen in the intercalated gallery of the KC_{24}. Here only the case of one hydrogen molecule per potassium atom is reported. Similar results have been observed for the other hydrogen concentrations and the hydrogen absorption energies and the optimised interlayer distances are reported in Table 6.2. The interlayer distances for the intercalated galleries are also showed.

Table 6.2: Results for the interlayer spacing of the full gallery of KC_{24} and absorption energies at different hydrogen concentration (x) per potassium atom and configurations. The different configurations are named according to Fig. 6.5. The energies have been corrected for the zero point energy ($\sim$ 50 meV).

x	**Interlayer spacing (Å)**			**Absorption energy (meV)**		
	$H_{\perp T}$	$H_{\parallel T}$	$H_{\parallel K}$	$H_{\perp T}$	$H_{\parallel T}$	$H_{\parallel K}$
1	5.49	5.40	5.44	-67	-50	-67
2	5.64	5.54	5.61	-90	-98	-72
3	5.70	5.70	5.66	-19	-22	24
4	5.70	5.71		36	49	
5	5.69	5.67		85	99	

6.4 Discussion and Conclusion

The results reported here show a preliminary analysis of the interaction between hydrogen and the KC_{24} GIC using the optB88-vdW functional. The first set of calculations show how it is possible to discriminate between two of the most used structural models of KC_{24} in the computational studies, namely the $(\sqrt{12} \times \sqrt{12})$-$R30°$ that corresponds to a stoichiometry of KC_{24}, and $(\sqrt{7} \times \sqrt{7})$-$R19.11°$ domains structure that corresponds to a local stoichiometry of KC_{28}. The intercalation energy of the domains structure, KC_{28}, is ~ 0.8 eV lower than the energy of the KC_{24}, due to a larger separation of the positive potassium atoms in the galleries, that stabilises this structure. In addition it was also checked that the inclusion of dispersion forces is essential for the description of this material, due to the presence of the empty galleries of graphite which are held together by pure vdW forces. Indeed, unless the empty galleries are neglected, the PBE functional fails in the description of this material.

KC_{24} and KC_{28} show different behaviour when it comes to the hydrogen adsorption, with the latter substrate showing closer properties to the ones measured in the experiment. This suggests that the proposed structure formed by domains of KC_{28}, similar to the structure found for CsC_{24} and RbC_{24}, is a good model for the still not fully determined structure of KC_{24}. The optB88-vdW functional performs well in the description of this system, predicting the right concentration of absorbed hydrogen in KC_{24} (in this case KC_{28}) of about two molecules per potassium atom. The preferential configuration of the hydrogen molecule is a T–shape with the potassium atom. This is due to the presence of the permanent quadrupole moment and the dipole moment induced on the H_2 molecule due to the charge migration towards the potassium atom. The calculated K^+–H_2 distance of ~ 2.90 Å and the interlayer spacing of the intercalated galleries of ~ 5.64 Å are in good agreement with experiment [29]. The absorption energy calculated for half of the saturate state (KC_{28}–$(H_2)_1$), that is one hydrogen molecule per potassium atom is -110 meV, slightly overestimated compared to experimental value of ~ -93 meV, but in better agreement if the temperature effect is taken into account. The PBE prediction of the hydrogen absorption energy is underestimated compared to experiment [29, 226, 30]. This indicates that the inclusion of vdW forces needs to be taken into account to proper predict the interaction between the hydrogen and the substrate.

This study is the first attempt in describing hydrogen physisorption in KC_{24} by including all the relevant physical properties such as vdW interactions, ZPE and

a good model of the substrate and hydrogen concentration. This forms a basis for a good model in order to further investigate the finer details of this process like the proposed quantum delocalization of the single hydrogen molecule in the system [29, 219] or the role of the potassium concentration in tuning the strength of the hydrogen absorption.

Chapter 7

Summary and Outlook

This work focused on the study of different features of layered materials: structure, bond energetics, atomic dynamics and adsorptive properties. The newly developed vdW–inclusive functionals within the DFT framework have been exploited in order to understand the role of the long–range dispersive forces, that is the vdWs, in the aforementioned properties of these materials. Here the findings of this work will be joined together in order to draw a general conclusion and highlight how these results can open up new questions and form the basis for new studies.

Two of the most popular layered materials, graphite and the isoelectronic *h*-BN, have been used to benchmark several of the newly developed vdW–inclusive density functionals. The results in Chapter 3 show that, among the functionals used, optB88-vdW gives the best prediction of the structure and bond energetics of the two materials. This result has been verified for both the covalent bonds between the atoms within the layer and vdW interactions between the layers. Strong similarities, especially between the interlayer distances and binding energies of graphite and *h*-BN, have also been highlighted. The decomposition of the interlayer binding energies into the different contributions revealed that this is due to a balance between the repulsive electrostatic interactions (collected in the exchange correlation energy) and the attractive vdW interactions (summed in the non–local correlation energy).

The same similarity of the interlayer binding energies have been found for other layered materials, like transition metal dichalcogenides as reported in Chapter 5 and in other works in the literature [40, 38, 39]. More interestingly, physisorption of molecular hydrogen has been found to be surprisingly similar on the surface of the layered materials investigated. Hydrogen physisorption is another process mostly driven by vdW forces, and our findings show that this is not significantly affected

by different atomic composition, structure and polarizability of the surface. Also in this case, this similarity results from a balance between repulsive and attractive contributions to the adsorption energy. More precisely the larger polarizability of atoms on the surface is counterbalanced by a larger vdW radius. This leads to an optimal overlap of the vdW radius of the atoms on the surface and the vdW radius of the hydrogen that is about 0.7 Å. It seems that the overlap of the atomic volumes define the distance of the hydrogen molecule from the surface and consequently the adsorption energy. Although our finding is in line with what has been reported recently by Alvarez [210], still more studies are needed to confirm this value as a constant that can be used to predict the distance of molecules from surfaces in the physisorption regime. Indeed, this finding needs to be tested against more complex adsorbates (from water to large organic molecules) and different substrates.

It will also be interesting to explore if a similar trend seen for the hydrogen adsorption on the surface of layered materials, is still verified for hydrogen physisorption in a confined space, like between the layers. The vast plethora of substrates that can be investigated not only includes, graphite, *h*-BN, all the transition metal dichalcogenides, layered oxides and other inorganic layered materials, but also the newly proposed *vdW heterostruscutres* [234]. Because of the easy exfoliation of layered materials, it is possible to combine different layers to form heterostructures, which are characterised by different electronic and optical properties compared to the single components [234]. Furthermore these properties can be tuned by the combination of the different layers and by the different number of layers of each single component. It would be interesting to study the behaviour of hydrogen also in this sort of asymmetric confined environment.

Hydrogen absorption between two layers has been investigated in this thesis for the particular case of potassium intercalated graphite. This system has been chosen because of its promising technological application in the hydrogen storage field. In fact the intercalation of potassium in graphite up to a concentration of KC_{24} can expand the natural interlayer spacing of graphite, reducing the H_2–intercalation energy barrier. In addition, the alkali metal polarises the hydrogen molecule leading to a stronger H_2–substrate interaction which can increase the quantity of hydrogen stored in these layered materials, as discussed in Chapters 1 and 6. Although this system has been extensively studied experimentally [226, 28, 42, 29, 219, 30], still some details need to be understood. One of the main questions is related to the definition of the orientation of the hydrogen molecule and the extent of the translational delocalisation. Different theoretical studies have been reported to complement the

experiments [29, 30, 226], which however have not been able to shed much light on the translational delocalisation. These works made use of various approximations, more specifically on the model of the substrate, the neglect of the vdW forces, and quantum nuclear effects (QNE). In Chapter 6 the role of some of these approximations in the theoretical description of the physisorption of hydrogen in KC_{24} was addressed by using a complete description of the substrate and by explicitly including the vdW forces. The absorption energy of the hydrogen molecule in KC_{24} has been investigated as a function of the hydrogen concentration and configurations in two different models of the substrate, namely KC_{24} and KC_{28}. The encouraging agreement of the results of the hydrogen concentration and adsorption energy reported in Chapter 6, suggests that the model proposed here for hydrogen physisorption in KC_{24} can be used for further investigation of this process.

QNE has been claimed to be responsible for the orientation and translational delocalisation of hydrogen in KC_{24}, and it needs to be included in the simulations to reconcile theory and experiment [226]. Although higher order QNEs (more than the zero point energy contribution) have not been included in the description of hydrogen physisorption in graphite, results in Chapter 4 reveal that this is important not only for a good description of the hydrogen molecule, but it can also be important for the accurate description of the substrate itself. By comparing experimental values to different theoretical approaches, it was shown that QNEs can affect the dynamics of the carbon atoms. In particular it was shown that the in–plane and out–of–plane carbon displacements cannot be predicted with the same level of accuracy within the harmonic approximation. Furthermore it was highlighted that the description of the carbon atom as a classical nucleus is no longer valid at temperatures lower than 300 K. Thus particular care is needed for the prediction of the quantum dynamics of small molecules like hydrogen on top and in between graphite layers at such low temperatures, where the hydrogen physisorption occurs.

In Chapters 3, 4, 5 and 6 it was highlighted that the effect of vdW forces and the role of quantum dynamics need strictly to be taken into account if we want to explore by theory not only layered materials themselves, but also some of their applications. In Chapters 5 and 6 layered materials have been investigated as substrates for the hydrogen storage. In fact the safe and efficient storage of hydrogen for mobile applications remains an unsolved challenge. Particularly in Chapter 6 it was discussed how potassium intercalation in graphite is one promising solution to this problem, however it is still not the definitive one. Even at 77 K only physisorbed hydrogen reaches only 1%wt, however KC_{24} is the perfect template in order to achieve

a molecular understanding of the physisorption process driven by stronger interactions than the vdW. In fact in this substrate there is only one site for the hydrogen adsorption and it can be easily studied using both theory and experiment.

One of the other fascinating properties of potassium intercalated compounds that is worth further study, is related to the possibility of *tuning* the strength of the hydrogen adsorption by changing the potassium concentration. In fact the concentration of the metal in the substrate can control whether chemical adsorption or physisorption of the hydrogen takes place. High concentration of potassium in the graphite (KC_8) leads to the breaking of the hydrogen molecule and the formation of new covalent bonds between H atoms and the substrate. On the other side low concentrations of potassium (KC_{24}) lead to the physisorption of the gas. The absorption process at the intermediate potassium doping remains still unexplored. On the basis of this trend, it is possible that new sorption regimes, which would imply stronger H_2–substrate interactions compared to physisorption, but still not so strong as in the chemisorption regime, may arise from intermediate potassium concentrations. The lack of information about the intermediate concentration has been obstructed by practical difficulties in tuning of the potassium concentration in this regime. However, recently Howard *et al.* have been able to tune the potassium doping in graphene and few layer (1-4) graphene (FLG) specimens [235], resulting in the formation of expanded, stage-*1* intercalated compounds (that is, the alkali metal will occupy all layers). The results in Chapter 6 have shown that the inclusion of the empty gallery does not affect the nature of the hydrogen–adsorption. Therefore, this substrate can be safely used to look at hydrogen absorption as a function of potassium concentration. Furthermore our very recent quasi–elastic neutron scattering experiment confirms that the hydrogen adsorption process on the *expanded* KC_8 are in line with the previous study of *unexpanded* KC_8 [42, 213] (see Appendix C). Of course other kinds of substrates and interactions need to be further investigated. Beyond layered materials, metal organic frameworks for example have been shown to be good porous sorbents but deeper analysis are still necessary. In addition Kubas interactions based on the formation of metal–hydrogen complexes are also very fascinating because their strength can be tuned by changing the number of the metal sites and their oxidation state [24].

Overall, we hope that this work has contributed to a deeper understanding of the fundamental properties of layered materials and that the models proposed here can form the basis for further study including the large technological application of these materials.

Appendix A

Measurement of the graphite vibrational density of states: TOSCA experiment

The graphite vibrational density of state (v–DOS) has been measured experimentally using the TOSCA spectrometer at ISIS neutron spallation source.

Various experimental measurements of different regions of the phonon dispersion relation are reported in the literature, from which it is possible to describe most of the graphite lattice vibrations. First and second order Raman spectroscopy has been used to look at some of the prominent features of graphite dynamics, i.e. the in–plane bond stretching modes and the out–of plane shearing mode [143, 148, 153, 152, 150, 151], which are compatible with the selection rules of the technique. Other precise measurements of the optical in–plane vibrations of graphite have been carried out by means of X-ray diffraction by Maultzsch *et al.* [144] in 2004 while a more complete pictures of the phonon dispersion relation was provided by Mohr *et al.* [145] in 2007. The longitudinal acoustic modes have been measured by inelastic neutron scattering in 1962 by Dolling *et al.* [236] and in 1971 by Nicklow *et al.* [179]. These last two experiments obtained the frequencies of the longitudinal acoustic modes in the [001] direction, and limited information on the other modes (optical and in-plane vibrations); moreover, these experiments were limited by the quality of the sample, which showed a quite high angular spread of the c axis, and by the quality of instrumentation. A complete spectrum of the lattice vibrations of graphite obtained with only one kind of technique is still not reported in the literature.

The lack of selection rules for the neutron probe and the large energy range that

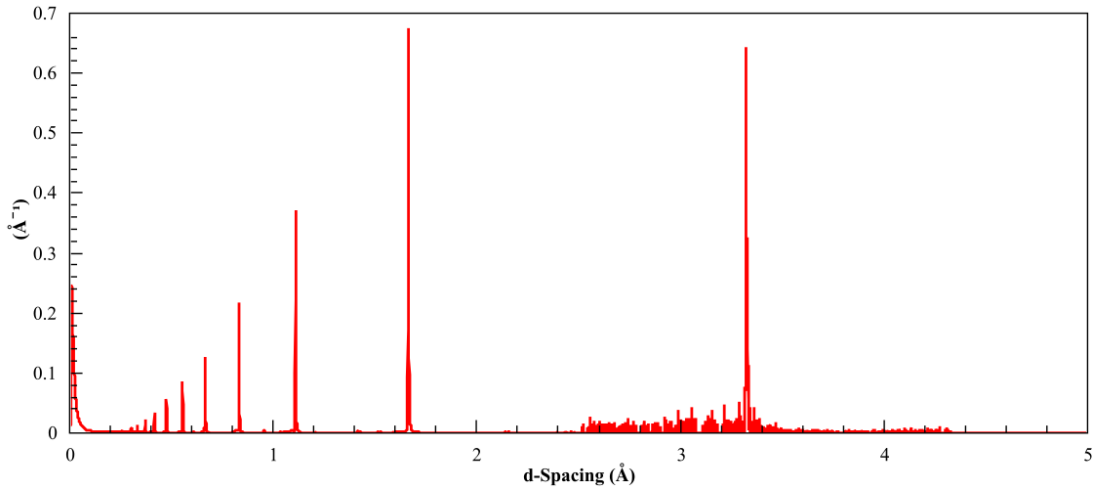

Figure A.1: Diffraction pattern of HOPG measured by the TOSCA spectrometer.

can be analyzed using this technique will allow a fingerprint of the material to be obtain with a single measurement, overcoming the limits of the other techniques such as IR- and Raman spectroscopy and X-ray diffraction. In addition, the excellent resolution of the TOSCA instrument makes it a very powerful tool and a very unique technique to look a the v–DOS of graphite. Thus the main objective of this experiment was to use the TOSCA spectrometer in order to obtain complete high-resolution inelastic neutron scattering spectra for highly oriented pyrolytic graphite (HOPG). This material is characterized by the ordered orientation of the graphite planes along the c axis, and a disordered orientation of the planes along the a and b axis. That is why it can be treated as a powder along the in–plane direction and a single crystal along the out–of–plane. The accurate information that can be obtained, especially for the out–of–plain dynamics, can therefor used to benchmark even further the computational techniques most commonly used to simulate the atoms dynamics, in a similar vein of the study reported in Chapter 4.

During the experiment, a HOPG plate (30 mm x 40mm x 2mm in size) has been investigated using the TOSCA spectrometer at a temperature of 10 K. HOPG was aligned using TOSCA's diffraction bank in order to have the c axis of the material parallel with respect to the incident beam. The alignment of the sample was achieved by tracking the intensity of the (006) Bragg reflection at specific diffraction detectors over an angular range of 20 degrees. A representative diffraction pattern is shown in Figure A.1.

Following this alignment procedure, inelastic neutron-scattering spectra were collected at a series of orientations of the c axis relative to the incident neutron

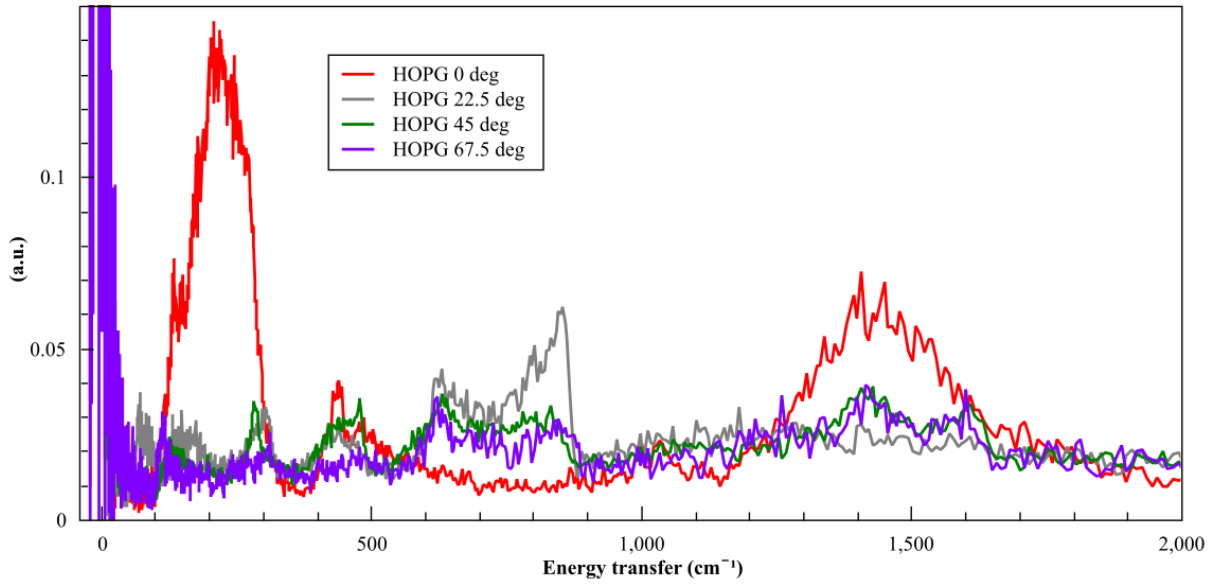

Figure A.2: Inelastic neutron scattering spectrum of HOPG at different orientations of the c axis with respect to the incident beam.

beam, namely at 0.0°, 22.5°, 45.0° and 67.5°. A representative spectrum is shown in Figure A.2.

However an accurate analysis of these data including a comparison with theoretical predictions of the TOSCA spectra are currently underway.

Appendix B

Momentum distribution of carbon atoms in graphite: VESUVIO experiment

The momentum distribution of carbon atoms in graphite has been measured at different temperatures using the VESUVIO spectrometer at the ISIS neutron spallation source facility. As already mentioned in Chapter 4, VESUVIO spectrometer allows to look directly at the momentum distribution of the individual atoms. This means that this information can be accessed circumventing a structure refinement procedure, and thus they can complement the measurement of the ADPs arising from the refinement of the diffraction patterns.

During the experiment powder graphite and HOPG were analysed at 4 K and 300 K, in order to obtain the isotropic momentum distribution from the measurement of powder graphite and the directional contributions, that is along the plane and out–of–plane of graphite, to the isotropic momentum distribution from HOPG. It must to be noted that a similar experiment was performed in 1998 by Fielding *et al.* [237] using the previous configuration of VESUVIO. In that instance the measurements were performed just at 300 K, in addition the samples were mounted in aluminium cells making difficult the separation between the signal coming from the sample and that coming from the cell. In the present experiment the samples were mounted in bespoke tin cans in order to make the sample and the cell peaks more separable.

The signal obtained experimentally reported in Fig. B.1 is the Compton profile, $J(y)$, that is the probability distribution to measure y (which is the projection

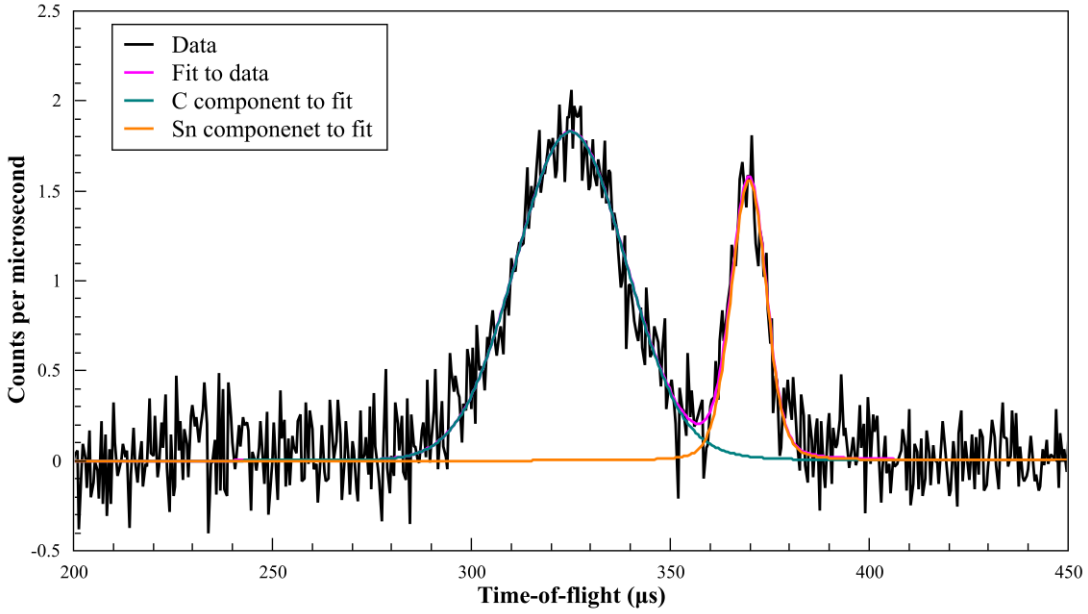

Figure B.1: Powder graphite Compton profile measured at 300 K. The main peak at 340 μs refers to the graphite and that at 380 μs refers to the tin can.

of the nuclear momentum along the scattering vector), along a given direction of the momentum transfer. In deep inelastic neutron scattering measurements, the Compton profile can be approximated to a Gaussian, and the standard deviation, σ, corresponds the second moment of the momentum distribution. It can be calculated as the integral of the phonon frequencies, $\omega_{\vec{q}}$, and the eigenvectors $\vec{e}_{\vec{q}k,n}$, along a direction defined direction ($\overrightarrow{q}$) as follows:

$$\sigma_n(\overrightarrow{q})^2 = \frac{m_n}{N_q\hbar^2}\int \omega_{\vec{q}}[\vec{e}_{\vec{q},n}\cdot\vec{e}^*_{\vec{q},n}]\coth\left(\frac{\hbar\omega_{\vec{q}}}{2k_BT}\right)\mathrm{d}\omega\mathrm{d}q, \tag{B.1}$$

where m_n is the atomic mass of the nucleus, N_q is the total number of **q** points sampled in the Brillouin zone, $\vec{e}^*_{\vec{q},n}$ is the eigenvector complex conjugate, and coth $\left(\frac{\hbar\omega_{\vec{q}}}{2k_BT}\right)$ accounts for the phonon population as a function of temperature.

The isotropic value of the width of the momentum distribution is then given by the average of σ along the three spatial direction x, y, z:

$$\sigma^2_{\mathrm{iso}} = \frac{\sigma(\hat{x})^2+\sigma(\hat{y})^2+\sigma(\hat{z})^2}{3}. \tag{B.2}$$

The second moment of the momentum distribution can be predicted following a procedure very similar to the calculation of the ADPs from the computed eigenvectors and frequencies from DFT simulations. Knowing the second moment of the

momentum distribution of the individual atoms allows to obtain their mean kinetic energy from the simple relation:

$$\langle E_k(\hat{q})\rangle = \frac{3\hbar\sigma^2}{2m_n}, \tag{B.3}$$

and therefor a straightforward measurement of the ZPE of the atoms.

The comparison between experimental and predicted values of the second moment of the momentum distribution and the kinetic energy as reported in Table B.1 will be used to assess even further the adequacy of first principles models within the harmonic approximation in the description of the carbon dynamics as a function of temperature. However the preliminary results in Table B.1 anticipate a trend of the in–plane and out–of–plane properties, especially at low temperature, in line with the trend of the ADPs discussed in Chapter 4.

Table B.1: Experimental and calculated second moments of the momentum distribution (σ) and mean kinetic energies (E_k) per carbon atom along the in–plane (x), out–of–plane (z) and averaged along all the directions (iso). σ is always expressed in Å^{-1} and E_k in eV. The present experiment is currently under examination, therefor the values reported here correspond to a first estimate of σ and E_k.

4 K						
Functional	$\sigma(\hat{x})$	$\sigma(\hat{z})$	σ_{iso}	$E_k(\hat{x})$	$E_k(\hat{z})$	$E_k$iso
LDA	14.97	10.36	13.60	0.116	0.056	0.096
PBE	13.84	9.69	12.44	0.099	0.047	0.080
DFT-D2	14.84	10.33	13.34	0.114	0.055	0.092
vdW-DF2	13.76	9.66	12.37	0.098	0.0483	0.079
optPBE-vdW	14.77	10.28	13.27	0.113	0.055	0.091
optB88-vdW	14.80	10.31	13.30	0.113	0.055	0.091
Powder (prelim.)			∼13.00±0.18			0.087
HOPG (prelim.)	∼14.5±0.1	∼11.5±0.1	∼13.5±0.1	∼0.109±0.001	∼0.068±0.001	∼0.094±0.001
300 K						
LDA	11.52	8.57	10.54	0.069	0.038	0.057
PBE	15.00	11.28	13.76	0.117	0.066	0.098
DFT-D2	15.06	11.26	13.79	0.117	0.066	0.098
vdW-DF2	14.91	11.27	13.70	0.115	0.066	0.097
optPBE-vdW	14.98	11.23	13.73	0.116	0.065	0.098
optB88-vdW	15.02	11.25	13.76	0.117	0.0654	0.098
Powder [237]						0.091±0.001
HOPG [237]				0.110±0.001	0.057±0.001	0.093±0.001

Appendix C

News from nowhere: Exploring new sorption regimes in alkali-graphite intercalates

The safe and efficient storage of hydrogen for mobile applications remains an unsolved challenge. Amongst those materials able to store reasonable amounts of hydrogen, potassium-doped graphite intercalates are characterized by a rather unique feature, as they can either physisorb or chemisorb molecular hydrogen depending on the level of metal doping. Molecular hydrogen is either physisorbed at low potassium doping (e.g., KC_{24}) or chemisorbed as a hydride (following bond breaking) at three times this potassium concentration (KC_8). Here quasielastic neutron scattering experiment performed using the OSIRIS spectrometer at the ISIS pulsed neutron source in the UK, was used to gain a deeper understanding of the role of the substrate porosity in the hydrogenation process of the KC_8.

Recently, Howard et al. proposed a new protocol to produce alkali-metal intercalated graphite [235]. This improved synthesis protocol involves first exfoliating the graphite to give very low density expanded substrate. The exfoliated graphite, which consists mainly in a few graphene layers, is then doped with potassium. We looked at the specific case of the exfoliated-KC_8 and we compared the hydrogenation process with the previously studied unexfoliated-KC_8.

First the diffraction pattern of the pristine substrate was measured at different temperatures, namely: 10, 20, 40, 77, 150, 200, 250 and 300 K. The 008 reflection of the KC_8 moves from $\sim$2.65 Å to $\sim$2.68 Å with the temperature, because of the expansion along the c direction of the KC_8. Hydrogen was then loaded in the sample

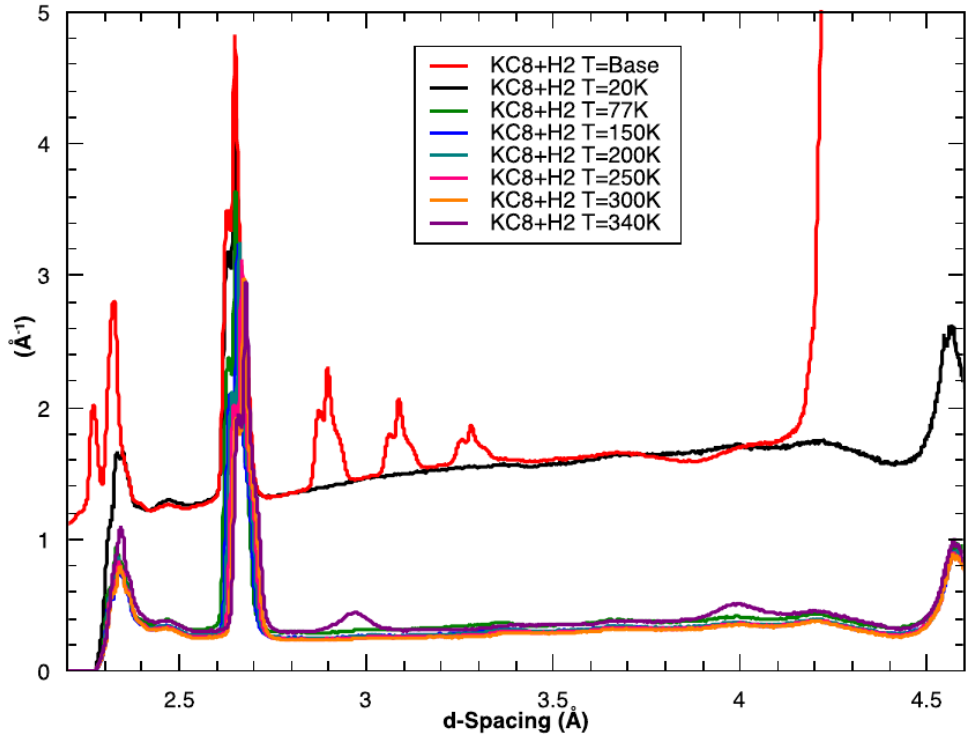

Figure C.1: Diffraction patterns of the KC_8 and H_2 at different temperatures.

cell and its interaction with the KC_8 was monitored at the same set of temperatures.

Fig. C.1 shows a summary of the diffraction pattern of the KC_8 and hydrogen at different temperatures. At base temperature (∼1.5 K) hydrogen solidifies following the substrate template, as showed by the features at 2.9, 3.1 and 3.4 Å in the red spectrum. At 20 K hydrogen is liquid, thus the only outstanding reflections come from the substrate. At higher temperature, hydrogen is in the gas phase and no appreciable interaction with the KC_8 can be highlighted from the diffraction pattern. The temperature needed to be raised up to 340 K in order to hollow KC_8 to chemisorb hydrogen and form the hydrides. The hydrides formation is then illustrated by the new peaks at ∼3.0 and ∼4.0 Å in the diffraction pattern.

The peaks at 0 meV at different temperatures of the inelastic spectra in fig. C.2 show an intense peak in the case of solid hydrogen and a broader one in the case of liquid hydrogen. No particular differences are appreciable in the case of the hydrides at 340 K compared to the gas interacting with the substrate. This suggests that the percentage of the hydrogen that has reacted with the substrate is very low and that probably the substrate was just partially hydrogenated.

These results are in line with the previous study of the unexfoliated-KC_8 by

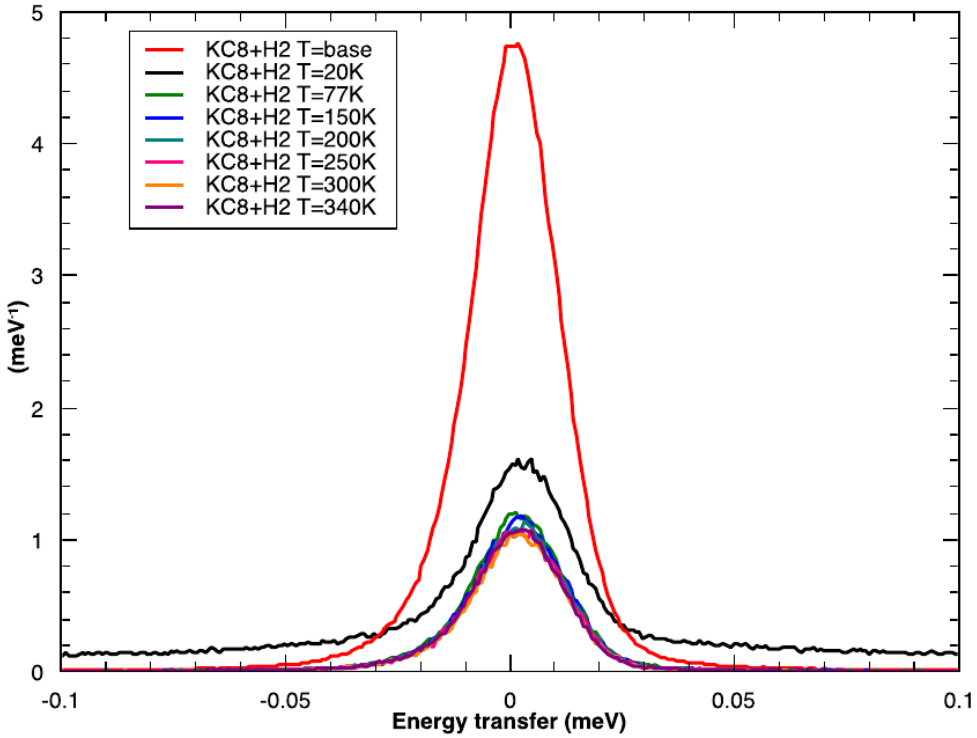

Figure C.2: Inelastic spectra of the KC_8 and H_2 at different temperatures.

Lovell and co–workers. In that case it was found that KC_8 chemisorbs H_2 between 250 and 290 K, if the system is pressurised at 2.90 bar [213]. These results suggest that, in addition to the role of the substrate porosity, further studies need to be run in order to understand the role of the potassium concentration in the regime between KC_8 and KC_{24} in the hydrogen adsorption.

Bibliography

[1] A. K. Geim and K. S. Novoselov. The rise of graphene. *Nat. Mater.*, 6:183–191, 2007.

[2] W. Bollmann and J. Spreadborough. Action of graphite as a lubricant. *Nature*, 186:4718, 1960.

[3] Y. Kimura, T. Wakabayashi, K. Okada, T. Wada, and H. Nishikawa. Boron nitride as a lubricant additive. *Wear*, 232:199–206, 1999.

[4] Dae-Hyun C., Jin-Seon K., Sang-Hyuk K., Changgu L., and Young-Ze L. Evaluation of hexagonal boron nitride nano-sheets as a lubricant additive in water. *Wear*, 302:981 – 986, 2013.

[5] I. Kaplan-Ashiri, S. R. Cohen, K. Gartsman, V. Ivanovskaya, T. Heine, G. Seifert, I. Wiesel, H. D. Wagner, and R. Tenne. On the mechanical behavior of WS_2 nanotubes under axial tension and compression. *PNAS*, 103:523–528, 2006.

[6] C. N. R. Rao, H. S. S. Ramakrishna Matte, and U. Maitra. Graphene analogues of inorganic layered materials. *Angew. Chem. Int. Ed.*, 52:13162–13185, 2013.

[7] M. Nie, D. Chalasani, D. P. Abraham, Y. Chen, A. Bose, and B. L. Lucht. Lithium ion battery graphite solid electrolyte interphase revealed by microscopy and spectroscopy. *J. Phys. Chem. C*, 117:1257–1267, 2013.

[8] H. Li, Z. Yin, Q. He, H. Li, X. Huang, G. Lu, D. W. H. Fam, A. I. Y. Tok, Q. Zhang, and H. Zhang. Fabrication of single-and multilayer MoS_2 film-based field-effect transistors for sensing no at room temperature. *Small*, 8:63–67, 2012.

[9] Q. He, Z. Zeng, Z. Yin, H. Li, S. Wu, X. Huang, and H. Zhang. Fabrication of flexible MoS_2 thin-film transistor arrays for practical gas-sensing applications. *Small*, 8:2994–2999, 2012.

[10] S. Wu, Z. Zeng, Q. He, Z. Wang, S. J. Wang, Y. Du, Z. Yin, X. Sun, W. Chen, and H. Zhang. Electrochemically reduced single-layer MoS_2 nanosheets: Characterization, properties, and sensing applications. *Small*, 8:2264–2270, 2012.

[11] M. Z. Jacobson, W. G. Colella, and D. M. Golden. Cleaning the air and improving health with hydrogen fuel-cell vehicles. *Science*, 308:1901–1905, 2005.

[12] D. L. Trimm and Z. I. Önsan. Onboard fuel conversion for hydrogen-fuel-cell-driven vehicles. *Catalysis Revews: Science and Engineering*, 43:31 – 84, 2001.

[13] F. Fernandez-Alonso, F.J. Bermejo, and M.L. Saboungi. *Molecular hydrogen in carbon nanostructures, Handbook of Nanophysics*.

[14] D.K. Ross. Hydrogen storage: The major technological barrier to the development of hydrogen fuel cell cars. *Vacuum*, 80:1084–1089, 2006.

[15] W. I. F. David. Effective hydrogen storage: a strategic chemistry challenge. *Faraday Discuss.*, 151:399–414, 2011.

[16] K. Hirose. Hydrogen as a fuel for today and tomorrow: expectations for advanced hydrogen storage materials/systems research. *Faraday Discuss.*, 151:11–18, 2011.

[17] L. Wang and R. T. Yang. Hydrogen storage on carbon-based adsorbents and storage at ambient temperature by hydrogen spillover. *Cat. Rev.: Sci. Eng.*, 52:0161–4940, 2010.

[18] K. D. Georgios, E. Tylianakis, and G. E. Froudakis. Pillared graphene: A new 3-D network nanostructure for enhanced hydrogen storage. *Nano Letters*, 8:3166–3170, 2008.

[19] M. P. Shu, H. J. Park, T. K. Prasad, and D-W. Lim. Hydrogen storage in metal-organic frameworks. *Chem. Rev.*, 112:–, 2012.

[20] S. Tedds, A. Walton, D. P. Broom, and D. Book. Characterisation of porous hydrogen storage materials: carbons, zeolites, MOFs and PIMs. *Faraday Discuss.*, 151:75–94, 2011.

[21] T. Enoki, M. Endo, and M. Suzuki. *Graphite Intercalation Compounds and Applications.* Oxford University Press, Oxford, 2003.

[22] S. Patchkovskii, J.S. Tse, S.N. Yurchenko, L. Zhechkov, T. Heine, and G. Seifert. Graphene nanostructures as tunable storage media for molecular hydrogen. *Proc. Nat. Acad. Scien. USA*, 102:10434–10444, 2005.

[23] Z. Yang, Y. Xia, and R. Mokaya. Enhanced hydrogen storage capacity of high surface area zeolite-like carbon materials. *J. Am. Chem. Soc.*, 129:1673–1679, 2007.

[24] T. K. A. Hoang and D. M. Antonelli. Exploiting the Kubas interaction in the design of hydrogen storage materials. *Adv. Mater.*, 21:1787–1800, 2009.

[25] C. Liu, Y. Y. Fan, M. Liu, H. T. Cong, H. M. Cheng, and M. S. Dresselhaus. Hydrogen storage in single-walled carbon nanotubes at room temperature. *Science*, 286:1127–1129, 1999.

[26] H. Tanaka, H. Kanoh, M. Yudasaka, S. Iijima, and K. Kaneko. Quantum effects on hydrogen isotope adsorption on single-wall carbon nanohorns. *J. Am Chem. Soc.*, 127:7511–7516, 2005.

[27] G. Mpourmpakis, E. Tylianakis, and G. E. Froudakis. Carbon nanoscrolls: A promising material for hydrogen storage. *Nano Lett.*, 7:1893–1897, 2007.

[28] T. Enoki, S. Majimaa, M. Sanoa, and H. Inokuchia. Hydrogen-alkali-metal-graphite ternary intercalation compounds. *J. Mater. Res*, 5:435–466, 1990.

[29] A. Lovell, F. Fernandez-Alonso, N. T. Skipper, K. Refson, S.M. Bennington, and S. F. Parker. Quantum delocalization of molecular hydrogen in alkali-graphite intercalates. *Phys. Rev. Lett.*, 101:126101, 2008.

[30] R. J.-M. Pellenq, F. Marinelli, J. D. Fuhr, F. Fernandez-Alonso, and K. Refson. Strong physisorption site for H_2 in K- and Li-doped porous carbons. *J. Chem. Phys.*, 129:224701, 2008.

[31] G. J. Kubas. Molecular hydrogen complexes: coordination of a. sigma. bond to transition metals. *Acc. Chem. Res.*, 21:120–128, 1988.

[32] G. J. Kubas, R. R. Ryan, B. I. Swanson, P. J. Vergamini, and H. J. Wasserman. Characterization of the first examples of isolable molecular hydrogen complexes, M(CO)3(PR3)2(H2) (M = molybdenum or tungsten; R = Cy or isopropyl). evidence for a side-on bonded dihydrogen ligand. *J. Am. Chem. Soc.*, 106:451, 1984.

[33] P. Hohenberg and W. Kohn. Inhomogeneous electron gas. *Phys. Rev*, 136:B864–B871, 1964.

[34] W. Kohn and L. J. Sham. Self-consistent equations including exchange and correlation effects. *Phys. Rev*, 140:A1133–A1138, 1965.

[35] J. Klimeš and A. Michaelides. Perspective: Advances and challenges in treating van der Waals dispersion forces in density functional theory. *J. Chem. Phys.*, 137:120901, 2012.

[36] J. Klimeš, D. R. Bowler, and A. Michaelides. Chemical accuracy for the van der Waals density functional. *J. Phys.: Condens. Matter*, 22:022201, 2010.

[37] J. Klimeš, D. R. Bowler, and A. Michaelides. Van der Waals density functionals applied to solids. *Phys. Rev. B*, 83:195131, 2011.

[38] T. Björkman. van der Waals density functional for solids. *Phys. Rev. B*, 86:165109, 2012.

[39] T. Björkman, A. Gulans, A. V. Krasheninnikov, and R. M. Nieminen. van der Waals bonding in layered compounds frm advanced density functional first principle. *Phys. Rev. Lett.*, 108:235502, 2012.

[40] T. Björkman. Testing several recent van der Waals density functionals for layered structures. *J. Chem. Phys.*, 141:074708, 2014.

[41] N. T. Skipper, J. K. Walters, C. Lobban, J. McKewn, R. Mukerji, G. J. Martin, M. de Podesta, and A. C. Hannon. Neutron diffraction studies of graphite potassium methylamine: Staging transitions and structure of new graphite intercalation compounds. *J. Phys. Chem. B*, 104:10969–10972, 2000.

[42] A. Lovell, S. M. Bennington, N. T. Skipper, C. Gejke, H. Thompson, and M. A. Adams. Neutron scattering studies of hydrogen in potassium graphite intercalates: Towards tunable graphite intercalates for hydrogen storage. *Phys. B: Condensed Matter*, 385-386:163 – 165, 2006. Proceedings of the Eighth International Conference on Neutron Scattering.

[43] M. Born and R. Oppenheimer. Zur quantentheorie der molekeln. *Ann. Phys.*, 389:457–484, 1927.

[44] E. Fermi. Un metodo statistico per la determinazione di alcune priorieta dell'atomo. *Rend. Accad. Naz. Lincei*, 6:32, 1927.

[45] L. H. Thomas. The calculation of atomic fields. *Math. Proc. of the Cambridge Philos. Soc*, 23:542–548, 1927.

[46] J. P. Perdew and A. Zunger. Self-interaction correction to density-functional approximations for many-electron systems. *Phys. Rev. B*, 23:5048–5079, 1981.

[47] S. H. Vosko, L. Wilk, and M. Nusair. Accurate spin-dependent electron liquid correlation energies for local spin density calculations: a critical analysis. *Can. J. Phys.*, 58:1200–1211, 1980.

[48] J. P. Perdew and Y. Wang. Accurate and simple analytic representation of the electron-gas correlation energy. *Phys. Rev. B*, 45:13244–13249, 1992.

[49] D. C. Langreth and J. P. Perdew. Theory of nonuniform electronic systems. i. analysis of the gradient approximation and a generalization that works. *Phys. Rev. B*, 21:5469–5493, 1980.

[50] D. C. Langreth and M. J. Mehl. Beyond the local-density approximation in calculations of ground-state electronic properties. *Phys. Rev. B*, 28:1809–1834, 1983.

[51] J. P. Perdew and W. Yue. Accurate and simple density functional for the electronic exchange energy: Generalized gradient approximation. *Phys. Rev. B*, 33:8800–8802, 1986.

[52] J. P. Perdew. Density-functional approximation for the correlation energy of the inhomogeneous electron gas. *Phys. Rev. B*, 33:8822–8824, 1986.

[53] J. P. Perdew, K. Burke, and M. Ernzerhof. Generalized gradient approximation made simple. *Phys. Rev. Lett.*, 77:3865–3868, 1996.

[54] A. D. Becke. Density-functional exchange-energy approximation with correct asymptotic behavior. *Phys. Rev. A*, 38:3098–3100, 1988.

[55] C. Lee, W. Yang, and R. G. Parr. Development of the colle-salvetti correlation-energy formula into a functional of the electron density. *Phys. Rev. B*, 37:785–789, 1988.

[56] J. P. Perdew. Density-functional approximation for the correlation energy of the inhomogeneous electron gas. *Phys. Rev. B*, 33:8822–8824, 1986.

[57] J. P. Perdew, A. Ruzsinszky, G. I. Csonka, L. A. Constantin, and J. Sun. Workhorse semilocal density functional for condensed matter physics and quantum chemistry. *Phys. Rev. Lett.*, 103:026403, 2009.

[58] G. I. Csonka, J. P. Perdew, A. Ruzsinszky, P. H. T. Philipsen, S. Lebègue, J. Paier, O. A. Vydrov, and J. G. Ángyán. Assessing the performance of recent density functionals for bulk solids. *Phys. Rev. B*, 79:155107, 2009.

[59] K. Burke. Perspective on density functional theory. *J. Chem. Phys.*, 136:150901, 2012.

[60] A. J. Cohen, P. Mori-Sánchez, and W. Yang. Insights into current limitations of density functional theory. *Science*, 321:792–794, 2008.

[61] J. Heyd, J. E. Peralta, G. E. Scuseria, and R. L. Martin. Energy band gaps and lattice parameters evaluated with the heyd-scuseria-ernzerhof screened hybrid functional. *J. Chem. Phys.*, 123, 2005.

[62] C. Adamo and V. Barone. Toward reliable density functional methods without adjustable parameters: The PBE_0 model. *J. Chem. Phys.*, 110, 1999.

[63] J. Heyd, G. E. Scuseria, and M. Ernzerhof. Hybrid functionals based on a screened coulomb potential. *J. Chem. Phys.*, 118:8207–8215, 2003.

[64] P. J. Stephens, F. J. Devlin, C. F. Chabalowski, and M. J. Frisch. Ab initio calculation of vibrational absorption and circular dichroism spectra using density functional force fields. *J. Phys. Chem.*, 98:11623–11627, 1994.

[65] S. Grimme. Accurate description of van der Waals complexes by density functional theory including empirical corrections. *J. Comput. Chem.*, 25:1463–1473, 2004.

[66] S. Grimme. Semiempirical GGA-type density functional constructed with a long-range dispersion correction. *J. Comput. Chem.*, 27:1787–1799, 2006.

[67] J. Antonyd, S. Ehrlich, S. Grimme, and H. Krieg. A consistent and accurate ab initio parametrization of density functional dispersion correction (dft-d) for the 94 elements h-pu. *J. Chem. Phys.*, 132:154104, 2010.

[68] A. Tkatchenko and M. Scheffler. Accurate molecular van der Waals interactions from ground-state electron density and free-atom reference data. *Phys. Rev. Lett.*, 102:073005, 2009.

[69] M. Dion, H. Rydberg, E. Schröder, D. C. Langreth, and B. I. Lundqvist. Van der Waals density functional for general geometries. *Phys. Rev. Lett.*, 92:246401, 2004.

[70] R. D. Adamson, J. P. Dombroski, and P. M. W. Gill. Efficient calculation of short-range coulomb energies. *J. Comput. Chem.*, 20:921–927, 1999.

[71] K. Lee, E. D. Murray, L. Kong, B. I. Lundqvist, and D. C. Langreth. Higher-accuracy van der Waals density functional. *Phys. Rev. B*, 82:081101, 2010.

[72] O. A. Vydrov and T. Van Voorhis. Dispersion interactions from a local polarizability model. *Phys. Rev. A*, 81:062708, 2010.

[73] J. Carrasco, B. Santra, J. Klimeš, and A. Michaelides. To wet or not to wet? dispersion forces tip the balance for water ice on metals. *Phys. Rev. Lett.*, 106:026101, 2011.

[74] P. Nozières and D. Pines. Correlation energy of a free electron gas. *Phys. Rev.*, 111:442–454, Jul 1958.

[75] A. Tkatchenko, R. A. DiStasio Jr, R. Car, and M. Scheffler. Accurate and efficient method for many-body van der Waals interactions. *Phys. Rev. Let.*, 108:236402, 2012.

[76] H. J. Monkhorst and J. D. Pack. Special points for brillouin-zone integrations. *Phys. Rev. B*, 13:5188–5192, 1976.

[77] D. Vanderbilt. Soft self-consistent pseudopotentials in a generalized eigenvalue formalism. *Phys. Rev. B*, 41:7892–7895, 1990.

[78] P. E. Blöchl. Projector augmented-wave method. *Phys. Rev. B*, 50:17953–17979, 1994.

[79] R. Car and M. Parrinello. Unified approach for molecular dynamics and density-functional theory. *Phys. Rev. Lett.*, 55:2471, 1985.

[80] K. Laasonen, A. Pasquarello, R. Car, C. Lee, and D. Vanderbilt. Car-parrinello molecular dynamics with vanderbilt ultrasoft pseudopotentials. *Phys. Rev. B*, 47:10142, 1993.

[81] D. Marx and M. Parrinello. Ab initio path integral molecular dynamics: Basic ideas. *J. Chem. Phys.*, 104(11):4077–4082, 1996.

[82] S. Baroni, S. de Gironcoli, A. Dal Corso, and P. Giannozzi. Phonons and related crystal properties from density-functional perturbation theory. *Rev. Mod. Phys.*, 73:515–562, 2001.

[83] M. E. Tuckerman. *Statistical Mechanics: Theory and Molecular Simulation.* Oxford Graduate Texts, 2010.

[84] R. P. Feynman. Space-time approach to non-relativistic quantum mechanics. *Rev. Mod. Phys.*, 20:367, 1948.

[85] M. T Dove. *Structure and Dynamics. An atomic view of materials.* Oxford Univ., 2003.

[86] P. C. H. Mitchell, S. F. Parker, A. J. Ramirez-Cuesta, and J. Tomkinson. *Vibrational Spectroscopy with Neutrons, with Applications in Chemistry, Biology, Materials Science, and Catalysis.* World Scientific, London, 2005.

[87] G. L. Squires. *Introduction to the theory of thermal neutron scattering.* Cambridge university press, 2012.

[88] D. L Price and F. Fernandez-Alonso. *Neutron Scattering.* Academic Press, 2013.

[89] D. A. Keen, M. J. Gutmann, and C. C. Wilson. SXD-the single-crystal diffractometer at the isis spallation neutron source. *J. Appl. Cryst.*, 39:714–722, 2006.

[90] P. Debye. Interferenz von röntgenstrahlen und wärmebewegung. *Annalen der Physik*, 348:49–92, 1913.

[91] I. Waller. Zur frage der einwirkung der wärmebewegung auf die interferenz von röntgenstrahlen. *Zeitschrift für Physik A Hadrons and Nuclei*, 17:398–408, 1923.

[92] S. Rudic, A. J. Ramirez-Cuesta, S. F. Parker, F. Fernandez-Alonoso, R. S. Pinna, G. Gorini, C. G. Salzmann, S. E. McLain, and N. T. Skipper. *TOSCA International Beamline Review.* Rutherford Appleton Laboratory Tecnical Report RAL-2013-015, Didcot, 2013. http://purl.org/net/epubs/work/11216706.

[93] R. S. Pinna et al. Monte carlo simulations of the tosca spectrometer: assessment of current performance and future upgrades. *Europ. Phys. J.*, 2014. in press.

[94] S. F. Parker et al. Recent and future developments on tosca at isis. *J. Phys: Conference Series*, 2014. in press.

[95] J. Mayers. Quantum effects in deep inelastic neutron scattering. *Phys. Rev. B*, 41:41–51, 1990.

[96] R. Senesi, C. Andreani, Z. Bowden, D. Colognesi, E. Degiorgi, A. L. Fielding, J. Mayers, M. Nardone, J. Norris, M. Praitano, et al. Vesuvio: a novel instrument for performing spectroscopic studies in condensed matter with ev neutrons at the isis facility. *Physica B: Condens. Matter*, 276:200–201, 2000.

[97] M. T. F. Telling and K. H. Andersen. Spectroscopic characteristics of the OSIRIS near-backscattering crystal analyser spectrometer on the ISIS pulsed neutron source. *Phys. Chem. Chem. Phys.*, 7:1255–1261, 2005.

[98] K. H. Andersen, D. M. y Marero, and M. J. Barlow. The osiris diffractometer and polarisation-analysis backscattering spectrometer. *Appl. Phys. A*, 74:s237–s239, 2002.

[99] F. Demmel et al. Opening the terahertz window on the osiris spectrometer. *Europ. Phys. J.*, 2014. in press.

[100] J. F. Dobson and B. P. Dinte. Constraint satisfaction in local and gradient susceptibility approximations: Application to a van der Waals density functional. *Phys. Rev. Lett.*, 76:1780–1783, 1996.

[101] Y. Andersson, D. C. Langreth, and B. I. Lundqvist. van der Waals interactions in density-functional theory. *Phys. Rev. Lett.*, 76:102–105, 1996.

[102] E. Hult, Y. Andersson, B. I. Lundqvist, and D. C. Langreth. Density functional for van der Waals forces at surfaces. *Phys. Rev. Lett.*, 77:2029–2032, 1996.

[103] H. Rydberg, M. Dion, N. Jacobson, E. Schröder, P. Hyldgaard, S. I. Simak, D. C. Langreth, and B. I. Lundqvist. Van der Waals density functional for layered structures. *Phys. Rev. Lett.*, 91:126402, 2003.

[104] J. Harl and G. Kresse. Accurate bulk properties from approximate many-body techniques. *Phys. Rev. Lett.*, 103:056401, Jul 2009.

[105] A. D. Becke and E. R. Johnson. Exchange-hole dipole moment and the dispersion interaction. 122:154104, 2005.

[106] S.-H. Jhi and Y.-K. Kwon. Hydrogen adsorption on boron nitride nanotubes: A path to room-temperature hydrogen storage. *Phys. Rev. B*, 69:245407, 2004.

[107] A. Rairkar, J. B. Adams, and N. Ooi. Density functional study of graphite bulk and surface properties. *Carbon*, 44:231–242, Jul 2005.

[108] L. A. Girifalco and M. Hodak. Van der Waals binding energies in graphitic structures. *Phys. Rev. B*, 65, 2002.

[109] S. Kristyán and P. Pulay. Can (semi)local density functional theory account for the london dispersion forces? *Chem. Phys. Lett.*, 229:175–180, Oct 1994.

[110] J. M Pérez-Jordá and A. D. Becke. A density-functional study of van der Waals forces: rare gas diatomics. *Chem. Phys. Lett.*, 233:134–137, Feb 1995.

[111] L. Spanu, S. Sorella, and G. Galli. Nature and strength of interlayer binding in graphite. *Phys. Rev. Lett.*, 103:196401, 2009.

[112] W. Kohn, Y. Meir, and D. E. Makarov. Van der Waals energies in density functional theory. *Phys. Rev. Lett.*, 80:4153–4156, May 1998.

[113] E. Ziambaras, J. Kleis, E. Schröder, and P. Hyldgaard. Potassium intercalation in graphite: A van der Waals density-functional study. *Phys. Rev. B*, 76:155425, 2007.

[114] I. Hamada and M. Otani. Comparative van der Waals density-functional study of graphene on metal surfaces. *Phys. Rev. B*, 82:153412, 2010.

[115] N. Marom, J. Bernstein, J. Garel, A. Tkatchenko, E. Joselevich, L. Kronik, and O. Hod. Stacking and registry effects in layered materials: The case of hexagonal boron nitride. *Phys. Rev. Lett.*, 105:046801, 2010.

[116] F. Hanke. Sensitivity analysis and uncertainty calculation for dispersion corrected density functional theory. *J. Comp. Chem.*, 32, 2011.

[117] S. Lebègue, J. Harl, T. Gould, J. G. Ángyán, G. Kresse, and J. F. Dobson. Cohesive properties and asymptotics of the dispersion interaction in graphite by the random phase approximation. *Phys. Rev. Lett.*, 105:196401, 2010.

[118] G. Kresse and J. Hafner. Ab initio molecular dynamics for liquid metals. *Phys. Rev. B*, 47:558–561, 1993.

[119] G. Kresse and J. Furthmüller. Efficiency of ab-initio total energy calculations for metals and semiconductors using a plane-wave basis set. *Comp. Mater. Sci.*, 6(1):15–50, 1996.

[120] G. Kresse and J. Furthmüller. Efficient iterative schemes for ab initio total-energy calculations using a plane-wave basis set. *Phys. Rev. B*, 54:11169–11186, 1996.

[121] G. Román-Pérez and J. M. Soler. Efficient implementation of a van der Waals density functional: Application to double-wall carbon nanotubes. *Phys. Rev. Lett.*, 103:096102, Aug 2009.

[122] R. Zacharia, H. Ulbricht, and T. Hertel. Interlayer cohesive energy of graphite from thermal desorption of polyaromatic hydrocarbons. *Phys. Rev. B*, 69:155406, 2004.

[123] A. Peluso and S. Fliszá. Charge distribution and chemical effects, xlv. graphite. *Can. J. Chem.*, 66:2631–2633, 1988.

[124] D. R. Lide, editor. *CRC Handbook of Chemistry and Physics*. CRC Press, Boca Raton, 2008.

[125] Buckingham potential: $E = a\exp(-bx) + e/x^6$, where a, b and e are constants and x is the interatomic distance. The first term describes the repulsion and the second one describe the attraction between two particles. Due to the integration over a surface, this term tuns up to depend on x^{-4}.

[126] K. Berland, Ø. Borck, and P. Hyldgaard. Van der Waals density functional calculations of binding in molecular crystals. *Comp. Phys. Commun.*, 182:1800–1804, 2011.

[127] N. Mounet and N. Marzari. First-principles determination of the structural, vibrational and thermodynamic propertie/s of diamond, graphite, and derivatives. *Phys. Rev. B*, 71:205214, 2005.

[128] S. D. Chakarova-Käck, A. Vojvodic, J. Kleis, P. Hyldgaard, and E. Schröder. Binding of polycyclic aromatic hydrocarbons and graphene dimers in density functional theory. *New J. of Phys.*, 12, 2010.

[129] S. Kabalkina and L.F. Vereshchagin. X-ray diffraction study of ZnF 2 at pressures up to 130 Kbar and at temperatures of 25 and 300. *Sov. Phys. Dokl.*, 5:1065, 1961.

[130] G. Kresse, G. Kern, and J. Hafner. Ab initio calculation of the lattice dynamics and phase diagram of boron nitride. *Phys. Rev. B*, 59:8551–8559, 1999.

[131] L. Liu, Y. P. Feng, and Z. X. Shen. Structural and electronic properties of h-bn. *Phys. Rev. B*, 68:104102, 2003.

[132] V. L. Solozhenko, G. Will, and F. Elf. Isothermal compression of hexagonal graphite-like boron nitride up to 12 gpa. *Solid State Commun.*, 96:1–3, 1995.

[133] A. Marini, P. García-González, and A. Rubio. First-principles description of correlation effects in layered materials. *Phys. Rev. Lett.*, 96:136404, 2006.

[134] J. F. Green, T. K. Bolland, and J. W. Bolland. Theoretical elastic behavior for hexagonal boron-nitride. *J. Chem. Phys.*, 64:656–662, 1976.

[135] F. Mittendorfer, A. Garhofer, J. Redinger, J. Klimeš, J. Harl, and G Kresse. Graphene on Ni (111): Strong interaction and weak adsorption. *Phys. Rev. B*, 84:201401, 2011.

[136] X. Li, J. Feng, E. Wang, S. Meng, J. Klimeš, and A. Michaelides. Influence of water on the electronic structure of metal-supported graphene: Insights from van der Waals density functional theory. *Phys. Rev. B*, 85:085425, 2012.

[137] X. L. Hu, J. Carrasco, J. Klimeš, and A. Michaelides. Trends in water monomer adsorption and dissociation on flat insulating surfaces. *Phys. Chem. Chem. Phys.*, 13:12447–12453, 2011.

[138] W. Lew, M. C. Crowe, C. T. Campbell, J. Carrasco, and A. Michaelides. The energy of hydroxyl coadsorbed with water on Pt(111). *J. Phys. Chem. C*, 115:23008–23012, 2011.

[139] C. Zhang, J. Wu, G. Galli, and F. Gygi. Structural and vibrational properties of liquid water from van der Waals density functionals. *J. Chem. Theory Comput.*, 7:3054–3061, 2011.

[140] M. A. F. Addato, A. A. Rubert, G. A. Benítez, M. H. Fonticelli, J. Carrasco, P. Carro, and R. C. Salvarezza. Alkanethiol adsorption on platinum: Chain length effects on the quality of self-assembled monolayers. *J. Phys. Chem. C*, 115:17788–17798, 2011.

[141] O. A. von Lilienfeld and A. Tkatchenko. Two- and three-body interatomic dispersion energy contributions to binding in molecules and solids. *J. Chem. Phys.*, 132:234109, 2010.

[142] M. Nie, D. Chalasani, D. P. Abraham, Y. Chen, A. Bose, and B. L. Lucht. Lithium ion battery graphite solid electrolyte interphase revealed by microscopy and spectroscopy. *J. Phys. Chem. C*, 117(3):1257–1267, 2013.

[143] R. J. Nemanich and A. S. Solin. First- and second-order raman scattering from finite-size crystals of graphite. *Phys. Rev. B*, 20:392–401, 1979.

[144] J. Maultzsch, S. Reich, C. Thomsen, H. Requardt, and P Ordejón. Phonon dispersion in graphite. *Phys. Rev. Let.*, 92:075501, 2004.

[145] M. Mohr, J. Maultzsch, E. Dobardžić, S. Reich, I. Milošević, M. Damnjanović, A. Bosak, M. Krisch, and C. Thomsen. Phonon dispersion of graphite by inelastic x-ray scattering. *Phys. Rev. B*, 76:035439, 2007.

[146] A. Bosak, M. Krisch, M. Mohr, J. Maultzsch, and C. Thomsen. Elasticity of single-crystalline graphite: Inelastic x-ray scattering study. *Phys. Rev. B*, 75:153408, 2007.

[147] J. Maultzsch, S. Reich, and C. Thomsen. Double-resonant raman scattering in graphite: Interference effects, selection rules, and phonon dispersion. *Phys. Rev. B.*, 70:155403, 2004.

[148] S. Reich and C. Thomsen. Raman spectroscopy of graphite. *Phil. Trans. R. Soc. Lon. A*, 362:2271–2288, 2004.

[149] M. Lazzeri, S. Piscanec, F. Mauri, A. C. Ferrari, and J. Robertson. Phonon linewidths and electron-phonon coupling in graphite and nanotubes. *Phys. Rev. B*, 73:155426, 2006.

[150] P. H. Tan, W. P. Han, W. J. Zhao, Z. H. Wu, K. Chang, H. Wang, Y. F. Wang, N. Bonini, N. Marzari, N. Pugno, et al. The shear mode of multilayer graphene. *Nature materials*, 11:294–300, 2012.

[151] A. C. Ferrari. Raman spectroscopy of graphene and graphite: Disorder, electron-phonon coupling, doping and nonadiabatic effects. *Solid State Communications*, 143:47 – 57, 2007.

[152] R. Saito, A. Jorio, A. G. Souza Filho, G. Dresselhaus, M. S. Dresselhaus, and M. A. Pimenta. Probing phonon dispersion relations of graphite by double resonance raman scattering. *Phys. Rev. Let.*, 88(2):027401, 2001.

[153] R. Al-Jishi and G. Dresselhaus. Lattice-dynamical model for graphite. *Phys. Rev. B*, 26:4514, 1982.

[154] L. Wirtz and A. Rubio. The phonon dispersion of graphite revisited. *Solid State Commun.*, 131:141 – 152, 2004.

[155] M. Lazzeri, C. Attaccalite, L. Wirtz, and F. Mauri. Impact of the electron-electron correlation on phonon dispersion: Failure of LDA and GGA DFT functionals in graphene and graphite. *Phys. Rev. B*, 78:081406, 2008.

[156] S. Piscanec, M. Lazzeri, F. Mauri, A. C. Ferrari, and J. Robertson. Kohn anomalies and electron-phonon interactions in graphite. *Phys. Rev. Lett.*, 93:185503, 2004.

[157] J. D. Dunitz, V. Schomaker, and K. N. Trueblood. Interpretation of atomic displacement parameters from diffraction studies of crystals, 1988.

[158] H. Xu, Y. Zhao, D. D. Hickmott, N. J. Lane, S. C. Vogel, J. Zhang, and L. L. Daemen. High-temperature neutron diffraction study of deuterated brucite. *Phys. Chem. Minerals*, 40:799–810, 2013.

[159] M. J. Gutmann, K. Refson, M. v. Zimmermann, I. P. Swainson, A. Dabkowski, and H. Dabkowska. Room temperature single-crystal diffuse scattering and ab initio lattice dynamics in catisio 5. *J. Phys.: Condens. Matter*, 25:315402, 2013.

[160] W. Hummel, A. Raselli, and H.B. Burgi. Analysis of atomic displacement parameters and molecular motion in crystals. *Acta Cryst.*, 46:683–692, 1990.

[161] N. J. Lane, S. C. Vogel, G. Hug, A. Togo, L. Chaput, L. Hultman, and M. W. Barsoum. Neutron diffraction measurements and first-principles study of thermal motion of atoms in select M n+1 ax n and binary mx transition-metal carbide phases. *Phys. Rev. B*, 86:214301, 2012.

[162] L. D. Zhao, S. H. Lo, Y. Zhang, H. Sun, G. Tan, C. Uher, C. Wolverton, V. P Dravid, and M. G. Kanatzidis. Ultralow thermal conductivity and high thermoelectric figure of merit in snse crystals. *Nature*, 508:373–377, 2014.

[163] J. Sootsman, D. Y. Chung, and M.G. Kanatzidis. New and old concepts in thermoelectric materials. *Angew. Chem. Int. Ed.*, 48:8616–8639, 2009.

[164] M. J. Gutmann. *SXD2001.* Oxfordshire: ISIS Facility, Rutherford Appleton Laboratory, 2005.

[165] V. Petricek, M. Dusek, and Palatinus. *The crystallographic computing system.* Institute of Physics, Praha, Czech Republi, 2006. Program availabe at http://jana.fzu.cz/.

[166] A. Togo, F. Oba, and I. Tanaka. First-principles calculations of the ferroelastic transition between rutile-type and $CaCl_2$-type SiO_2 at high pressures. *Phys. Rev. B*, 78:134106, 2008.

[167] M. J. McGrath, J. I. Siepmann, I.-F. W. Kuo, C. J. Mundy, J. VandeVondele, M. Sprik, J. Hutter, F. Mohamed, M. Krack, and M. Parrinello. Toward a

monte carlo program for simulating vapor liquid phase equilibria from first principles. *Comp. Phys. Comm.*, 167:103, 2005.

[168] M. Ceriotti, J. More, and D. E. Manolopoulos. i-PI: A python interface for ab initio path integral molecular dynamics simulations. *Comp. Phys. Comm.*, 185:1019 – 1026, 2014.

[169] M. Ceriotti, G. Bussi, and M. Parrinello. Nuclear quantum effects in solids using a colored-noise thermostat. *Phys. Rev. Lett.*, 103:030603, 2009.

[170] M. Ceriotti, G. Bussi, and M. Parrinello. Colored-noise thermostats á la carte. *J. Chem. Theory Comput.*, 6:1170–1180, 2010.

[171] M. Ceriotti, D. E. Manolopoulos, and M. Parrinello. Accelerating the convergence of path integral dynamics with a generalized langevin equation. *J. Chem. Phys.*, 134:084104, 2011.

[172] S. Plimpton. Fast parallel algorithms for short-range molecular dynamics. *J. Comp. Phys.*, 117:1–19, 1995.

[173] J. Tersoff. Empirical interatomic potential for carbon, with applications to amorphous carbon. *Phys. Rev. Lett.*, 61:2879–2882, 1988.

[174] J. Tersoff. New empirical approach for the structure and energy of covalent systems. *Phys. Rev. B*, 37:6991–7000, Apr 1988.

[175] L. Lindsay and D. A. Broido. Optimized tersoff and brenner empirical potential parameters for lattice dynamics and phonon thermal transport in carbon nanotubes and graphene. *Phys. Rev. B*, 81:205441, 2010.

[176] D. L. Nika, E. P. Pokatilov, A. S. Askerov, and A. A. Balandin. Phonon thermal conduction in graphene: Role of umklapp and edge roughness scattering. *Phys. Rev. B*, 79:155413, 2009.

[177] Y. Baskin and L. Meyer. Lattice constants of graphite at low temperatures. *Phys. Rev.*, 100:544, 1955.

[178] J. B. Nelson and D. P. Riley. The thermal expansion of graphite from 15 c. to 800 c.: Part i. experimental. *Proc. Phys. Soc.*, 57:477, 1945.

[179] R. Nicklow, N. Wakabayashi, and H. G. Smith. Lattice dynamics of pyrolytic graphite. *Phys. Rev. B*, 5:4951–4962, 1972.

[180] H. B. Bürgi, S. C. Capelli, and H. Birkedal. Anharmonicity in anisotropic displacement parameters. *Acta Cryst.*, 56:425–435, 2000.

[181] H. B. Bürgi and S. C. Capelli. Dynamics of molecules in crystals from multi-temperature anisotropic displacement parameters. i. theory. *Acta Cryst.*, 56:403–412, 2000.

[182] J. Antony and S. Grimme. Density functional theory including dispersion corrections for intermolecular interactions in a large benchmark set of biologically relevant molecules. *Phys. Chem. Che. Phys*, 8(45):5287–5293, 2006.

[183] V. R. Cooper, T. Thonhauser, A. Puzder, E. Schröder, B. I. Lundqvist, and D. C. Langreth. Stacking interactions and the twist of DNA. *J. Am. Chem. Soc.*, 130(4):1304–1308, 2008.

[184] J. Tao, J. P. Perdew, and A. Ruzsinszky. Long-range van der Waals attraction and alkali-metal lattice constants. *Phys. Rev. B*, 81:233102, 2010.

[185] K. Johnston, J. Kleis, B. I. Lundqvist, and R. M. Nieminen. Influence of van der Waals forces on the adsorption structure of benzene on silicon studied using density functional theory. *Phys. Rev. B*, 77:121404, 2008.

[186] S. D. Chakarova-Käck, E. Schröder, B. I. Lundqvist, and D. C. Langreth. Application of van der Waals density functional to an extended system: Adsorption of benzene and naphthalene on graphite. *Phys. Rev. Lett.*, 96:146107, 2006.

[187] LW Bruch. Theory of physisorption interactions. *Surface Science*, 125:194–217, 1983.

[188] R. J. Pellenq, F. Marinelli, J. D. Fuhr, F. Fernandez-Alonso, and K. Refson. Strong physisorption site for h2 in k- and li-doped porous carbons. *J. Chem. Phys.*, 129:22470, 2008.

[189] R. Ströbel, J. Garche, P.T. Moseley, L. Jörissen, and G. Wolf. Hydrogen storage by carbon materials. *J. Pow. Sour.*, 159:781 – 801, 2006.

[190] G. Srinivas, Y. Zhu, R. Piner, N. Skipper, M. Ellerby, and R. Ruoff. Synthesis of graphene-like nanosheets and their hydrogen adsorption capacity. *Carbon*, 48:630 – 635, 2010.

[191] J. S. Arellano, L. M. Molina, A. Rubio, and J. A. Alonso. Density functional study of adsorption of molecular hydrogen on graphene layers. *J. Chem. Phys.*, 112, 2000.

[192] D. Henwood and J. David Carey. *Ab initio* investigation of molecular hydrogen physisorption on graphene and carbon nanotubes. *Phys. Rev. B*, 75:245413, 2007.

[193] M. Rubeš and O. Bludský. DFT/CCSD(T) investigation of the interaction of molecular hydrogen with carbon nanostructures. *Chem. Phys. Chem.*, 3:1868–73, 2009.

[194] F. Costanzo, P. L. Silvestrelli, and F. Ancillotto. Physisorption, diffusion, and chemisorption pathways of H_2 molecule on graphene and on (2, 2) carbon nanotube by first principles calculations. *J. Chem. Theory Comput.*, 8:1288, 2012.

[195] Y. Okamoto and Y. Miyamoto. Ab initio investigation of physisorption of molecular hydrogen on planar and curved graphenes. *J. Phys. Chem. B*, 105:3470–3474, 2001.

[196] T. Heine, L. Zhechkov, and G. Seifert. Hydrogen storage by physisorption on nanostructured graphite platelets. *Phys. Chem. Chem. Phys.*, 6:980–984, 2004.

[197] A. Ferre-Vilaplana. Numerical treatment discussion and ab initio computational reinvestigation of physisorption of molecular hydrogen on graphene. *J. Chem. Phys.*, 122:104709, 2005.

[198] Q. Wang and J. K. Johnson. Computer simulations of hydrogen adsorption on graphite nanofibers. *J. Phys. Chem. B*, 103:277–281, 1999.

[199] R. F. Cracknell. Molecular simulation of hydrogen adsorption in graphitic nanofibres. *Phys. Chem. Chem. Phys.*, 3:2091–2097, 2001.

[200] S. A. Shevlin and Z. X. Guo. Hydrogen sorption in defective hexagonal BN sheet and BN nanotubes. *Phys. Rev. B*, 76:024104, 2007.

[201] V. Alexiev, R. Prins, and T. Weber. Dft study of mos2 and hydrogen adsorbed on the 101 face of MoS_2. *Phys. Chem. Chem. Phys.*, 3:5326–5336, 2001.

[202] J. Chen, S. L. Li, Z. L. Tao, Y. T. Shen, and C. X. Cui. Titanium disulfide nanotubes as hydrogen-storage materials. *J. Am. Chem. Soc.*, 125:5284–5285, 2003.

[203] X. S. Li, Q. Xin, X. X. Guo, P. Grange, and B. Delmon. Reversible hydrogen adsorption on MoS_2 studied by temperature-programmed desorption and temperature-programmed reduction. *J. Catal.*, 137:385 – 393, 1992.

[204] L. She, J. Li, D. Gu, Y. Shi, R. Che, and D. Zhao. High-resolution electron microscopy study of mesoporous dichalcogenides and their hydrogen storage properties. *Nanotechnology*, 22:075702, 2011.

[205] T. Bučko, S. Lebègue, J. Hafner, and J. G. Ángyán. Tkatchenko-Scheffler van der Waals correction method with and without self-consistent screening applied to solids. *Phys. Rev. B*, 87:064110, 2013.

[206] L. Mattera, F. Rosatelli, C. Salvo, F. Tommasini, U. Valbusa, and G. Vidali. Selective adsorption of $1H_2$ and $2H_2$ on the (0001) graphite surface. *Sur. Sci.*, 93:515–525, 1980.

[207] P. Wang, S. Orimo, T. Matsushima, H. Fujii, and G. Majer. Hydrogen in mechanically prepared nanostructured h-BN: a critical comparison with that in nanostructured graphite. *App. Phys. Lett.*, 80:318–320, 2002.

[208] Z. Zhou, J. Zhao, Z. Chen, X. Gao, T. Yan, B. Wen, and P. Schleyer. Comparative study of hydrogen adsorption on carbon and BN nanotubes. *J. Phys. Chem. B*, 110:13363–13369, 2006.

[209] S. Krishnan, R. Vadapoo, K. E. Riley, and J. P. Velev. Dispersion-corrected density functional theory comparison of hydrogen adsorption on boron-nitride and carbon nanotubes. *Phys. Rev. B*, 84:165408, 2011.

[210] S. Alvarez. A cartography of the van der Waals territories. *Dalton Trans.*, 42:8617, 2013.

[211] T. A. Halgren and W. Damm. Polarizable force fields. *Current opinion in structural biology*, 11:236–242, 2001.

[212] K. Ichimura, E. Takamura, and M. Sano. Hydrogen in alkali-metal-graphite intercalation compounds. *Synthetic Metals*, 40:355–368, 1991.

[213] A. Lovell, N. T. Skipper, S. M. Bennington, and R. I. Smith. A high-resolution neutron scattering study of the hydrogen-driven metal-insulator phase transition in KC_8H_x. *J. of All. Comp.*, 446–447:397 – 401, 2007.

[214] G. Srinivas, A. Lovell, C. A. Howard, N. T. Skipper, M. Ellerby, and S. M. Bennington. Structure and phase stability of hydrogenated first-stage alkali- and alkaline-earth metal graphite intercalation compounds. *Synth. Met.*, 160:1631 – 1635, 2010.

[215] E. M. Milner, N. T. Skipper, C. A. Howard, M. S. P. Shaffer, D. J. Buckley, K. A. Rahnejat, P. L. Cullen, R. K. Heenan, P. Lindner, and R. Schweins. Structure and morphology of charged graphene platelets in solution by small-angle neutron scattering. *J. Am. Chem. Soc.*, 134:8302–8305, 2012.

[216] S. B. DiCenzo, G. K. Wertheim, S. Basu, and J. E. Fischer. Charge distribution in potassium graphite. *Phys. Rev. B*, 24:2270–2273, 1981.

[217] G. L. Doll and P. C. Eklund. *In situ* optical-reflectance study of H_2 physisorption in $C_{24}K$. *Phys. Rev. B*, 36:9191–9195, 1987.

[218] R. Benedek, A. P. Smith, and L. H. Yan. Charge transfer in Rb-intercalated graphites. *Phys. Rev. B*, 49:7786–7789, 1994.

[219] J. J. Purewal, J. B. Keith, C. C. Ahn, B. Fultz, C. M. Brown, and M. Tyagi. Adsorption and melting of hydrogen in potassium-intercalated graphite. *Phys. Rev. B*, 79:054305, 2009.

[220] J. Purewal. *Hydrogen adsorption by alkali metal graphite intercalation compounds.* PhD thesis, California Institute of Technology, 2010.

[221] Y. Arai, Y. Shirakawa, and S. Tamaki. Structuralproperties of lowdimensional potassium metal in intercalated graphite. *J. Non-Crystalline Solids*, 205–207:803–806, 1996.

[222] D. E. Nixon and G. S. Parry. Order-disorder transformation in potassium graphite. *Nature*, 216:909–910, 1967.

[223] J. B. Hastings, W. D. Ellenson, and J. E. Fischer. Phase transitions in potassium-intercalated graphite: KC_{24}. *Phys. Rev. Lett.*, 42:1552–1556, 1979.

[224] F. Rousseaux, R. More, D. Guerard, and P. Lagrange. X-ray study of the liquid and solid phases of the alkali metals in KC_{24}- and RbC_{24}-intercalated graphite single crystal. *Phys. Rev. B*, 42:725–742, 1990.

[225] H. Cheng, G. Pez, G. Kern, G. Kresse, and J. Hafner. Hydrogen adsorption in potassium-intercalated graphite of second stage: An ab initio molecular dynamics study. *J. Phys. Chem. B*, 105:736–742, 2001.

[226] M. Krzystyniak, M. A. Adams, A. Lovell, N. T. Skipper, S. M. Bennington, J. Mayers, and F. Fernandez-Alonso. Probing the binding and spatial arrangement of molecular hydrogen in porous hosts via neutron compton scattering. *Faraday Discuss.*, 151:–, 2011. in press.

[227] A. P. Smith, R. Benedek, F. R. Trouw, M. Minkoff, and L. H. Yang. Quasi-two-dimensional quantum states of H_2 in stage-2 Rb-intercalated graphite. *Phys. Rev. B*, 53:10187–10199, 1996.

[228] J. G. Vitillo, Alessandro Damin, Adriano Zecchina, and Gabriele Ricchiardi. Theoretical characterization of dihydrogen adducts with alkaline cations. *J. Chem. Phys.*, 122:114311, 2005.

[229] M. Nielsen and W. D. Elleson. *Proceedings of the 14th International Conference on Low Temperature Physics.* 1975.

[230] F. Fernandez-Alonso, F. J. Bermejo, C. Cabrillo, R. O. Loutfy, V. Leon, and M. L. Saboungi. Nature of the bound states of molecular hydrogen in carbon nanohorns. *Phys. Rev. Lett.*, 98:215503, 2007.

[231] K. Watanabe, T. Kondow, M. Soma, T. Onishi, and K. Tamaru. Molecular-sieve type sorption on alkali graphite intercalation compounds. *Proc. R. Soc. Lond. A*, 333:51–67, 1991.

[232] A. Michels, W. De Graaff, and C. A. Ten Seldam. Virial coefficients of hydrogen and deuterium at temperatures between -175 C and + 150 C. conclusions from the second virial coefficient with regards to the intermolecular potential. *Physica*, 26:393–408, 1960.

[233] K. Watanabe, M. Soma, T. Onishi, and K. Tamaru. Sorption of molecular hydrogen by potassium graphite. *Nature Phys. Sci.*, 233:160–161, 1971.

[234] A. K. Geim and I. V. Grigorieva. Van der Waals heterostructures. *Nature*, 499:419–425, 2013.

[235] C. A. Howard, M. P. M. Dean, and F. Withers. Phonons in potassium-doped graphene: the effects of electron-phonon interactions, dimensionality, and adatom ordering. *Phys. Rev. B*, 84:241404, 2011.

[236] G. Dolling and B. N. Brockhouse. Lattice vibrations in pyrolitic graphite. *Phys. Rev.*, 128:1120–1123, 1962.

[237] A. L. Fielding, D. N. Timms, and J. Mayers. Measurement of anisotropies of the kinetic energy and anharmonicity in pyrolytic graphite by neutron compton scattering. *Europhys. Let.*, 44:255, 1998.